Development of an Integrated Estimation Method for Vehicle States, Parameters and Tire Forces

by

Ayyoub Rezaeian

A thesis
presented to the University of Waterloo
in fulfillment of the
thesis requirement for the degree of
Doctor of Philosophy
in
Mechanical Engineering

Waterloo, Ontario, Canada, 2015

AUTHOR'S DECLARATION

I hereby declare that I am the sole author of this thesis. This is a true copy of the thesis, including any required final revisions, as accepted by my examiners.

I understand that my thesis may be made electronically available to the public.

Ayyoub Rezaeian

Abstract

Stability and desirable performance of vehicle control systems are directly dependent on the quality and accuracy of sensory and estimated data provided to the controllers. Tire forces and vehicle states such as lateral and longitudinal velocities are required information for most vehicle control systems. However, there are challenges associated with efficient estimation of tire forces and vehicle states. Furthermore, changes in vehicle inertial parameters, road grade, and bank angle all have major influences on both tire forces and vehicle states. Efficient identification of these parameters requires sufficient information about a set of vehicle states and tire forces. This duality relationship mandates the development of efficient methods for simultaneous estimation of tire forces, vehicle states, and vehicle and road parameters.

This research proposes the design of an integrated estimation structure that can simultaneously estimate tire forces, vehicle velocity, vehicle inertial parameters, and road angles. The proposed structure is robust against variations in tire parameters because of tire brand, wear, and road friction coefficient. The methods developed in this thesis are all validated experimentally on multiple vehicle platform.

Acknowledgements

I would like to express my deep appreciation to my supervisors, Prof. Amir Khajepour and Prof. William Melek, for their valuable guidance, patience, support and constant encouragement during my research.

I also wish to thank my committee members, Prof. Steven Waslander, Prof. Soe Jeon, Prof. Dana Kulic and Prof. Bruce Minaker for reviewing and improving my thesis.

I thank my friends, Reza Zarringhalam and Saber Fallah, and colleagues at the Mechatronic Vehicle System Laboratory for all their support during my studies at University of Waterloo.

Sincere thanks to the project sponsors, Automotive Partnership Canada, Ontario Research Fund and General Motors for their technical and financial support. In addition, I also wish to thank for the comments that I have received from Dr. Bakhtiar Litkouhi, Dr. Shih-Ken Chen and Dr. Nikolai Moshchuk in the GM Research and Development Center in Warren, Michigan to improve my research.

I am grateful to my parents, my brothers and sister for supporting me spiritually during my life.

Finally, I am deeply indebted to my darling wife, Fattaneh, for her endless love, encouragement and support.

Dedication

To Fattaneh

Table of Contents

List of Figures

List of Tables

Chapter 1

Introduction

In this chapter, the scope and motivation behind this research are discussed. Objectives of this research are introduced, followed by a chapter description of the thesis contents.

1.1 Motivation

Most vehicle control systems utilize vehicle states such as longitudinal and lateral velocities, vehicle body angles, and tire forces (longitudinal, lateral, and vertical forces) in order to stabilize the vehicle and achieve the desired cornering performance. Advanced driver assistance systems (ADAS), electronic stability control (ESC), holistic corner control (HCC), and rollover avoidance systems are examples of such control systems.

Vehicle states and forces depend on vehicle parameters, road angles and condition, and the vehicle maneuver. These parameters can be divided into three categories:

1- **Vehicle inertial parameters:** These parameters include the vehicle mass, location of the vehicle's center of gravity (COG), and moment of inertia matrix, and can change. Vehicle mass is the most important parameter among the vehicle inertial parameters. It is reported that in light passenger vehicles, four occupants can result in a 20% change in the inertial properties, which affects the handling characteristics of the vehicle [1].

2- **Road bank angle and road grade:** Vehicle controllers need to have these angles to generate accurate and proper commands for the vehicle contrtol stability. In addition, accurate estimation of the road grade can be used for transmission shift scheduling, vehicle longitudinal control, cruise control, and pitch angle estimation algorithms. Estimation of bank angle is useful for roll avoidance systems, lateral velocity estimation algorithms, and roll angle estimation algorithms.

3- **Tire-road friction coefficient:** The tire-road friction coefficient directly affects lateral and longitudinal tire forces that impact the vehicle handling performance. The investigation of this parameter is out of the scope of this thesis.

Vehicle control systems often use fixed values for these parameters because of the associated difficulty and costs of real time estimation. Fixed parameters lead to a conservative controller design for the worst-case scenarios. Online identification of these parameters can significantly improve the performance of both the estimator and controller. However, because of the inherent interdependency between tire forces, vehicle states, vehicle inertial parameters, and road parameters, these problems cannot be solved separately.

1.2 Objectives

The main objective of this thesis is to develop an integrated estimation system that uses sensory data and vehicle dynamics to simultaneously estimate the vehicle states (longitudinal and lateral velocities of COG) and tire forces (lateral, longitudinal, and vertical forces) as well as identify vehicle inertial parameters and road angles (road grade and road bank angle). The estimation and identification algorithms will be implemented on a real car to validate the accuracy and effectiveness of the proposed methods.

1.3 Overall estimation/identification structure

Figure 1.1 shows the closed-loop of a general vehicle control system, as well as the integrated estimator that reconstructs the tire forces (longitudinal, lateral, and vertical tire forces), vehicle states (longitudinal and lateral velocities, roll and pitch angles of the vehicle body), vehicle mass, road bank angle, and road grade.

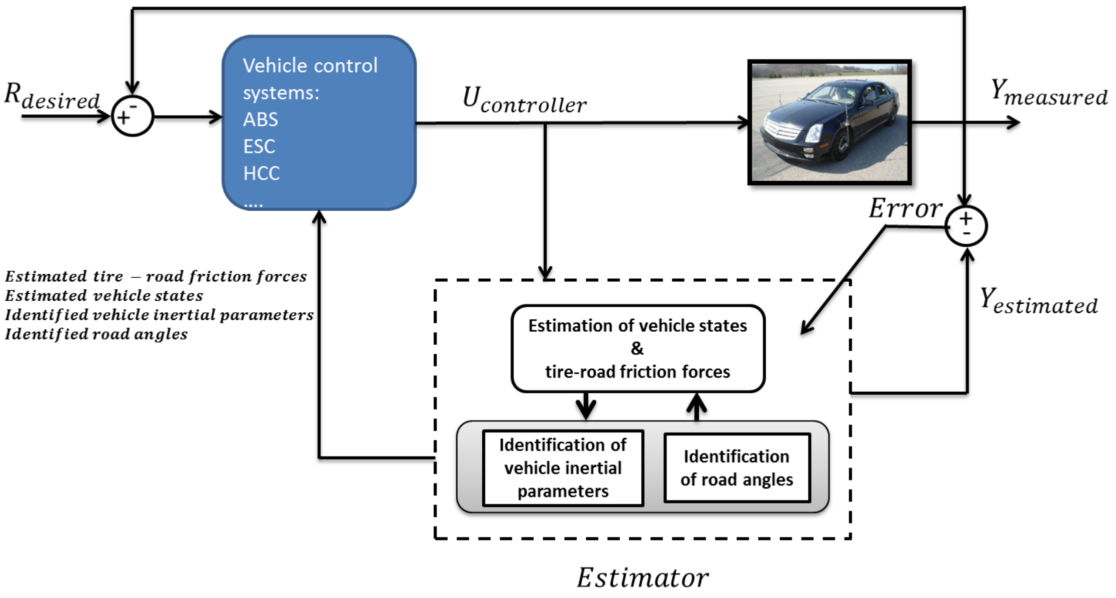

Figure 1.1. Closed loop of vehicle control system and communication between controller and estimator

The focus of this thesis is on the development and validation of the Estimator block in the above figure. Figure 1.2 shows more details about this block. This figure clearly illustrates that the developed integrated estimation structure uses a parallel scheme to estimate states, forces, and parameters simultaneously. At each time step, the estimation block uses identified parameters in the previous step as constants, and the parameters' identification block uses states and forces estimated in the previous step as known values. Therefore, the outputs of this parallel scheme would be the estimated states and tire forces plus the identified vehicle inertial parameters at each time instant.

In this thesis, the vehicle states, tire forces and parameters are not estimated using a single estimation algorithm. Each estimation block uses a separate algorithm to estimate a vehicle state, tire force in one direction, or a single vehicle parameter. This method is chosen because of the modularity of this estimation approach. Each of these blocks can be replaced with a new block which uses a different estimation algorithm or a different sensor set.

The significant constraint on the vehicle control process shown in Fig 1.1 is the limitation on the time available to estimate the required signals in order to generate the $U_{controller}$. This is referred to as the control loop frequency and in this thesis it is required to be 5 ms to run the tests that will be presented in Chapter 5. Hence, for each control command update cycle, all of the states, forces, and parameters need to be estimated in 5 ms and send to the controller. The estimation approach proposed is effective in the presence of this computational time constraint.

The required sensory data for this algorithm are tabulated in Table 1.1. A 6-axis inertial measurement unit (IMU), anti-lock braking system (ABS) sensor, steering wheel angle sensor, and wheel hub sensor are the devices employed to provide accurate measurements for the algorithm. The accuracy of some of these sensors is verified by comparing their outputs with other available sensors that measure the same physical quantities. For example, the accuracy of the measured longitudinal, lateral accelerations and yaw rate with the 6-axis IMU is verified through a comparison between the 6-axis IMU outputs and a 3-axis IMU outputs. The accuracy of the measured velocity with the GPS has been verified through the comparison between the GPS outputs and the measured velocity using an optical sensor.

The 6-axis IMU measures the longitudinal and lateral accelerations and the yaw rate of the vehicle which are similar to a 3-axis IMU's outputs. The special reason for using 6-axis IMU is the ability to measure additional signals which are the roll rate and pitch rate of the vehicle and vertical acceleration of the vehicle body. The meaasured pitch rate and roll rate are used to accurately estimate the roll and pitch angles of the vehicle body and to identify the road bank and grade angles. In addition, the vertical acceleration is used in the vertical tire force estimation algorithms.

In conventional vehicles driving torques can be calculated using powertrain specifications [2]- [3], and braking torques can be calculated using measured pressure in braking system [4]. Furthermore, the wheels' torques (driving and braking torques) are available in electric vehicles using electric motor drives and brake pressure.

The rates of changes in the vehicle parameters ane road angles are not fast. It is assumed that the vehicle mass is constant in each journy. When the vehicle mass is identifed, its value is fixed for the remainder of journey in the other estimation algorithms. The road angles are not constant and may change in each journey. Therefore, the road angles identification algorithm needs to estimate the angles dynamically throughout a given journy.

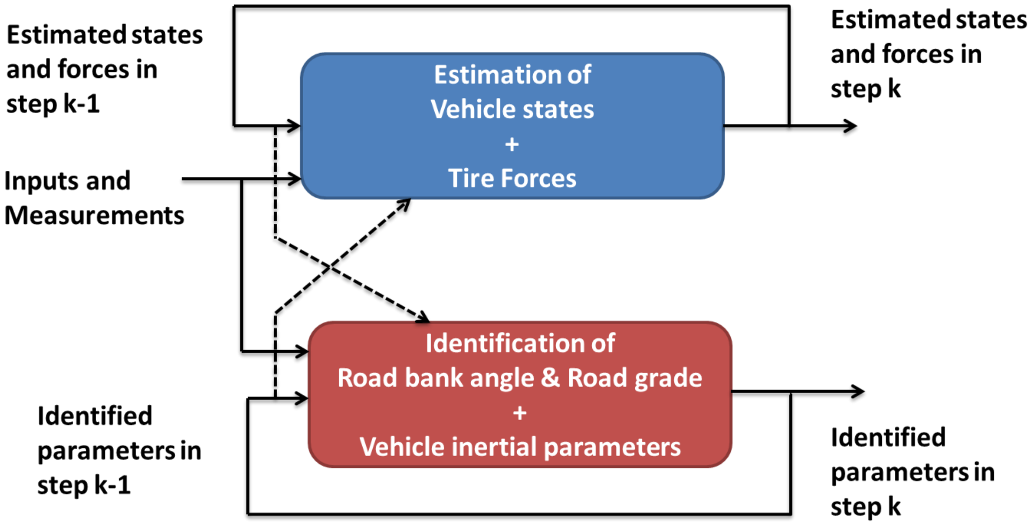

Figure 1.2. Integrated estimation structure

Table 1.1. Required sensory data and their definitions

Definition	Sensor
Longitudinal acceleration	6-axis IMU
Lateral acceleration	6-axis IMU
Vertical acceleration	6-axis IMU
Yaw rate	6-axis IMU
Roll rate	6-axis IMU
Pitch rate	6-axis IMU
Wheel angular velocity of each wheel	ABS sensor
Steering wheel angle	Steering wheel angle sensor
Wheels' torques	Wheel hub sensor

1.4 Thesis organization

The current thesis is organized as follows:

Chapter 2: In this chapter, the literature on the estimation of tire forces and vehicle states, identification of vehicle inertial parameters, and identification of road bank angle and road grade is reviewed. The chapter covers the estimation methods that have been recently published in the literature. Differences between this work and the work of other researchers are discussed.

Chapter 3: In this chapter, the vehicle state estimation and tire force estimation algorithm are presented in detail.

Chapter 4: In Chapter 4, road bank and grade angle identification algorithms are fully described. According to the sensitivity analysis, the vehicle mass is identified as an important parameter needed to be identified. Then, a vehicle mass identification algorithm is developed.

Chapter 5: This chapter introduces the test vehicles and the devices used for collecting data and experimental studies. Following this, experimental studies to validate the proposed integrated estimation methods are presented.

Chapter 6: This chapter summarizes the main contributions of the research. It also provides recommendations for future works.

Chapter 2

Literature survey

This chapter presents the relevant literature on estimation of tire forces and vehicle states, and identification of vehicle mass, road bank angle and road grade. The contributions of this thesis relative to recent development in the literature are discussed.

2.1 Estimation of tire forces and vehicle states

This section discusses the different existing tire force and vehicle state estimation algorithms in the literature.

2.1.1 Estimation of tire forces

There are various studies on estimation of vehicle tire forces in the literature using analytical tire models such as linear [5], Dugoff's model [6], or semi-empirical models including the Pacejka's tire model [7]. However, these tire models have parameters that should be tuned based on experimental data collected in different tests and for different road conditions. For example, Pacejka's tire model - one of the most popular tire models - has seven parameters that change for different load and road conditions [7]. Therefore, using tire models and tuning the tire parameters for each road and load is a challenging task. Looking at the market, it is easy to figure out that the sensors to measure the tire forces are quite expensive. For example, a transducer that can measure six components (three forces and three moments) currently costs about €100,000 [8].

One potentially advantageous solution for manufacturers is the estimation of these three elements of tire forces (longitudinal, lateral, and vertical - see Figure 2.1) based on the dynamic behavior of vehicles. First, this method can estimate the tire forces without any additional tests and tuning. Second, this method is robust against changes in road conditions and tire parameters. Consequently, control systems can rely heavily on these tire force estimation schemes to achieve the desired response. The existing literature related to estimation of tire forces is reviewed in the next section.

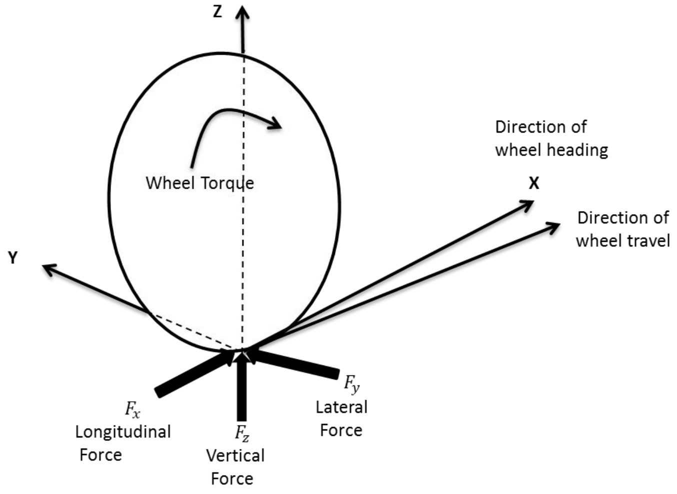

Figure 2.1. Tire forces acting on the tire.

2.1.1.1 Estimation of vertical tire Forces:

In the research literature, vertical tire forces have been estimated by using equations that represent the summations of longitudinal and lateral load transfer and the static loads on each wheel. Here, two of such methods are reviewed. Dumiati *et al.* in [9] used a four wheel vehicle model to estimate the vertical forces based on a Kalman filter (KF). They applied three observers; the first for lateral load transfer estimation, which is based on roll dynamics, and two other observers derived from linear and nonlinear vehicle models are used to estimate the vertical forces. In the estimation of these forces, they assumed that the changes in these forces are slow, thus justifying the use of the random-walk model for estimation of these forces. The measurements employed were lateral acceleration, longitudinal acceleration, suspension displacement, roll, and yaw rate. The experimental results demonstrated the effectiveness of the algorithm. Cho *et al.* [10] used summations of longitudinal load transfer, lateral load transfer, and static normal force to estimate the vertical forces. This estimator needs the observed or measured longitudinal and lateral accelerations and roll states to be fairly accurate.

These algorithms are tested and the experimental results show their effectiveness. However, they are not accurate when the vehicle is moving on the road with bank and grade angles [9]-[10], or when extra weight is added to the vehicle [10].

2.1.1.2 Estimation of longitudinal and lateral tire forces

Most research papers have used wheel dynamics, or a combination of wheel dynamics and vehicle longitudinal dynamics to estimate the longitudinal tire force acting on each wheel. However, the estimation of lateral tire force acting on each wheel is a bigger challenge. According to the handling dynamics equations, the system is not observable when lateral tire forces are used as states of the system, and only the lateral tire force acting on each axle is being estimated.

W. Cho et al. [10] designed a tire longitudinal force estimator based on a wheel dynamics model that used a wheel's angular velocity, braking pressure, and shaft torque data. An energy function that used wheel angular velocity errors was defined, and the goal of the designed estimator was the minimization of the defined energy. Subsequently, the lateral tire forces acting on the front and rear axles were estimated by using the estimated longitudinal forces. Moreover, to estimate the longitudinal and lateral tire forces for large slip ratios, they combined the estimation of lateral and longitudinal tire forces by using a random-walk Kalman filter.

Two algorithms were proposed in [11] to estimate longitudinal tire force based on the wheel angular velocity dynamics and longitudinal vehicle dynamics. In the first algorithm, the authors used the combination of wheel angular velocity dynamics and a random-walk model for estimating longitudinal tire force to avoid the need to numerically differentiate the wheel angular velocity. The second algorithm employed the longitudinal acceleration, longitudinal velocity (provided by global position system (GPS) measurements), wheel angular velocities, and derivative of the angular velocities as the measurements to estimate the longitudinal tire force. They showed that there are five unknowns in the five equations: four equations for four wheel angular velocity dynamics, and one equation for longitudinal vehicle dynamics. By solving this set of equations, the longitudinal tire forces were estimated.

The sliding mode observer (SMO) is another option for estimating longitudinal tire force [12]-[13]. The effectiveness of the algorithm was investigated by simulation results. However, wheel angular position measurements were used as the sensory data; these are not commonly measured in commercial vehicles. In addition, the estimator performance is dependent on the observer gains that need to be tuned for different maneuvers.

Estimation of longitudinal and lateral tire forces based on the vertical tire force distribution has been investigated in [9]. According to this approach, the lateral and longitudinal tire forces acting on the front and rear axles were initially estimated. This was followed by the use of a defined coefficient, which in this case was the vertical tire force acting on the wheel divided by the vertical tire force acting on the related axle. Next, this coefficient was used to estimate the lateral and longitudinal forces acting on the left and right wheels.

K. Huh [14] assumed that the time derivative of the lateral tire force is proportional to the roll rate, and the proportional constant is a slowly time-varying term. Using this assumption, the lateral tire force acting on each axle can be estimated by using dynamic equations related to a vehicle with four degrees of freedom (DOF) (longitudinal and lateral motion, yaw and roll motion) to design an EKF. Additionally, they distributed these lateral forces between the left and right wheel by using vertical tire force distribution. The simulation results revealed that the estimated results follow the true lateral tire forces relatively closely.

Based on existing literature, and to the best of our knowledge, no research considers the changes in the vehicle mass, road bank and road grade angles that can occur during each journey when designing tire force estimation methods. The subsequent sections provide a review of research literature that addresses the identification of vehicle parameters.

2.1.2 Estimation of roll and pitch angles

Roll angle information is necessary for accurate representation of a lateral dynamic model of the vehicle. In addition, this angle can be used to recognize and avoid rollover of the vehicle during harsh maneuvers. Longitudinal dynamics of the vehicle can be described more accurately by incorporating information about the pitch angle of the vehicle body. The information about the pitch angle can be used to identify the road grade angle and estimate vehicle longitudinal velocity more accurately.

Roll and pitch angles of the vehicle body can be calculated/estimated with several sets of sensors. Suspension-deflection transducers can be used to estimate roll and pitch angles [15]. However, these are not common sensors on vehicles without semi-active or active suspension systems. Additionally, [16] shows that using only lateral acceleration signal is not enough to accurately estimate the roll angle, especially when the vehicle mass changes or when the vehicle is excited in the lateral direction very fast. The same problem exists if only the longitudinal acceleration is used to estimate pitch angle. An adaptive estimation structure to estimate roll angle is proposed. The authors used roll rate and lateral acceleration signals as the measurements signals. In [17], an algorithm is proposed to estimate roll angle of the vehicle body using the measured lateral acceleration and roll rate signals. Because of the relations used in [17], this algorithm is not reliable when the rate of change in the lateral velocity, or the pitch angle of the vehicle body are large. A complicated estimation structure that used a six axis IMU, steering wheel- angle sensor, and wheel speed sensors to estimate roll and pitch angles of the vehicle body is developed in [18]. This structure estimates the vehicle body angles by combining the velocity observer and longitudinal and lateral kinematic models. In [19], GPS and inertial navigation system (INS) sensors are used to estimate the roll angle of the vehicle body. By using the GPS signal, the sensors biases can be corrected so as not to deteriorate the performance of the proposed algorithm.

According to this review, there are challenging problems when estimating roll and pitch angles. These problems related to:

- Bias in sensory data
- Accuracy of the estimated roll and pitch angles in both transient and stationary situations
- Distinction between roll and bank angles, and distinction between pitch and grade angles

The proposed estimation structure needs to use a sensor configuration that can handle the abovementioned situations, and accurately estimate the roll and pitch angles needed for the tire force estimation algorithm, velocity estimation algorithm, etc.

2.1.3 Estimation of vehicle velocity

Accurate estimation of vehicle longitudinal and lateral velocity is vital for vehicle control systems such as the traction control system (TCS), and ESC. These velocities are not measured directly in commercial vehicles due to a lack of cost effective and reliable sensors. Therefore, developing a reliable algorithm for estimation of these velocities using existing measurements from stock sensors is necessary. Such algorithms should also be accurate in the presence of unknown inputs such as bank angle and road grade, which affect several sensor outputs such as longitudinal and lateral accelerations. Therefore, estimation of vehicle lateral and longitudinal velocity is a challenging problem considering additive sensors bias, unknown inputs, sensor noise, and possible wheel slipping.

In the literature, several vehicle velocity estimations have been proposed. Some approaches estimate both longitudinal and lateral velocities concurrently. For example, nonlinear observers designed in [20], [21], [22], [23], [24] have been used to estimate longitudinal and lateral velocity. [25] and [26] used a limited-bandwidth integration technique. In [27] an algebraic approach based on numerical differentiation and diagnosis has been proposed to estimate both longitudinal and lateral velocities. The kinematic model-based observer described in [28] is another approach to estimate the vehicle velocity in both longitudinal and lateral directions. Another observer used in the literature to estimate these velocities is extended Kalman filter (EKF) [29], [30], [31], [32].

There are also some articles on estimating vehicle velocity in one direction. For instance, a combination of fuzzy and sliding mode observer has been used in [33] to estimate the vehicle longitudinal velocity. In [34] and [35], algorithms are proposed to estimate the vehicle longitudinal velocity by using an accelerometer and wheel encoders. An adaptive nonlinear filter method [36] is another practical approach in the literature to estimate vehicle velocity by using information from wheel velocities. The Kalman filter([37], [38], [39]) is another type of estimator used to estimate vehicle longitudinal velocity.

In addition, there are reports that focus on estimation of sideslip angle to determine longitudinal and lateral velocities. For instance, [40] and [41] propose two methods to estimate longitudinal and lateral velocities and then use these estimates to obtain the side-slip angle. Furthermore, some of these approaches such as [26], [28], [29],[30], [32],[38] have not been tested and verified with a real vehicle.

There are two common problems in the above-mentioned approaches that need to be considered in the vehicle longitudinal and lateral velocity estimations. First, accelerometer signals usually have additive bias, which often introduces errors in the estimated velocity. This problem is not usually considered in the literature. Most reports assume that the lateral acceleration signal does not have bias. Also, some reports such as [21], [22] and [41] used a high-pass filter to deal with the accelerometer bias and road bank angle that are added to the measured signal. However, one needs to consider that such bias and unknown road bank angle are not static and they often change. Therefore, using a fixed high-pass filter is not an effective way to mitigate this problem. Secondly, when a wheel is slipping or locking, the angular velocity of such a wheel is not a reliable measure for vehicle velocity estimation. This could happen often on low friction surfaces or when ABS is on. In [37] and [42] fuzzy logic was used to decrease the effect of wheel slippage. In [43], a method has been developed to estimate the longitudinal velocity using wheel speed measurements and a longitudinal acceleration signal. In [21]-[22], the authors propose a Luenberger observer whose gains are functions of longitudinal acceleration and wheel speeds to decrease the effect of wheel slippage. In [38] and [39], the authors proposed an adaptive Kalman filter to estimate the longitudinal velocity. However, they ignored the effect of lateral velocity in their estimation algorithm. And, [39] is not applicable for conventional vehicles because the observer requires wheels' torques.

The proposed velocity estimation structure in this thesis will address these two challenges:

1- Additive bias in the measured acceleration signals

2- Effect of slippage in the estimated velocity

In the next section, the parameters that impact the vehicle state estimation are discussed and the relevant literature of identification of these parameters is reviewed.

2.2 Identification of parameters

Vehicle inertial parameters including center of gravity location, vehicle mass, and moment of inertia matrix are all parameters that play a role in determining vehicle states and tire forces. Moreover, distribution of the tire forces and vehicle states will change when the slope of the road varies. This section discusses the different parameter identification methods used in the research literature to identify these parameters.

2.2.1 Identification of vehicle inertial parameters

The stability and desirable performance of a vehicle under different loading conditions are a necessary requirement in the development of active vehicle control systems. Depending on how the vehicle is loaded, its inertial parameters, including mass, moments of inertia, and spatial components for locating the center of gravity (COG), can have different magnitudes. Figure 2.2 illustrates the parameters related to COG location.

It is reported that four occupants can result in a 20% change in the inertial properties of light passenger vehicles [1]. The effects of possible changes in inertial vehicle parameters on handling, ride, braking, and traction performance are widely investigated in research literature [44]-[45].

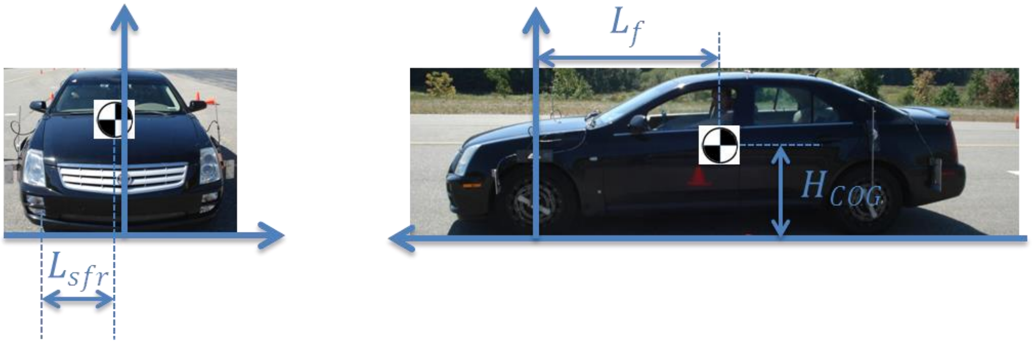

Figure 2.2. Center of gravity location.

Rather than using nominal values of vehicle inertial parameters, the performance of vehicle stability controllers and driving assistant systems can be improved by proper online identification of vehicle inertial properties.

There are practical requirements for the feasibility of an inertial parameter identification module for an economy-priced vehicle [46]:

- **Simplicity:** to run in real time despite onboard processing limitations
- **Accuracy:** to estimate inertial parameters within a 3-5% error bound

- **Speed:** to detect changes in a vehicle's loading immediately after it is started and driven
- **Reliability:** to operate successfully despite any instrumentation failures
- **Robustness:** to handle disturbances (e.g., road grade) and variations in vehicle dynamics (e.g., drag)
- **Cost:** to be economically feasible when implemented in a car.

Research that is currently available suggests a variety of strategies that can be used for the development of online vehicle inertial estimators. These algorithms can be classified into four major categories based on the dynamic properties used for estimation. These categories are: lateral/yaw dynamics [47]; longitudinal dynamics [48], [49], [46], [50]; suspension dynamics [1],[51]; and combinatory approach [52], [53], [3], [54].

Best and Gordon [47] developed an extended Kalman filter (EKF) that used lateral measurements for the estimation of vehicle states and vehicle mass. The simulation and experimental results showed that the EKF can be used as an identifier. They have assumed the vehicle's lateral velocity (or body side slip angle) as a measurement that can be measured by an integrated GPS/inertial body motion measurement system. This is not a commonly measured signal in commercial vehicles.

Several methods have been used in the research literature to identify the vehicle mass based on the longitudinal vehicle dynamics. These methods have used the direct dynamic relationship between mass and longitudinal acceleration of the vehicle. Bae et al. [48] proposed a recursive least squares to identify vehicle mass and aerodynamic drag based on longitudinal forces, longitudinal acceleration, and GPS-based road grade measurements. This method requires uncommonly measured signals on commercial vehicles such as GPS measurements. Vahidi et al. [49] used a recursive least squares method to estimate vehicle mass and road grade. Since these two parameters vary with different rates, the authors used two forgetting factors to improve the RLS performance for this application.

To estimate vehicle mass, H. K. Fathy et al. [46] used the notion that inertial forces dominate longitudinal vehicle dynamics, while other resistive forces such as rolling resistance, drag force, and road grade force only influence the vehicle at low frequencies. The researchers designed a fuzzy supervisor to analyze the sensory data and used a recursive least squares algorithm to estimate the vehicle mass.

A vehicle's inertial properties directly affect vertical deflections of the suspension system. Availability of the sensors such as linear variable differential transformers (LVDTs) provides the proper tools to identify vehicle inertial parameters based on suspension sensory data. Rajamani and Hedrick [51] proposed adaptive observers for the combined estimation of a vehicle's states and a number of vehicle parameters including mass.

In [55], the authors proposed a parallel mass and road grade identification algorithm. They assumed that the torques of the driven wheels are available, and longitudinal acceleration and longitudinal velocity are available signals. The algorithm identifies these two parameters with separate estimators. They showed that the parallel mass and road grade algorithm has the better performance in comparison with RLS and EKF algorithm. The algorithm is active when vehicle is moving in the straight line.

Rozyn and Zhang [1] proposed a method based on modal analysis to extract the sprung mass, damping ratios, and mode shapes. They used a 12-DOF vehicle model as the vehicle simulation model, and prepared sensory data from this high order model. Next, a simplified 3-DOF vehicle model was employed to estimate the inertial properties. This was done by using the least squares algorithm and known equivalent stiffness of suspension systems. They used three corner accelerometers to provide the necessary information for the estimation algorithm. The method cannot accurately estimate the inertial parameters in low-speed maneuvers because of the wheelbase filtering effect, which causes a delay between the front and rear measured acceleration signals.

A combination of the aforementioned approaches can be used to estimate vehicle inertial parameters. H. Lee et al. [52] presented a model-based mass estimation that used the combination of powertrain and vehicle longitudinal dynamics equations to identify vehicle mass. The vehicle mass was only accurately estimated when certain special conditions were satisfied, such as longitudinal acceleration above 0.1g, or engine RPM above 1500rpm. The other approach is the combination of longitudinal and lateral vehicle dynamics, which has been investigated in [53]. One identifier is used only when vehicle is excited in longitudinal direction, and vehicle mass identified by employing the recursive least square. The other estimator is only used when vehicle is excited in the lateral direction. Therefore, vehicle lateral dynamics are used and RLS applied to estimate the vehicle mass. Since this algorithm requires the use of the estimated lateral tire forces, a linear tire model was used. Moreover, the road bank angle, which has an effect on lateral vehicle dynamics, was neglected. S. Solmaz et al. [3] presented a methodology based on a combination of the vehicle lateral and roll dynamics to estimate the longitudinal and height positions of the COG. In their estimation procedure, they designed multiple model schemes by using possible measures of each unknown parameter, followed by the use of a cost function to find the model with the least identification error. They assumed longitudinal velocity as a constant parameter and used a linear tire model. The accuracy and speed of convergence in this method is dependent on the number of models and perfectly tuned cost function parameters. Another approach for identification of the inertial parameters uses genetic algorithm [54]. This method cannot be applied for online parameter estimation because of its large computation time.

According to this review, vehicle mass, location of the COG (in three directions: longitudinal, lateral and vertical), yaw moment of inertia, and roll moment of inertia are the parameters that researchers tried to identify. In the scope of this thesis, it is important to do a sensitivity analysis and recognize the parameters that have significant effects on the specific application, and then develop identification algorithms for them.

2.2.2 Identification of road bank angle

It is common to encounter sections on rural roads or poorly shaped curves on regular city roads that have insufficient bank angles. Furthermore, entrance or exit regions of highways usually have sections with a bank angle. It is difficult to measure this angle because it is coupled with other vehicle states such as roll angle and lateral acceleration obtained from sensory data. Equation (2-1) shows the measured lateral acceleration of road bank angle:

$$\boldsymbol{a_{y,m}} = \dot{\boldsymbol{v}}_{\boldsymbol{y}} + \dot{\boldsymbol{\psi}}\boldsymbol{v_x} + \boldsymbol{g}\,\boldsymbol{sin}(\boldsymbol{\phi_r} + \boldsymbol{\phi_v}) \tag{2-1}$$

where $a_{y,m}$ is the measured lateral acceleration, $\dot{v}_y$ is the time-derivative of lateral velocity, $\dot{\psi}$ is yaw rate, u is the longitudinal velocity, ϕ_r is road bank angle, and ϕ_v is the vehicle roll angle. Equation (2-1) shows that the roll angle and road bank angle are coupled, as Figure 2.3 illustrates. Differentiating the roll angle estimation from the bank angle estimation is often a challenge, as is differentiating the estimation of road bank angle from the estimation of the vehicle lateral velocity. This is because both of them can change the lateral accelerometer’s signal at a similar rate. Therefore, the estimation of this angle provides valuable information for vehicle control systems, while also helping to distinguish the effects of bank angle and time derivative of the lateral velocity on the measured lateral acceleration [5]. According to the literature, the road bank angle can be estimated using the kinematic-based method [56], [57], or by combining kinematic-based and model-based methods [58], [59], [60], [61], [62], [5], [60] , [63].

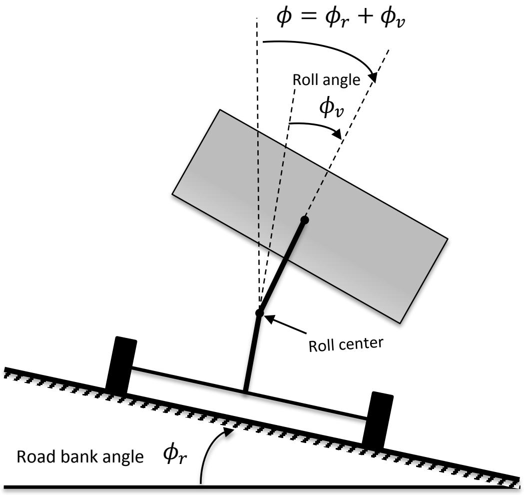

Figure 2.3. Vehicle roll model on bank road

One method to estimate the road bank angle is using the kinematic-based approach. To the best of this author's knowledge, [56],[57] are the two papers that introduced this method. Since vehicle parameters such as vehicle mass, center of gravity location, and tire parameters are not used in the kinematic-based method, it is robust against changes in these parameters. Understandably, errors in the sensory data undermine the estimated states [41],[56]. For example, a drift appears in the estimated states due to the effect of integration bias error. D. Piyabonkarn et al. [56] estimated the road bank angle by using the measurements from lateral and vertical accelerometers. They extracted a kinematic relation between road bank angle and the sensory data. However, the proposed method in [56] does not have the ability to separate the roll angle from the road bank angle. In fact, they estimated the summation of the roll and bank angle. In [57], a kinematic relation related to the lateral accelerometer was used to estimate the road bank angle via the time derivative of the estimated vehicle side-slip angle. Therefore, the accuracy of the estimated angle depends on the accuracy of the estimated side-slip angle and its derivative term.

Another method that early researchers employed to estimate bank angle uses a combination of vehicle model-based and kinematic-based methods [58], [59], [60], [61], [62], [5], [60] , [63]. Compared to the kinematic-based method, this approach is sensitive to changes in vehicle and tire parameters, but is robust against the sensor noise [21]. Different types of estimators have been used in the literature to estimate the road bank angle through the following combination: extended Kalman filter (EKF) [58], [21], [41], unknown input observers (UIO) [59], [60], dynamic filter compensation (DFC) [61], and proportional integral observer (PIO) [5],[62],[64].

An approximate equation was proposed by [27] that presented the relation between roll angle and lateral acceleration; therefore, this additional equation helped differentiate the estimation of roll angle from the road bank angle. The EKF was used as the estimator. A practical cahllenge in this method is tuning the tire model's parameters for each road condition. Using fixed vehicle inertial parameters such as constant vehicle mass is another drawback of this algorithm.

Tseng [61] proposed a practical approach to estimate the road bank angle based on measured signals. He introduced a dynamic factor based on the system transfer functions and sensory data. However, this approach has its limitations. For example, it is not accurate when there is a road with a low friction coefficient and bank angle. Furthermore, the method used a differential global position system (DGPS), which is uncommon in commercial vehicles. As proven by [5], this algorithm is also not robust against changes in tire parameters.

The other approach that has been used to estimate the bank angle is an unknown input observer (UIO) [59]. It is extremely sensitive to the output changes [5]. There is a time derivative of the output that undermines the performance of the observer with the existence of noises on the sensory data, a common problem in real time applications. In [59], a nonlinear UIO used the kinematic relation of lateral acceleration and vehicle lateral dynamics to estimate the road bank angle. There is an inverse term (the inverse of measurements divided by lateral velocity) in this approach that can lead to unstable behavior of the estimator during maneuvers with large side slips [59].

In [32], road bank angle was considered as a disturbance that can be estimated by applying a disturbance observer. The weakness of this approach is using the DGPS measurements which is not a common type of sensor in commercial vehicles [5]. Moreover, the sampling rate of GPSs (1~5 Hz) available in the market is not high enough when compared to other common sensors such as the inertial measurement unit (IMU). Additionally, authors [5] have completed a robustness analysis which proved that the estimated road bank angle has a steady state error if model uncertainties exist.

Proportional integral observer (PIO), which is a modification of Luenberger observers, not only uses the information of estimation error, but also data from previous time instances. It does so by applying the integral of the error [65]. The research papers that have applied this observer to estimate road bank angle are reviewed next. In [62],a two degree of freedom vehicle model was employed, and the road bank angle was considered to be an unknown input. Next, an observer that combined UIO and PIO has been designed to make the road bank angle estimation procedure insensitive to disturbances. This algorithm cannot separate the road bank angle from the roll angle, as the summation of these angles is estimated. Moreover, the approach is not robust against uncertainty in vehicle or tire parameters. J. Kim et al. [5] have completed investigations about the robustness of various estimation algorithms against changes in tire parameters, such as dynamic filter compensation algorithm and UIO. They used a proportional integral observer whose gains were designed by the H_∞ filter, and used game theory to estimate the road bank angle. Although they showed that the algorithm worked accurately in the selected maneuvers that had constant longitudinal speed, there are still some weaknesses in this approach. Firstly, they used longitudinal velocity as one of the measurements; however, this sensory data is actually uncommon in commercial vehicles. They also did not investigate the robustness of the algorithm against changes in vehicle inertial parameters. Also, due to the use of the linear tire model, the algorithm cannot accurately work in the nonlinear region of tire forces. In [64], a PIO is designed, and its gains are calculated by linear matrix inequality (LMI). Although the authors are able to estimate the road bank angle using such a method, the estimation is only valid for known vehicle inertial parameters and tire parameters.

2.2.3 Identification of road Grade

An accurate model of the longitudinal vehicle dynamics provides reliable data for vehicle control systems such as adaptive cruise control. Although there are well defined longitudinal vehicle models, the model parameters are not exactly known, and their variations can change the performance of the control system. Road grade is one of the parameters whose variation directly affects the vehicle longitudinal dynamics. Moreover, knowing this angle can help manage fuel consumption [66]. There is no sensor in commercial vehicles that can measure this angle. In the literature, employing a well-designed estimator is the method that is most referred to identify the road grade. Distinction between the road grade and pitch angle during acceleration or braking is another challenging problem that needs to be solved. Equation (2-2) illustrates the coupling between these two angles. It also presents the challenges regarding the estimation of road grade and the estimation of longitudinal velocity by using measured longitudinal acceleration. This is particularly difficult because both terms influence the longitudinal accelerometer signal with similar rates. The relation between abovementioned variables is defined with

$$\boldsymbol{a_{x,m}} = \boldsymbol{\dot{v}_x} - \boldsymbol{\dot{\psi} v_y} - \boldsymbol{g sin}(\boldsymbol{\theta_v} + \boldsymbol{\theta_r}) \tag{2-2}$$

where $a_{x,m}$ is the measured longitudinal acceleration, $\dot{v}_x$ is the time-derivative of longitudinal velocity, v_y is the lateral velocity, θ_v is the vehicle pitch angle, and θ_r is road grade. Figure 2.4 shows the vehicle on a sloped road and depicts the angles in **(2-2)**.

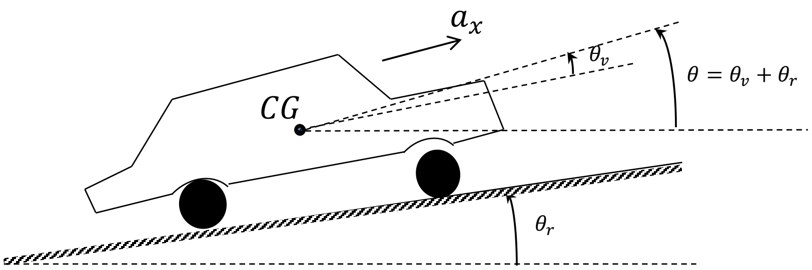

Figure 2.4. A vehicle on a sloped road

In most road grade estimation algorithms in the literature, the pitch angle is ignored during maneuvers on the sloped road. Below, the literature that considered the road grade is reviewed.

In [2], two different methods were used to estimate the road grade. The first method used a kinematic relation and specifically measured longitudinal acceleration and vehicle speed. The second method used road grade estimation based on the vehicle longitudinal velocity and wheel torque, which was estimated using information from the powertrain system. The authors concluded that the first method is more expensive because it requires the use extra sensors for the acceleration signal. Furthermore, the first method is also sensitive to noise and bias in the accelerometer signal. While the second method is not as expensive, its error is bigger, and it is also more sensitive to vehicle parameters such as mass. It should be mentioned that in both methods, a summation of the pitch and road angles is estimated.

The other benefit of road grade information is its application in fuel consumption, especially in high duty vehicles (HDVs) [66]. The recursive least squares algorithm is used in [49] to identify road grade for HDVs. Estimation of road grade during gear shifting has been investigated, and due to the existence of spikes in the estimated road grade, the authors proposed to turn off the estimator during and shortly after a gearshift in HDVs.

In [55], the authors compared the RLS and EKF identification algorithms for vehicle mass and road grade identification. They proposed a parallel mass and grade estimation algorithm, too. In their proposed structure, they assumed that the torques of the driven wheels, longitudinal acceleration, and vehicle velocity are available. The proposed method can only identify road grade when the vehicle is moving in a straight line. It cannot identify the road grade when the vehicle is excited in the lateral direction.

In [67], one gyro, one accelerometer, and a micro-electro-mechanical system (MEMS) barometer has been used to estimate the road grade. The advantage of this method is that the road grade is estimated without the use of a GPS signal. However, due to temperature, ventilation changes inside the car and variance of pressure measurements in different locations such as a tunnel, the accuracy of MEMS barometer measurements are subject to change [68].

J. Barrho et al. [69] designed a linear Luenberger observer to estimate the road grade by employing longitudinal velocity and acceleration data without using a GPS signal. They proposed a flow chart based on several ruls that were working according to measurments to distinguish driving situations (moving downhill\uphill and braking\accelerating). They linearized the vehicle model, and assumed that the longitudinal force acting on the COG, the rolling resistance force, and the wind force are known signals. This approach cannot distinguish between the pitch angle and the road grade because it estimates the summation of both angles.

Bae et al. [48] used a GPS system to measure the road grade with two methods: using two antennas differentially in the pitch plane, or by measuring the ratio of vertical to horizontal velocity using one antenna. In the first method, the authors used the low frequency portion of the measured signals by the differential GPS system to estimate the road grade. The first method is sensitive to change in the vehicle pitch angle, while the second is sensitive to vehicle bounce motions. Moreover, it should be mentioned that GPS signals are not reliable due to the propensity to outages and loss of signal in some situations[48]. The next section reviews papers that consider the estimation of both angles.

2.2.4 Combined identification of road grade and bank angle

In [70], a PI algorithm was used to estimate the road angles. The authors proved that by selecting appropriate gain tuned according to stability issues, the estimated angle can exponentially converge to the correct angle. The authors acknowledge that this algorithm cannot realistically handle the sensor noise and sensor offsets because these errors will be propagated to the estimated angle.

In [71], a switching observer was used to estimate vehicle states and road angles. The vehicle differential equations were divided into two sub-models, and EKF was applied for each block. These blocks communicate with each other in such a way that one estimator predicted its sub-model states, while the states related to the other sub-model were held fixed. This method decreases the complexity and computational efforts of the EKF. This method estimates two road angles (road grade and bank angle) without looking at GPS signals. However, as the authors in [71] stated, the observability and robustness of the switching observer should be investigated. Moreover, road grades can be estimated accurately when the vehicle yaw angle is known. Unfortunately, commercial vehicles do not yet have a sensor that can measure this angle.

2.3 Combined state and parameter estimation methods

Simultaneous estimation of the vehicle inertial parameters and vehicle states has been investigated in [72], [73], [74], [75]. If the vehicle parameters are used as additional states, then both the vehicle states and parameters can be simultaneously estimated by a single Unscented Kalman Filter (UKF). This approach is called the Joint Unscented Kalman Filter (JUKF), and is used in [72] and [76] to estimate vehicle states and certain vehicle inertial parameters, such as longitudinal location of the COG, roll and yaw moment of inertia, and vehicle mass. In [72], the simulation results showed that the parameters (mass, roll inertia, yaw inertia and longitudinal location of COG) can be identified. However, the large computation time limits the use of this algorithm for on-line application. Nuthong [73] used a JUKF to estimate an augmented state space that includes both the vehicle states and parameters. It was shown in [73] that a JUKF can estimate both vehicle states and parameters with computational efficiency and reasonable accuracy. However, the algorithm is not able to estimate the lateral tire force acting on each tire. Moreover, this method ignores the vertical tire forces that play a significant role in vehicle system dynamics. The algorithm can only work effectively if the parameters of the tire model are retuned for each road condition.

Wenzel et al. [74] implemented a dual extended Kalman filter strategy for the identification of vehicle parameters (vehicle mass, yaw moment of inertia, and longitudinal location of COG), and the state estimation of a 4-DOF vehicle handling model. Their approach was based on parallelization of two interacting extended Kalman filters, each solving one of the associated problems. The simulation results demonstrated that the estimated vehicle mass was within a range of 4% of the real value. However, this algorithm cannot accurately estimate the vehicle parameters for different road conditions such as wet and icy roads. This is because of its reliance on a tire model (Magic Formula tire model) that requires tire parameter tuning based on the road condition.

In [75], a dual structure was proposed that used UKF to estimate the vehicle states and vehicle mass, longitudinal COG location and yaw moment of inertia. The authors used a tire model that needs information about the road friction coefficient and tire parameters. In addition, the proposed structure is not robust against changes in the road angles.

2.4 Summary

This chapter presented and reviewed the relevant literature on the estimation of tire forces, vehicle inertial parameters, and road angles. In the literature, tire forces, vehicle states, vehicle inertial parameters, and road angles were generally estimated individually, although they were also estimated simultaneously in [72], [73], [74], [75], [76]. However, all of these references have used tire models to calculate the tire forces. Additionally, no prior work has explored the integrated estimation of tire forces, vehicle states and vehicle inertial parameters and road angles.

To address these concerns, this thesis propose an integrated estimation structure to simultaneously estimate tire forces acting on each wheel, as well as the vehicle states, vehicle inertial parameters, and road angles. This estimator is the primary contribution of this work. In the next chapter, the proposed integrated estimation structure will be presented in details.

Chapter 3

Vehicle state estimation and tire force estimation algorithms

In this chapter, the proposed vehicle state estimation algorithms including vehicle body roll and pitch angles as well as velocity estimation algorithms are fully presented. Furthermore, the developed algorithms for estimation of forces acting on each wheel in longitudinal, lateral and vertical directions are explained in detail.

3.1 Roll and pitch angle estimation algorithms

In this section, the proposed estimation algorithms for roll and pitch angles are introduced and explained in detail.

3.1.1 Overall estimation algorithm

A combination of the rates of changes of vehicle body angles and longitudinal and lateral accelerations of vehicle body are used to estimate the vehicle body's pitch and roll angles. Both longitudinal and lateral accelerations are available from 3-axis IMU in the electronic stability control unit. This algorithm requires two extra sensors which are roll rate and pitch rate.

Figure 3.1 shows the overall structure of the proposed observer for roll and pitch angles' estimation algorithms. In this figure, the terms in the parentheses are related to pitch angle estimation observer. This observer is utilizing a parallel structure. The bottom path is working based on the calculation of roll angle (pitch angle) in stationary conditions. The top path is working based on the integration of roll rate (pitch rate). Errors between low-pass filtered calculated angles in these two paths are multiplied by the observer gains, which are tuned according to the level of excitation in the lateral direction (longitudinal direction). The outcome signal will be used to correct the errors because of long term effects. In the next sections, the design of this observer is explained in more detail.

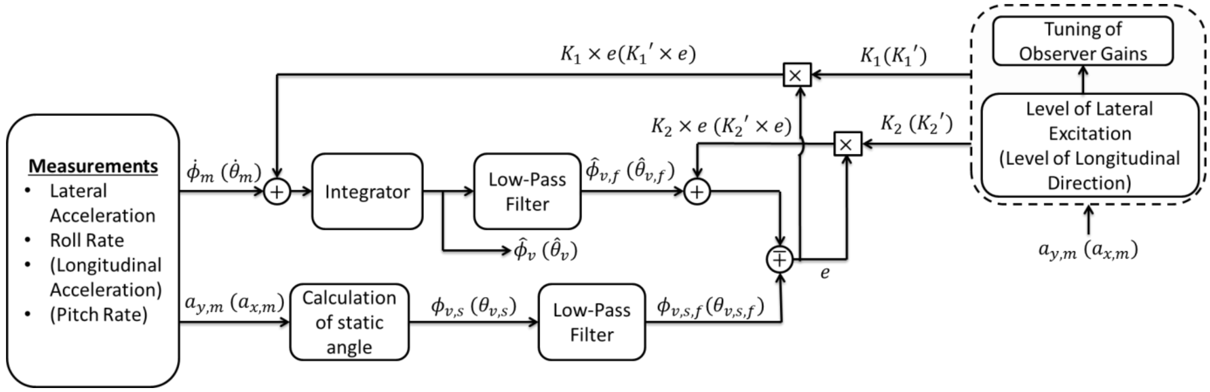

Figure 3.1. Overall structure of roll and pitch angle estimation algorithms

3.1.2 Roll and pitch angles' estimation algorithms

The measured roll rate ($\dot{\phi}_m$) can be written as [60]:

$$\dot{\boldsymbol{\phi}}_{\boldsymbol{m}} \approx \dot{\boldsymbol{\phi}}_{\boldsymbol{f}} + \dot{\boldsymbol{\phi}}_{\boldsymbol{v}} \tag{3-1}$$

where $\dot{\phi}_f$ is the roll rate of the vehicle frame and $\dot{\phi}_v$ is the roll rate of vehicle body. Furthermore, the measured pitch rate ($\dot{\theta}_m$) is

$$\dot{\boldsymbol{\theta}}_{\boldsymbol{m}} \approx \dot{\boldsymbol{\theta}}_{\boldsymbol{f}} + \dot{\boldsymbol{\theta}}_{\boldsymbol{v}} \tag{3-2}$$

where $\dot{\theta}_f$ is the pitch rate of vehicle frame and $\dot{\theta}_v$ is the pitch rate of vehicle body. Consequently, the integration outputs of (3-1) and (3-2) will not be the vehicle body roll angle and pitch angle. Therefore, it is necessary to separate the vehicle frame angles from these two measurements.

A 1-DOF roll plane model and a 1-DOF pitch plane model [77] can be used to estimate vehicle body angles when the vehicle parameters such as vehicle mass are known and the rate of changes in the vehicle body angles are not large [16]. Equations (3-3) and (3-4) represent the 1-DOF roll model and 1-DOF pitch model, respectively:

$$(I_{xx} + m_s H_{RC}^2)\, \ddot{\phi}_v = -C_\phi\, \dot{\phi}_v - K_\phi\, \phi_v + m\, a_{y,m}\, H_{RC} \tag{3-3}$$

$$(I_{yy} + m_s H_{PC}^2)\, \ddot{\theta}_v = -C_\theta\, \dot{\theta}_v - K_\theta\, \theta_v + m\, a_{x,m}\, H_{PC} \tag{3-4}$$

where I_{xx} and I_{yy} are the moment of inertia around x and y axis of vehicle body coordinate system, respectively. The distance between center of gravity and pitch center is H_{PC}, and H_{RC} is the distance between centre of gravity and roll center. It is assumed that H_{RC} , H_{PC} are known. The roll damping stiffness and roll spring stiffness are C_ϕ and K_ϕ. The pitch damping stiffness and pitch spring stiffness are C_θ and K_θ, respectively.

For most handling maneuvers the roll acceleration and roll rate terms $((I_{xx} + m_s H_{RC}^2)\, \ddot{\phi}$ and $(C_\phi\, \dot{\phi}_v))$ in (3-3) are small [16],[17]. Therefore, the roll angle of the vehicle body can be rewritten as

$$\phi_{v,s} = \frac{m H_{Rc}}{K_\phi}\, a_{y,m} \tag{3-5}$$

The calculated angle using (3-5) can be called the stationary roll angle. This stationary roll angle, $\phi_{v,s}$, is used to correct the drift that results from the integration of the measured roll rate signal. $\phi_{v,s}$ is then processed through a low-pass filter to remove the additive noises on the sensory data. The filtered output, $\phi_{v,s,f}$, is used to remove the drift using the following observer

$$\dot{\hat{\phi}}_v = \dot{\hat{\phi}}_m + K_1(\phi_{v,s,f} - \hat{\phi}_{v,f}) \tag{3-6}$$

$$\dot{\hat{z}}_1 = a\hat{z}_1 + b\hat{\phi}_v + K_2\, (\phi_{v,s,f} - \hat{\phi}_{v,f}) \tag{3-7}$$

$$\hat{\phi}_{v,f} = \hat{z}_1 \tag{3-8}$$

where a and b are the low-pass filter coefficients, $\hat{\phi}_{v,f}$ is the filtered estimated roll angle. The states in the observer are $\hat{z}_1$ and $\hat{\phi}_v$. The observer gains are K_1 and K_2.

The calculated error terms in (3-6) and (3-7) help to correct the drift in the estimated roll angle due to noise and bias in the measured roll rate. The integration of the measured roll rate will provide accurate estimation during transient motion of the vehicle body. Additionally, in stationary conditions, the abovementioned correction term prevents any drift in the estimated angle. Consequently, the developed observer accurately estimates roll angle in both stationary and transition conditions.

The absolute value of the derivative of lateral acceleration with respect to time is used to determine the level of lateral excitation. When this value is bigger than a pre-defined limit, it means that there is fast excitation in the lateral direction. When the value is smaller than the limit, it means that the vehicle excitation in the lateral direction is small. After recognizing the level of lateral excitation, the following rules are used to tune K_1 in the observer:

- When the excitation of the vehicle in the lateral direction is fast, then a small number is assigned to K_1. In this situation, the calculated roll angle with (3-5) is not accurate, therefore K_1 is set to a small value to reduce the contribution of the correction term in the output of the observer.
- When the excitation of the vehicle in the lateral direction is slow, then the correction term has more contribution. Therefore, a larger number is assigned to K_1.

According to experimental tests, a small fixed value is assigned to K_2.

By using the same algorithm, the pitch angle is estimated. The pitch angle in stationary conditions can be calculated with:

$$\boldsymbol{\theta_{v,s} = \frac{mH_{Pc}}{K_\theta}\, a_{x,m}} \tag{3-9}$$

This stationary pitch angle is used in the below observer to estimate the pitch angle of the vehicle body:

$$\boldsymbol{\dot{\hat{\theta}}_v = \dot{\hat{\theta}}_m + K'_1(\theta_{v,s,f} - \hat{\theta}_{v,f})} \tag{3-10}$$

$$\boldsymbol{\dot{\hat{z}}_2 = a\hat{z}_2 + b\hat{\theta}_v + K'_2\,(\theta_{v,s,f} - \hat{\theta}_{v,f})} \tag{3-11}$$

$$\boldsymbol{\hat{\theta}_{v,f}} = \boldsymbol{\hat{z}_2} \tag{3-12}$$

The stationary pitch angle is filtered with a low-pass filter (with gains a' and b') and is presented by $\theta_{v,s,f}$. The same low-pass filter is used to produce $\hat{\theta}_{v,f}$. $\hat{z}_2$ and $\hat{\theta}_v$ which are the states in the pitch angle observer. The error terms in (3-10) and (3-11) are the adjustment terms to correct the drift errors in the estimated pitch angle in the stationary state conditions.

K'_1 and K'_2 are observer gains. However, K'_1 is an adaptive gain and will change according to level of vehicle excitation in the longitudinal direction. This level of excitation is determined according to the value of the derivative of longitudinal acceleration. When this value is large, it means that the vehicle is accelerating fast or the driver is pushing down the brake pedal fast. When the value is small, it means that the vehicle is slowly accelerated or driver is pushing down the brake pedal smoothly. The rules below are used to set these gains:

- When the level of excitation in the longitudinal direction is large, a small number is assigned to K'_1. In this level of excitation, the correction term has to be small because of inaccuracy in the calculated stationary pitch angle with (3-9).
- When the level of excitation in the longitudinal direction is small, a larger number is assigned to K'_1. In this condition, the calculated stationary angle is accurate. Therefore, the correction term has more contribution.

It is observed from experiments that K'_2 can be set to a small fixed value. Estimated roll and pitch angles ($\hat{\phi}_v$ and $\hat{\theta}_v$) with two abovementioned observers (Equations (3-5)-(3-8), and Equations (3-9)-(3-12)) will be used in the developed algorithms in the next sections.

3.2 Tire force estimation algorithm

In this part, the algorithms applied to estimate longitudinal, lateral and vertical forces acting on each wheel are presented.

3.2.1 Longitudinal tire force estimation

For estimation of the longitudinal forces, an observer is developed using the wheel dynamics model proposed in [10]. Inputs to this observer are torques acting on each wheel and measured angular velocity of each wheel.

The wheel rotational dynamics equation is given by

$$\boldsymbol{I_{\omega,ij}\dot{\omega}_{ij} = T_{d,ij} - T_{b,ij} - R_e F_{x,ij}} \;, \quad \boldsymbol{i = f, r} \;, \quad \boldsymbol{j = l, r} \tag{3-13}$$

where T_d and T_b are driving and braking torques, respectively. The time derivative of the angular velocity is $\dot{\omega}$, R_e is the effective tire radius that lies between the tire's undeformed radius and static loaded radius [78]. The wheel moment of inertia around its spin axis is I_ω, and $F_{x,ij}$ is the longitudinal tire force (see Figure 3.2).

It is noted that driving and braking torques in (3-13) need to be calculated according to the vehicle's powertrain specifications and brake system. In this thesis, these torques are assumed available and are measured using the wheel load measurement system that will be discussed in Chapter 5.

It should be noted that since the dominant force in this estimation block is the longitudinal tire force, the effects of rolling resistance and wheel aerodynamic forces can be neglected.

The wheel dynamics, (3-13), can be presented in the Laplace space as

$$\boldsymbol{\frac{1}{Ts+1} I_\omega s\omega(s) = \frac{1}{Ts+1}[T_d(s) - T_b(s)] - \frac{1}{Ts+1} R_e F_x(s)} \tag{3-14}$$

where both sides are filtered by a low pass filter $1/(Ts + 1)$, and $T > 0$ is the related time constant.

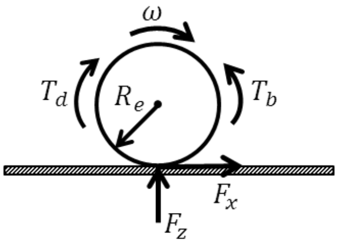

Figure 3.2. Simplified wheel dynamics model

The angular velocity is estimated by adding the following observer which has a similar structure to proportional-integral-derivative (PID) controller:

$$\frac{1}{Ts+1} I_\omega s\hat{\omega}(s) = \frac{1}{Ts+1}[T_d(s) - T_b(s)] - \frac{1}{Ts+1} R_e F_{x,0}(s) + \frac{1}{Ts+1}(K_p\tilde{\omega}(s) + K_i \frac{1}{s}\tilde{\omega}(s) + (I_\omega + K_d)\, s\tilde{\omega}(s)) \tag{3-15}$$

where K_p, K_i and K_d are the PID gains, $\hat{F}_x$ is the estimated tire longitudinal force, and

$$\tilde{\omega} = \omega_m - \hat{\omega} \tag{3-16}$$

where $\hat{\omega}$ is the estimated wheel angular velocity. It is worth noting that in **(3-13)** and **(3-16)** ω is the true angular velocity, and $\boldsymbol{\omega_m}$ is the measured angular velocity using the ABS sensor. In (3-15), driving and braking torques are used as inputs to estimate wheel's angular velocity. The following Lyapunov function is defined to prove the stability of the proposed observer and extract estimated longitudinal forces according to the stability analysis:

$$V = \frac{1}{2}\,\tilde{\omega}^2 \tag{3-17}$$

And, $\dot{V} = \dot{\tilde{\omega}}\,\tilde{\omega}$. Using (3-14), (3-15), and transferring $\dot{V}$ to Laplace domain

$$s\,V(s) = \frac{1}{I_w}(-R_e\tilde{F} - K_p\tilde{\omega} - K_i\frac{1}{s}\tilde{\omega} - (K_d + I_w)s\,\tilde{\omega})\tilde{\omega} \tag{3-18}$$

where $\tilde{F} = F_x - F_{x,0}$, and $V(0)$ and $\tilde{\omega}(0)$ are zero. With selecting

$$\tilde{\boldsymbol{F}} = \frac{-\boldsymbol{1}}{\boldsymbol{R_e}}\left(\boldsymbol{K_p^{\prime}}\,\tilde{\boldsymbol{\omega}} + \boldsymbol{K_i^{\prime}}\,\frac{\boldsymbol{1}}{\boldsymbol{s}}\,\tilde{\boldsymbol{\omega}} + \boldsymbol{K_d^{\prime}}\,\boldsymbol{s}\,\tilde{\boldsymbol{\omega}}\right) \tag{3-19}$$

and applying PID gains as: $0 < K_p' < K_p$, $K_i' = K_i$, $K_d' = (K_d + I_w)$, $\dot{V} \leq 0$ is guaranteed. Therefore, both $\tilde{\omega}$ and $\tilde{F}$ will converge to zero. Consequently, the estimated longitudinal force becomes:

$$\hat{\boldsymbol{F}}_{\boldsymbol{x}} = \boldsymbol{F_{x,0}} - \frac{\boldsymbol{1}}{\boldsymbol{R_e}}\left(\boldsymbol{K_p^{\prime}}\,\tilde{\boldsymbol{\omega}} + \boldsymbol{K_i^{\prime}}\,\frac{\boldsymbol{1}}{\boldsymbol{s}}\,\tilde{\boldsymbol{\omega}} + \boldsymbol{K_d^{\prime}}\,\boldsymbol{s}\,\tilde{\boldsymbol{\omega}}\right). \tag{3-20}$$

This observer requires an initial value for the longitudinal force ($F_{x,0}$). This initial value can be simply chosen as the initial drive torque divided by the effective tire radius.

3.2.2 Vertical tire force calculation

Typically, vertical tire forces are modeled without considering the effects of changes in the vehicle body roll and pitch angles and vertical motion of the vehicle body [10], [9], [8], [13]. To add these effects, vertical tire forces are calculated based on the acceleration of vehicle sprung mass in longitudinal, lateral and vertical directions, as well as rotation around roll and pitch axes.

Figure 3.3 depicts tire forces and acceleration components of the sprung mass in the vehicle pitch plane. In addition, m is the input that will be identified in Chapter 4. Vertical forces acting on the front and rear axles are given by:

$$\boldsymbol{F_{zf}} = -\boldsymbol{m}\frac{\boldsymbol{H_{COG}}}{\boldsymbol{L}}\big(\boldsymbol{a_{x,m}}\cos(\boldsymbol{\theta_v}) + \boldsymbol{a_{z,m}}\sin(\boldsymbol{\theta_v})\big) - \boldsymbol{m}\frac{\boldsymbol{L_r}}{\boldsymbol{L}}\big(\boldsymbol{a_{x,m}}\sin(\boldsymbol{\theta_v}) - \boldsymbol{a_{z,m}}\cos(\boldsymbol{\theta_v})\big) \tag{3-21}$$

$$\boldsymbol{F_{zr}} = \boldsymbol{m}\frac{\boldsymbol{H_{COG}}}{\boldsymbol{L}}\big(\boldsymbol{a_{x,m}}\cos(\boldsymbol{\theta_v}) + \boldsymbol{a_{z,m}}\sin(\boldsymbol{\theta_v})\big) - \boldsymbol{m}\frac{\boldsymbol{L_f}}{\boldsymbol{L}}\big(\boldsymbol{a_{x,m}}\sin(\boldsymbol{\theta_v}) - \boldsymbol{a_{z,m}}\cos(\boldsymbol{\theta_v})\big) \tag{3-22}$$

where $a_{z,m}$ is the measured vertical acceleration of COG, L_f is longitudinal distance between COG and front axle, and H_{COG} is the height of the centre of gravity.

Using these forces, the effective masses on the front and rear axles are defined as follows:

$$\boldsymbol{m_{v,f}} = \frac{\boldsymbol{F_{zf}}}{\boldsymbol{g}} \quad , \quad \boldsymbol{m_{v,r}} = \frac{\boldsymbol{F_{zr}}}{\boldsymbol{g}} \tag{3-23}$$

Figure 3.4 shows the sprung mass (rear view) in the roll plane and the forces which are acting on the sprung mass due to lateral motion of the vehicle. The roll plane model and equations in (3-23) can be used to compute the vertical tire force of each wheel, individually.

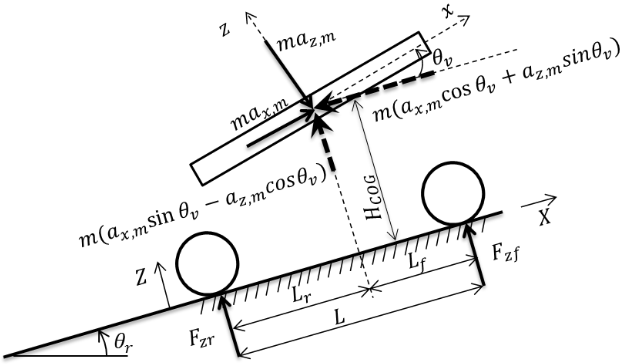

Figure 3.3. Pitch plane model (right side of the vehicle)

For instance, vertical force acting on rear-right tire can be calculated by taking moment around contact point of the rear left tire (see Figure 3.4) and using equations (3-21), (3-22) and (3-23) as follows:

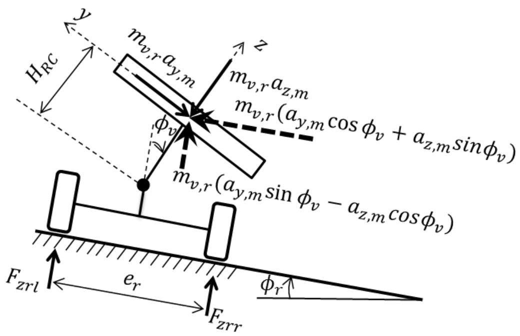

Figure 3.4. Roll plane model of rear axle (rear view of the vehicle)

$$\sum M_{rl} = 0 \rightarrow F_{zrr} = -\frac{m_{v,r}H_{COG}}{e_r}\Big(a_{y,m}\,cos(\phi_v) - a_{z,m}\,sin(\phi_v)\Big) - \frac{m_{v,r}}{e_r}\Big(a_{y,m}\,sin(\phi_v) + a_{z,m}\,cos(\phi_v)\Big)\left(\frac{e_r}{2} - H_{RC}\,sin(\phi_v)\right) \tag{3-24}$$

F_{zrl}, F_{zfr}, F_{zfl} are calculated in the same way.

$$F_{zrl} = \frac{m_{v,r}H_{COG}}{e_r}\Big(a_{y,m}\,cos(\phi_v) - a_{z,m}\,sin(\phi_v)\Big) - \frac{m_{v,r}}{e_r}\Big(a_{y,m}\,sin(\phi_v) + a_{z,m}\,cos(\phi_v)\Big)\left(\frac{e_r}{2} + H_{R_C}\,sin(\phi_v)\right) \tag{3-25}$$

$$F_{zfr} = -\frac{m_{v,f}H_{COG}}{e_f}\Big(a_{y,m}\,cos(\phi_v) - a_{z,m}\,sin(\phi_v)\Big) - \frac{m_{v,f}}{e_f}\Big(a_{y,m}\,sin(\phi_v) + a_{z,m}\,cos(\phi_v)\Big)\left(\frac{e_f}{2} - H_{RC}\,sin(\phi_v)\right) \tag{3-26}$$

$$F_{zfl} = \frac{m_{v,f}H_{COG}}{e_f}\Big(a_{y,m}\,cos(\phi_v) - a_{z,m}\,sin(\phi_v)\Big) - \frac{m_{v,f}}{e_f}\Big(a_{y,m}\,sin(\phi_v) + a_{z,m}\,cos(\phi_v)\Big)\left(\frac{e_f}{2} + H_{R_C}\,sin(\phi_v)\right) \tag{3-27}$$

where e_f and e_r are the front and rear track widths, respectively, and it is assumed that the height of front and rear roll centres are the same. The vertical tire forces for the wheels are F_{zfl}, F_{zfr}, F_{zrl} and F_{zrr}. The required variables for calculation of these forces are longitudinal, lateral, and vertical COG accelerations ($a_{x,m}$, $a_{y,m}$, $a_{z,m}$), as well as pitch (θ_v) and roll (ϕ_v) angles which are estimated using the algorithms introduced in the previous section. The accelerations are measured by an inertial measurement unit (6-axis IMU) which is connected to the vehicle body. It is important to note that $a_{x,m}$ and $a_{y,m}$ include the effects of gravity, vehicle body and road angles (road bank and road grade angles):

$$\boldsymbol{a_{y,m} = \dot{v}_y + \dot{\psi}\, v_x + g sin(\phi_v + \phi_r)} \tag{3-28}$$

$$\boldsymbol{a_{x,m} = \dot{v}_x - \dot{\psi}\, v_y + g sin(\theta_v + \theta_r)} \tag{3-29}$$

3.2.3 Lateral tire force estimation

The purpose of this module is to estimate the lateral tire force acting on each wheel. The estimated vertical and longitudinal tire forces, measured wheel steering angle, identified vehicle mass and estimated roll and pitch angles are the inputs. Yaw rate and longitudinal and lateral accelerations are the sensory data used in this estimation block. In this thesis, the parallel steering approximation is used to calculate the steering angle of wheels.

Because of observability issues highlighted in [7],[79], estimation of lateral force acting on each wheel is a challenging problem. To address this problem, lateral forces acting on front and rear axles are estimated first. Then, these estimated forces are distributed between left and right wheels proportional to their normal corresponding forces.

In a harsh maneuver however, where the wheels are slipping in the lateral direction, the estimated forces based on just vertical force distribution cannot exactly describe the actual changes in the lateral tire forces. Therefore, the equations governing the longitudinal and lateral forces and yaw moment are added to make this estimator more accurate in the extreme driving conditions and improve its robustness against wheel slippage. As a result, a handling model of the vehicle as shown in Figure 3.5 is used.

A random-walk model [31] that uses longitudinal and lateral acceleration and yaw moment signals is designed herein to handle the abovementioned conditions. The states for this estimator are defined as

$$\boldsymbol{x_1 = F_{yf} - \widehat{F}_{yf,temp} = \left(F_{yfl} + F_{yfr}\right) - (\widehat{F}_{yfl} + \widehat{F}_{yfr})} \tag{3-30}$$

$$x_2 = F_{yr} - \hat{F}_{yr,temp} = \left(F_{yrl} + F_{yrr}\right) - (\hat{F}_{yrl} + \hat{F}_{yrr}) \tag{3-31}$$

$$X = [x_1, x_2]^T \tag{3-32}$$

where F_{yfl}, F_{yfr}, F_{yrl} and F_{yrr} are the real force values (see Figure 3.5 (a)) while $\hat{F}_{yfl}$, $\hat{F}_{yfr}$, $\hat{F}_{yrl}$ and $\hat{F}_{yrr}$ are the estimated ones. F_{yf}, F_{yr} are the lateral forces acting on front and rear axles (see Figure 3.5 (b)), $\hat{F}_{y,f,temp}$, $\hat{F}_{y,r,temp}$ are the estimated forces obtained from

$$\hat{F}_{yf,temp} = \frac{\hat{F}_{zfl} + \hat{F}_{zfr}}{\hat{F}_{zfl} + \hat{F}_{zfr} + \hat{F}_{zrl} + \hat{F}_{zrr}} m\, a_{y,m} \tag{3-33}$$

$$\hat{F}_{yr,temp} = \frac{\hat{F}_{zrl} + \hat{F}_{zrr}}{\hat{F}_{zfl} + \hat{F}_{zfr} + \hat{F}_{zrl} + \hat{F}_{zrr}} m\, a_{y,m} \tag{3-34}$$

The new states do not have dynamics, and are treated as random signals

$$\dot{X}(t) = I_{2\times 2} w(t) \tag{3-35}$$

where $w(t)$ is the vector of process noise and I is an identity matrix. From the bicycle vehicle model (see Figure 3.5 (b)), longitudinal and lateral accelerations are related to the tire forces as:

$$a_{x,m} = \frac{1}{m}\left(F_{xf}\, cos(\delta) + F_{xr} - F_{yf}\, sin(\delta)\right) \tag{3-36}$$

$$a_{y,m} = \frac{1}{m}\left(F_{yr} + F_{yf}\, cos(\delta) + F_{xf}\, sin(\delta)\right) \tag{3-37}$$

$$\ddot{\psi} = \frac{1}{I_{zz}}\left(\left(F_{yf}\cos(\delta) + F_{xf}\sin(\delta)\right)L_f - F_{yr}\, L_r\right) \tag{3-38}$$

where the steering angle (δ) are the inputs, r is the yaw rate, I_{zz} is the moment of inertia about the z-axis, and F_{xf}, F_{xr} are

$$F_{xf} = F_{xfl} + F_{xfr} \tag{3-39}$$

$$F_{xr} = F_{xrl} + F_{xrr} \tag{3-40}$$

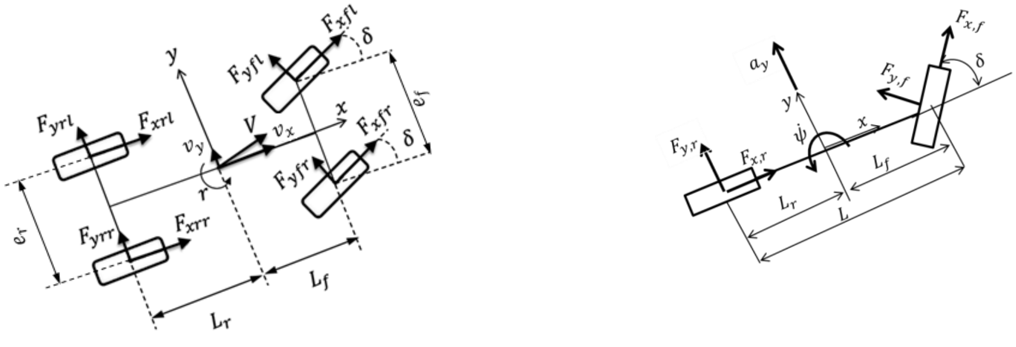

(a) (b)

Figure 3.5. Vehicle handling model (planar and bicycle vehicle models)

The measurement equation,y, can be represented in the state space form by using the newly defined states

$$\boldsymbol{y} = \begin{bmatrix} \boldsymbol{m a_{x,m} - \left(F_{xf}\, cos(\delta) + F_{xr} - \hat{F}_{yf,temp}\, sin(\delta)\right)} \\ \boldsymbol{m a_{y,m} - \left(F_{yf}\, cos(\delta) + \hat{F}_{yr,temp} + F_{xf}\, sin(\delta)\right)} \\ \boldsymbol{I_{zz}\ddot{\psi} - \left(\left(\hat{F}_{yf,temp}\, cos(\delta) + F_{xf}\, sin(\delta)\right) L_f - \hat{F}_{yr,temp}\, L_r\right)} \end{bmatrix} + \boldsymbol{v(t) = H(X,U) + v(t)} \tag{3-41}$$

where $v(t)$ is the measurement noise. It is assumed that good estimates of the longitudinal forces are available i.e. $F_{xij} = \hat{F}_{xij}$. Using this assumption and equations (3-30)-(3-32), (3-36)-(3-38) and (3-41), $H(X,U)$ can be written as

$$\boldsymbol{H(X,U)} = \begin{bmatrix} \boldsymbol{-x_1\, sin(\delta)} \\ \boldsymbol{x_1 cos(\delta) + x_2} \\ \boldsymbol{x_1\, cos(\delta)\, L_f - x_2 L_r} \end{bmatrix} \tag{3-42}$$

Therefore, the discrete forms of the state and measurement equations can be summarized as

$$\boldsymbol{X(k+1) = I_{2\times 2} X(k) + I_{2\times 2} w(k)} \tag{3-43}$$

$$\boldsymbol{y(k) = H(X(k), \delta(k)) + v(k)} \tag{3-44}$$

Equation (3-42) is the source of nonlinearity in the system. It can be assumed that δ is a time-varying parameter; therefore, equation (3-42) can be rearranged as

$$\boldsymbol{H}(\boldsymbol{X}) = \boldsymbol{C}\,\boldsymbol{X} = \begin{bmatrix} -\boldsymbol{sin}(\boldsymbol{\delta}) & \boldsymbol{0} \\ \boldsymbol{cos}(\boldsymbol{\delta}) & \boldsymbol{1} \\ \boldsymbol{L_f cos}(\boldsymbol{\delta}) & -\boldsymbol{L_r} \end{bmatrix} \begin{bmatrix} \boldsymbol{x_1} \\ \boldsymbol{x_2} \end{bmatrix} \tag{3-45}$$

According to equations (3-43) and (3-45), the observability matrix [16] is defined as

$$\boldsymbol{O} = [\boldsymbol{C}^{\boldsymbol{T}}\ \boldsymbol{A}^{\boldsymbol{T}}\boldsymbol{C}^{\boldsymbol{T}}] \tag{3-46}$$

where $A = I_{2\times2}$. According to observability criteria [80], the system in (3-43) and (3-44) is observable for all values of δ.

3.2.3.1 Nonlinear observer

The Extended Kalman filter (EKF) is a widely used state estimator in vehicle control applications [79], [31]. However, because the linearization of the system around the operating point and hence calculation of Jacobian matrices is required, the real-time implementation may not be computationally efficient [81], [82], [83]. Hence, the Unscented Kalman Filter (UKF) proposed in [82] can be a good alternative. It uses the unscented transformation technique [82] instead of the linearization and calculation of Jacobian matrices associated with the implementation of EKF.

Figure 3.6 shows the structure of the proposed estimator using the UKF algorithm for a discrete time nonlinear system. Equations (3-43)-(3-44) are applied to estimate lateral tire forces acting on each wheel.

This figure demonstrates the three steps involved in the UKF algorithm:

1- Sigma points calculation: these points are a minimal set of carefully chosen weighted sample points around each state.

2- States, covariance matrix and output prediction: in this step, information from the estimated states and the covariance matrix, in the time step $k-1$, and the calculated sigma points are used to predict the states, covariance matrix and outputs.

3- States and covariance matrix update: in this step, the new measurements are used to update the predicted states and covariance matrix in the previous step.

In this structure, $\bar{X}_{k|k-1}$ is the predicted state, $\bar{X}_k$ is the updated state, $\bar{X}_{k,1}$ is the first element of the vector $\bar{X}_k$, $\bar{X}_{k,2}$ is the second element of the vector $\bar{X}_k$. $P_{k|k-1}$ is the predicted error covariance matrix, P_k is the update error covariance matrix, and $\bar{Y}_{k|k-1}$ is the predicted output. For the sake of brevity, more details about the equations related to each of the above three steps can be found in Appendix I. The estimated states (i.e. $\bar{X}_k$) together with the initial rough estimates of the lateral forces ((3-33) and (3-34)) are used to estimate more accurate lateral forces acting on each axle ($\hat{F}_{yf}, \hat{F}_{yr}$). Finally, lateral forces acting on each wheel are calculated based on vertical force distribution on the right and left wheels as follows:

$$\hat{\boldsymbol{F}}_{yfl} = \frac{\hat{\boldsymbol{F}}_{zfl}}{\hat{\boldsymbol{F}}_{zfr} + \hat{\boldsymbol{F}}_{zfl}} \hat{\boldsymbol{F}}_{yf} \tag{3-47}$$

$$\hat{\boldsymbol{F}}_{yfr} = \frac{\hat{\boldsymbol{F}}_{zfr}}{\hat{\boldsymbol{F}}_{zfr} + \hat{\boldsymbol{F}}_{zfl}} \hat{\boldsymbol{F}}_{yf} \tag{3-48}$$

$$\hat{\boldsymbol{F}}_{yrl} = \frac{\hat{\boldsymbol{F}}_{zrl}}{\hat{\boldsymbol{F}}_{zrr} + \hat{\boldsymbol{F}}_{zrl}} \hat{\boldsymbol{F}}_{yr} \tag{3-49}$$

$$\hat{\boldsymbol{F}}_{yrr} = \frac{\hat{\boldsymbol{F}}_{zrr}}{\hat{\boldsymbol{F}}_{zrr} + \hat{\boldsymbol{F}}_{zrl}} \hat{\boldsymbol{F}}_{yr} \tag{3-50}$$

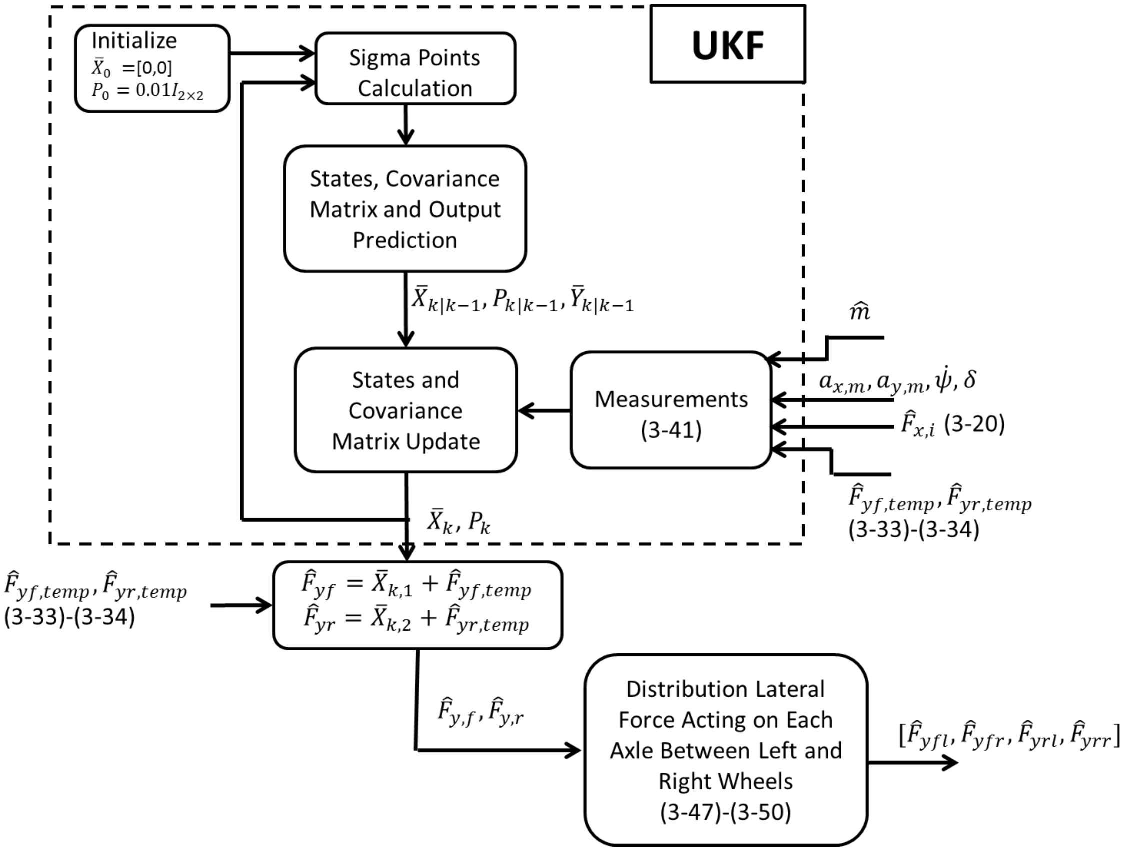

Figure 3.6. Proposed lateral tire force estimation structure

3.3 Vehicle velocity estimation algorithm

The developed structure of the vehicle lateral and longitudinal velocities' estimation is shown in Figure 3.7. Due to the coupling between longitudinal and lateral kinematic equations, a parallel structure is proposed to estimate longitudinal and lateral velocities of the vehicle, simultaneously.

Longitudinal and lateral acceleration signals, yaw rate, wheels' speeds and steering wheel angle are the required measurements for this algorithm. Additionally, the lateral velocity estimator (Block B2) needs the lateral and vertical forces acting on each tire provided by the estimation algorithms in Section 3.2, the roll angle and road bank angle provided by the proposed estimation algorithms in Section 3.1 and Chapter 4. Furthermore, Block B1 and B2 are communicating together by sharing their outputs at the previous time step. In the next sections, these blocks are explained in detail.

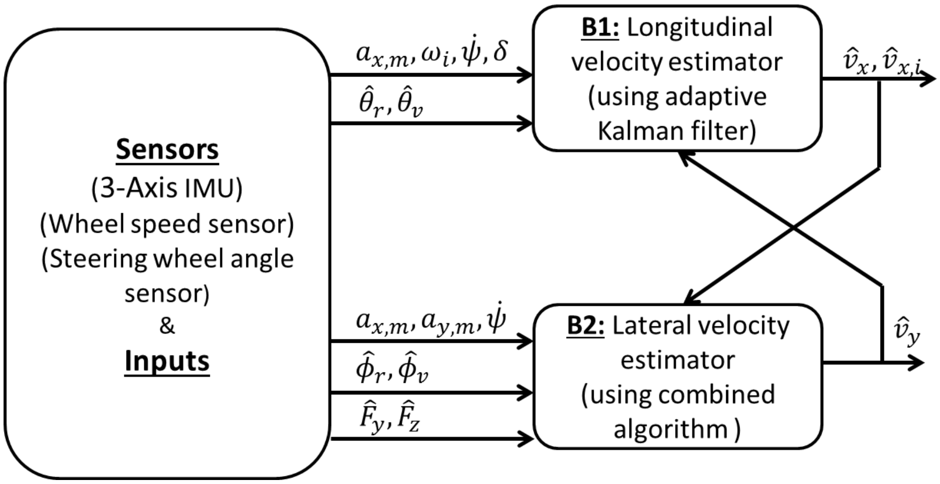

Figure 3.7. Overall structure of vehicle velocity estimation

3.3.1 Longitudinal velocity estimator (Block B1)

To estimate longitudinal velocity of vehicle at the centre of gravity, the vehicle motion in longitudinal direction is used that is defined as:

$$\dot{v}_x = a_{x,m} + \dot{\psi} v_y + g \sin(\theta_v + \theta_r) + b_1 + \epsilon_1 \tag{3-51}$$

$$\dot{b}_1 = 0 \tag{3-52}$$

where b_1 represents the bias in the sensory data, v_x and v_y are the vehicle longitudinal and lateral velocities, respectively. ϵ_1 represents the noise added to the measured signals. Equation (3-52) assumes that bias term does not have fast dynamics and hence its change in time is zero. The proposed algorithm depicted in Figure 3.8 is designed to estimate the longitudinal velocity.

The velocity of each individual wheel, longitudinal acceleration, yaw rate, wheel steering angle, estimated lateral velocity from previous step, estimated pitch angle (see Section 3.1) and identified road grade (see Chapter 4) are the required signals for this algorithm. The output of this structure is longitudinal velocity ($\hat{v}_{x,k}$) and estimated velocity at each corner, which are used in the lateral velocity estimation algorithm ($\hat{v}_{x,i,k}$). Each of the blocks shown in Figure 3.8 is discussed shortly.

The Kalman Filter (KF) is the observer used in this structure. A KF has two steps, which are prediction and correction. In the prediction step, vehicle longitudinal velocity and the bias are predicted, and then new measurements are used to correct the predicted states. The kinematic model ((3-51)-(3-52)) is used to predict the longitudinal velocity of the vehicle in KF. The predicted states are calculated by using:

$$\begin{bmatrix} \boldsymbol{\hat{v}_{x,k|k-1}} \\ \boldsymbol{\hat{b}\ _{k|k-1}} \end{bmatrix} = \begin{bmatrix} \mathbf{1} & \mathbf{1} \\ \mathbf{0} & \mathbf{1} \end{bmatrix} \begin{bmatrix} \boldsymbol{\hat{v}_{x,k-1}} \\ \boldsymbol{\hat{b}\ _{k-1}} \end{bmatrix} + \begin{bmatrix} \boldsymbol{\left(a_{x,m} + \dot{\psi}\hat{v}_{y,k-1} + g\ \mathbf{sin}(\hat{\theta}_v + \hat{\theta}_r)\right)\Delta T} \\ \mathbf{0} \end{bmatrix} \tag{3-53}$$

where $\hat{v}_{x,k|k-1}$ and $\hat{b}\ _{k|k-1}$ are the predicted states, $\hat{v}_{x,k-1}$ and $\hat{b}\ _{k-1}$ are the estimated states in the previous time step, $\hat{v}_{y,k-1}$ is the estimated lateral velocity in the previous time step and ΔT is the sample time.

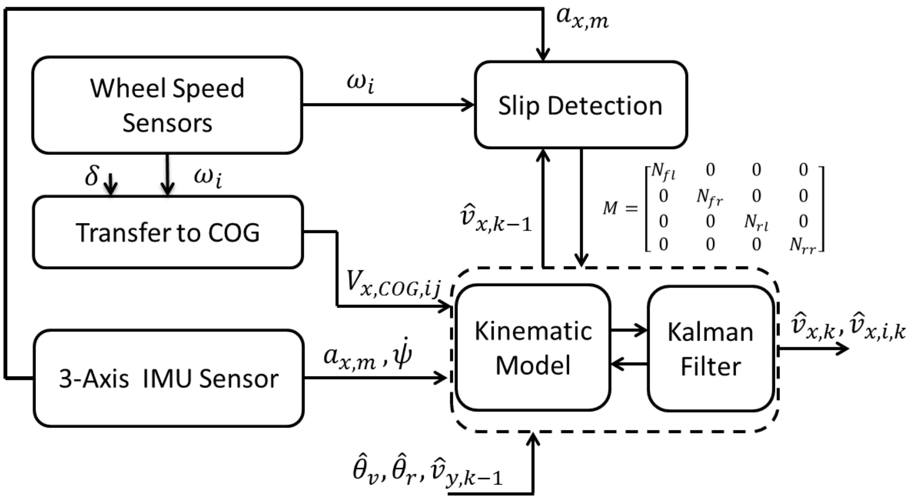

Figure 3.8. Estimation structure of reference longitudinal velocity

The wheels speeds are used to provide the measurement signals in the KF to update the predicted vehicle longitudinal velocity and the bias. Velocities at the centre of each of the four wheels are calculated and then transferred to vehicle COG. The “Transfer to COG” block in Figure 3.8 is used to calculate these velocities as follows:

$$\boldsymbol{V_{x,COG,fl} = R_{e,fl}\omega_{fl}\cos(\delta) - \dot{\psi}\frac{e_f}{2}} \tag{3-54}$$

$$\boldsymbol{V_{x,COG,fr} = R_{e,fr}\omega_{fr}\cos(\delta) + \dot{\psi}\frac{e_f}{2}} \tag{3-55}$$

$$\boldsymbol{V_{x,COG,rl} = R_{e,rl}\omega_{rl} - \dot{\psi}\frac{e_r}{2}} \tag{3-56}$$

$$\boldsymbol{V_{x,COG,rr} = R_{e,rr}\omega_{rr} + \dot{\psi}\frac{e_r}{2}} \tag{3-57}$$

where $R_{e,fl}$, $R_{e,fr}$, $R_{e,rl}$, $R_{e,rr}$, ω_{fl}, ω_{fr}, ω_{rl}, ω_{rr} are the effective radiuses and wheels’ speeds of front-left, front-right, rear left and rear right wheels, respectively. The front and rear track-width of vehicle are e_f and e_r. Therefore, the measurement matrix used in the KF is defined as:

$$\boldsymbol{Y_k} = \left[\boldsymbol{V_{x,COG,fl}}; \boldsymbol{V_{x,COG,fr}}; \boldsymbol{V_{x,COG,rl}}; \boldsymbol{V_{x,COG,rr}}\right] \tag{3-58}$$

However, these calculated velocities at the COG do not take into account the large slip that may happen during braking or traction for each wheel. For instance, the experimental data in Figure 3.9 is used to elaborate on the above fact. Figure 3.9 shows that the angular velocities of the four wheels before time 8 s have approximately the same values. However, between 8 s and 12 s, they have not. Most notably, angular velocity of the front left wheel during 10.43 s to 11.22 s is visibly increasing. Therefore, using information of such a wheel to estimate vehicle velocities within such time window can introduce large errors in the process.

The "Slip Detection" block, shown in Figure 3.8, is used to address the above-mentioned problem. This block determines which wheels are slipping. The output of this block is a diagonal matrix, *N*, which is 4-by-4 matrix:

$$\boldsymbol{N} = \begin{bmatrix} \boldsymbol{N_{fl}} & \mathbf{0} & \mathbf{0} & \mathbf{0} \\ \mathbf{0} & \boldsymbol{N_{fr}} & \mathbf{0} & \mathbf{0} \\ \mathbf{0} & \mathbf{0} & \boldsymbol{N_{rl}} & \mathbf{0} \\ \mathbf{0} & \mathbf{0} & \mathbf{0} & \boldsymbol{N_{rr}} \end{bmatrix} \tag{3-59}$$

This matrix is used by the KF to update the predicted states according to new measurements using:

$$\begin{bmatrix} \boldsymbol{\hat{v}_{x,k}} \\ \boldsymbol{\hat{b}}_{\ \boldsymbol{k}} \end{bmatrix} = \begin{bmatrix} \boldsymbol{\hat{v}_{x,k|k-1}} \\ \boldsymbol{\hat{b}}_{\ \boldsymbol{k|k-1}} \end{bmatrix} + \boldsymbol{K_k N}\left(\boldsymbol{Y_k} - \begin{bmatrix} \mathbf{1} & \mathbf{0} \\ \mathbf{1} & \mathbf{0} \\ \mathbf{1} & \mathbf{0} \\ \mathbf{1} & \mathbf{0} \end{bmatrix} \begin{bmatrix} \boldsymbol{\hat{v}_{x,k|k-1}} \\ \boldsymbol{\hat{b}}_{\ \boldsymbol{k|k-1}} \end{bmatrix} \right) \tag{3-60}$$

where K_k is the Kalman gain, $\hat{v}_{x,k}$ and $\hat{b}_k$ are the estimated states at the current time. For the sake of brevity, readers are referred to Appendix II for more details on the Kalman filter algorithm.

Each diagonal entry of N is zero or one indicating if slip happens (1) or does not happen (0). To determine these diagonal entries, the "Slip Detection" block uses rules that are functions of current wheel speed (ω_k), moving average of a set of wheel speed data including current time and n previous wheel speed data (ω_a), vehicle longitudinal acceleration ($a_{x,m}$) and estimated vehicle speed in previous step ($\hat{v}_{x,k1}$). Here, the rules used in this block are discussed:

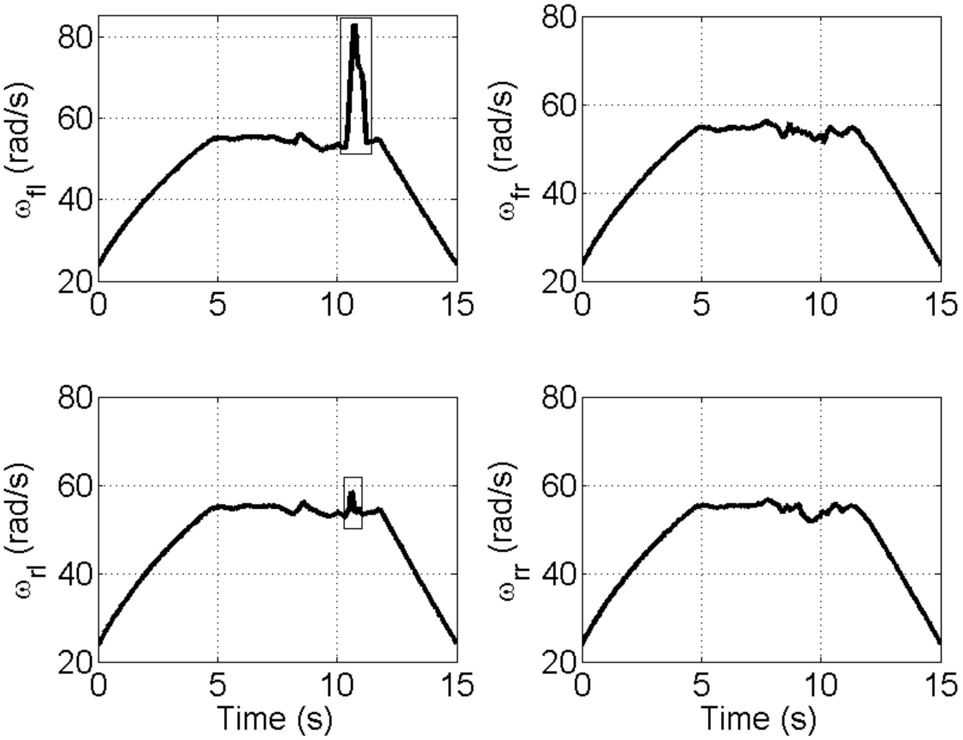

Figure 3.9. Experiment data of wheel angular velocities of electric vehicle. Slippages in front-left and rear-left wheels highlighted.

Rule 1: When the vehicle is accelerating ($a_{x,m} > 0$) the probability of slippage at the wheels on an axle with higher speed is more than wheels on the axle with lower speed. In addition, when the driver is pushing down the brake pedal ($a_{x,m} < 0$), wheels on the axle with the lower speed has higher likelihood of slippage.

Then, during acceleration, if $(\omega_{fl} + \omega_{fr}) \geq (\omega_{rl} + \omega_{rr})$ then $N_{fl} = N_{fr} = 0$, or during braking, if $(\omega_{fl} + \omega_{fr}) \leq (\omega_{rl} + \omega_{rr})$ then $N_{fl} = N_{fr} = 0$.

Rule 2: When a big slippage happens there is a fast and sharp change in the wheel angular velocity at the beginning of slippage. Monitoring the difference between moving average of the wheel angular velocity and current wheel angular velocity, these fast changes can be detected.

Then, during acceleration, if $\left|\omega_{fl} - \omega_{fl,a}\right| > \alpha_1$ then $N_{fl} = 0$. $\omega_{fl,a} = \frac{\sum_{i=1}^{M} \omega_{fl,i}}{M}$ and α_1 is a predefined boundary. Although, the same rule is used during braking, the parameter, α_1, has different value during braking which is α_1'. Parameters α_1, α_1' and the period selected for the moving average of each wheel angular velocity are tuned according to test data. The same rules are used for other wheels.

Rule 3: Calculated vehicle longitudinal velocity using each individual wheel speed (Equations **(3-54)-(3-57)**) can be compared with the estimated vehicle longitudinal velocity in the previous time step to detect slippage in each wheel. A big slippage in a wheel usually starts with a fast change. However, the big slippage may continue without any further fast changes. This rule is used to detect the slippage in this situation.

Then, during acceleration, if $\left|V_{x,COG,fl} - \hat{v}_{x,k1}\right| > \alpha_2$ then $N_{fl} = 0$. $V_{x,COG,fl}$ is calculated by (**3-54**), and $\hat{v}_{x,k1}$ is the estimated velocity in the previous time instant. And, during braking, if $\left|\hat{v}_{x,k1} - V_{x,COG,fl}\right| > \alpha_2^{'}$ then $N_{fl} = 0$. α_2 and α_2' are predefined boundaries with different values. And, their values are tuned according to experiment test data. The same rules are applied for other wheels.

Rule 4: This rule focuses on the direction of changes in the wheel angular velocity to select the proper wheel speed measurement for the KF. When the vehicle is accelerating and the wheel speed is decreasing, the information received from this wheel is not used in the KF. For example, we can assume that the vehicle is accelerating and a big slippage happens in a wheel. If the slipping wheel wants to return to its normal condition, then its angular velocity will be decreased. During this window of time that the wheel is slipping and its angular velocity is decreasing, its angular velocity will not be used in the velocity estimation algorithm. And, when the vehicle is braking and the wheel speed is increasing, the speed of that wheel is not used in the measurement model of KF.

For instance, during acceleration, if $\mathrm{sign}\left(\omega_{fl} - \omega_{fl,a}\right) = -1$ then $N_{fl} = 0$, and during braking, if $\mathrm{sign}\left(\omega_{fl} - \omega_{fl,a}\right) = 1$ then $N_{fl} = 0$. The same rules are applied for other three wheels.

All of these four rules are checked for each wheel, and the information received by the wheels which satisfy all rules is used in KF. If all the diagonal entries in (3-59) become zero, then the algorithm will be a simple integration of $\dot{v}_x$ in (3-51) to calculate the vehicle longitudinal velocity.

3.3.2 Lateral velocity estimator (Block B2)

Changes in the lateral velocity of the vehicle is presented by the following kinematic equation of the lateral motion

$$\dot{\boldsymbol{v}}_{y,kinematic} = \boldsymbol{a}_{y,m} - \dot{\boldsymbol{\psi}}\, \boldsymbol{v}_x - \boldsymbol{g}\, \boldsymbol{sin}(\boldsymbol{\phi}_v + \boldsymbol{\phi}_r) + \boldsymbol{b}_2 + \boldsymbol{\epsilon}_2 \tag{3-61}$$

where b_2 is the bias and ϵ_2 is sensor noise. The bias term will create a drift in long term in lateral velocity calculation if equation (3-61) is integrated to calculate the lateral velocity.

The effect of noise in ϵ_2 can be attenuated by filtering the sensory data $(a_{y,m}, \dot{\psi})$. To deal with this bias term, the lateral velocity will be estimated with combination of two different sources of information.

To estimate the lateral velocity, two sources of information will be used: one source is lateral velocity information from the kinematic equation (3-61). The second source is the inverse tire model. Figure 3.10 shows the overall structure of this estimator. Lateral velocity is estimated by designing a combined algorithm that uses both sources, simultaneously. The top path in Figure 3.10 is using an inverse tire model to estimate the lateral velocity of each wheel; then these lateral velocities will be transferred to COG and their derivatives are calculated. The bottom path is working according to the kinematic approach to calculate the changes in the vehicle lateral velocity. The two abovementioned sources are weighted and combined together in the last block (see Figure 3.10) by using following equation

$$\dot{\hat{\boldsymbol{v}}}_y = \boldsymbol{\alpha}\, \dot{\hat{\boldsymbol{v}}}_{y,tire\to COG} + (\boldsymbol{1} - \boldsymbol{\alpha})\, \dot{\hat{\boldsymbol{v}}}_{y,kinematic} \tag{3-62}$$

where the domain of $\alpha \in [0,1]$. When the vehicle is moving in a straight line, the proposed estimator puts more weight on the velocity information from the tire model ($\dot{\hat{v}}_{y,tire\rightarrow COG}$). However, when the vehicle is excited in the lateral direction, the kinematic equation ($\dot{\hat{v}}_{y,kinematic}$) has more contribution in the estimation of the vehicle lateral velocity. This decision is made according to the yaw rate and its change with respect to time. When the yaw rate and its change are close to zero, it means that the vehicle is not doing a maneuver in the lateral direction. But, when the yaw rate is large or the change in yaw rate is large it means that the vehicle is excited in the lateral direction. Finally, by integration of $\dot{\hat{v}}_y$ in (3-62), the lateral velocity is estimated. Calculation of both $\dot{\hat{v}}_{y,kinematic}$ and $\dot{\hat{v}}_{y,tire\rightarrow CG}$ are explained in more details in the following paragraphs.

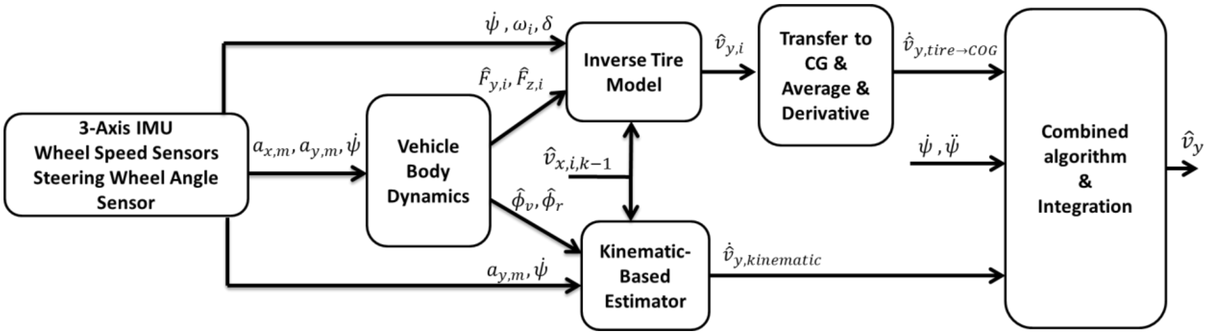

Figure 3.10. Estimation structure used to estimate reference lateral velocity.

According to Figure 3.10, $\dot{\hat{v}}_{y,kinematic}$ is a combination of sensory signals ($a_{y,m}, \dot{\psi}$), and estimated signals ($\hat{v}_{x,i}, \hat{\phi}_v, \hat{\phi}_r$). Additionally, $\hat{v}_{x,i}$ is the output of the algorithm proposed in Section 3.3.1.

Based on the proposed structure in Figure 3.10, the input of the inverse tire model is the calculated lateral and vertical forces (from Section 3.2) and sensory signals. The output is the estimation of the vehicle lateral velocity. The tire model used in this structure is a 1-D Lugre tire model [85]-[86]. This model is dynamic and is accurate even when the tire is in the nonlinear region [86]. This tire model is represented by:

$$\dot{z} = v_r - \frac{\sigma_0 |v_r|}{\vartheta g(v_r)} z - K\left|R_{e,ij}\omega\right| z, \qquad i = f,\, r, \quad j = l,\, r \tag{3-63}$$

$$\mu = \frac{F_y}{F_z} = \sigma_0 z + \sigma_1 \dot{z} + \sigma_2 v_r, \tag{3-64}$$

$$g(v_r) = \mu_C + (\mu_S - \mu_C) e^{-|v_r/v_s|^{1/2}} \tag{3-65}$$

where σ_0, $\sigma_1$and σ_2 are the stiffness coefficient, damping coefficient and the relative viscous damping coefficient, respectively. Because the contribution of v_r in (3-64) is small [86], it is assumed that $\sigma_2 = 0$. The internal friction state is z, v_s is the Stribeck relative velocity and K is a parameter to capture the steady state friction/slip characteristic. The normalized coulomb and static friction are μ_C and μ_S, respectively. The level of tire/road adhesion that changes according to road surface (icy, wet, dry,…) is ϑ. The relative velocity is v_r, and is defined as follows for front wheels

$$v_r = -v_x \sin\delta + v_y \cos\delta \tag{3-66}$$

Because the vehicles used in this thesis are front-wheel-steering vehicles, δ is zero in the rear wheels. By using the tire parameters and the estimated lateral and vertical forces, equation (3-64) can be evaluated. Consequently, z and $\dot{z}$ are known. Hence, equation (3-63) can be rearranged as

$$\dot{z} + K|R_e\omega| z = v_r - \frac{\sigma_0 |v_r|}{\vartheta g(v_r)} z \tag{3-67}$$

v_r and $-\frac{\sigma_0|v_r|}{\vartheta g(v_r)}$ are varying parameters. Hence, equation (3-67) can be represented in the following format:

$$\boldsymbol{y} = \boldsymbol{\phi}^{\boldsymbol{T}}\boldsymbol{\Psi}\,, \qquad \boldsymbol{\Psi}^{\boldsymbol{T}} = [\boldsymbol{\Psi}_{\boldsymbol{1}}\ \boldsymbol{\Psi}_{\boldsymbol{2}}], \qquad \boldsymbol{\phi}^{\boldsymbol{T}} = [\boldsymbol{\phi}_{\boldsymbol{1}}\ \boldsymbol{\phi}_{\boldsymbol{2}}] \tag{3-68}$$

where

$$\boldsymbol{y} = \dot{\boldsymbol{z}} + \boldsymbol{K}|\boldsymbol{R}_{\boldsymbol{e}}\boldsymbol{\omega}|\boldsymbol{z} \tag{3-69}$$

$$\boldsymbol{\Psi}^{\boldsymbol{T}} = [\boldsymbol{v}_{\boldsymbol{r}}\ \ -\frac{\boldsymbol{\sigma}_{\boldsymbol{0}}|\boldsymbol{v}_{\boldsymbol{r}}|}{\boldsymbol{\vartheta g}(\boldsymbol{v}_{\boldsymbol{r}})}], \tag{3-70}$$

$$\boldsymbol{\phi}^{\boldsymbol{T}} = [\boldsymbol{1}\ \boldsymbol{z}], \tag{3-71}$$

where Ψ is the vector of unknown parameters that can be identified using the measured signals, known variables, and a parameter identification method. In this thesis, recursive least square (RLS) method is adopted as the parameter identification algorithm. RLS utilizes the following cost function:

$$\boldsymbol{J}(\boldsymbol{w}) = \sum_{\boldsymbol{k}=\boldsymbol{1}}^{\boldsymbol{N}} \left[\boldsymbol{y}(\boldsymbol{k}) - \boldsymbol{\phi}^{\boldsymbol{T}}(\boldsymbol{k})\widehat{\boldsymbol{\theta}}(\boldsymbol{k})\right]^{\boldsymbol{2}} \tag{3-72}$$

According to this cost function, the following update equations can be derived to identify the system parameters:

$$\widehat{\boldsymbol{\theta}}(\boldsymbol{k}) = \widehat{\boldsymbol{\theta}}(\boldsymbol{k}-\boldsymbol{1}) + \frac{\boldsymbol{P}(\boldsymbol{k}-\boldsymbol{1})\boldsymbol{\phi}(\boldsymbol{k})\boldsymbol{e}(\boldsymbol{k})}{\boldsymbol{\lambda} + \boldsymbol{\phi}^{\boldsymbol{T}}(\boldsymbol{k})\boldsymbol{P}(\boldsymbol{k}-\boldsymbol{1})\boldsymbol{\phi}(\boldsymbol{k})} \tag{3-73}$$

$$\boldsymbol{P}(\boldsymbol{k}) = \frac{\boldsymbol{1}}{\boldsymbol{\lambda}}\boldsymbol{P}(\boldsymbol{k}-\boldsymbol{1}) - \frac{\boldsymbol{P}(\boldsymbol{k}-\boldsymbol{1})\boldsymbol{\phi}(\boldsymbol{k})\boldsymbol{\phi}^{\boldsymbol{T}}(\boldsymbol{k})\boldsymbol{P}(\boldsymbol{k}-\boldsymbol{1})}{\boldsymbol{\lambda}(\boldsymbol{\lambda} + \boldsymbol{\phi}^{\boldsymbol{T}}(\boldsymbol{k})\boldsymbol{P}(\boldsymbol{k}-\boldsymbol{1})\boldsymbol{\phi}(\boldsymbol{k}))} \tag{3-74}$$

where e is the output error ($e = y - \phi^T\hat{\theta}$). P is the covariance matrix and it is a diagonal matrix ($P(0) = \rho I_{2\times 2}$ and ρ is 0.001). λ is the forgetting factor.

Using the estimated longitudinal velocity at the centre of each wheel at the previous time step, v_r which is the output of RLS algorithm, and (3-66) the lateral velocity at the centre of each wheel is calculated. Using the lateral velocity of each wheel, the lateral velocity of COG is calculated as:

$$\boldsymbol{v_{y,COG,i} = v_{y,tire,i} - \dot{\psi} L_f,} \qquad \boldsymbol{i = fl, fr} \qquad \text{(Front tires)} \tag{3-75}$$

$$\boldsymbol{v_{y,COG,j} = v_{y,tire,j} + \dot{\psi}\, L_r,} \qquad \boldsymbol{j = rl, rr} \qquad \text{(Rear tires)} \tag{3-76}$$

The average of the lateral velocities in equations (3-75)-(3-76) is the estimated lateral velocity of the COG based on the inverse tire model. Using the derivative of this estimated lateral velocity, the kinematic model (see (3-61)), and equation (3-62), the lateral velocity can be calculated.

3.4 Summary

In this chapter, a structure was proposed to estimate vehicle body's roll and pitch angles and forces acting on each wheel individually. In addition, an estimation algorithm was proposed to estimate the vehicle longitudinal and lateral velocities. The proposed roll and pitch angle estimation algorithms estimated vehicle body angles during low and high excitations. The proposed tire forces estimation algorithms estimated forces acting on each tire in three directions without using tire model. The proposed velocity estimation algorithms estimated the vehicle longitudinal and lateral velocities concurrently.

In the next chapter, road bank angle and road grade identification algorithms used by the proposed velocity estimation structure will be presented. In addition, the sensitivity of tire forces and the proposed velocity estimation algorithms to changes in vehicle and tire parameters will be investigated. According to this investigation, parameters which have significant effect on the vehicle state estimation algorithm will be selected to develop identification algorithms for them.

Chapter 4

Vehicle parameters and road angles identification algorithms

The sensors used in vehicles such as inertial measurment unit (IMU) sensor, accelerometers or gyros are attached to the vehicle body. Changes in road angles or vehicle body angles impact the outputs of these sensors. In addition, road bank and grade angles have influences on the lateral and longitudinal velocity estimation algorithms proposed in Chapter 3. Two identification algorithms which are kinematic-based methods are proposed to identify bank and grade angles. The distinction between the effect of the vehicle body angles and the road angles is investigated through the analysis of the kinematic relations between the coordinate systems that is discussed in this chapter.

Additionally, the sensitivity of the developed estimation algorithms in the previous chapter to vehicle inertial and tire parameters is investigated to identify parameters that have significant effects on the performance of estimation algorithms.

4.1 Road bank angle and road grade

In this section, kinematic relations between angular velocities of the vehicle are defined. This information is then used to develop the proposed observer for identification of road bank angle and road grade.

4.1.1 Vehicle coordinate systems

Vehicle states can be described in different coordinate systems. Selection of the proper coordinate system is very important because the vehicle states can have different values in each of these coordinate systems. Figure 4.1 shows the main coordinate systems commonly used in the representation and analysis of vehicle system dynamics.

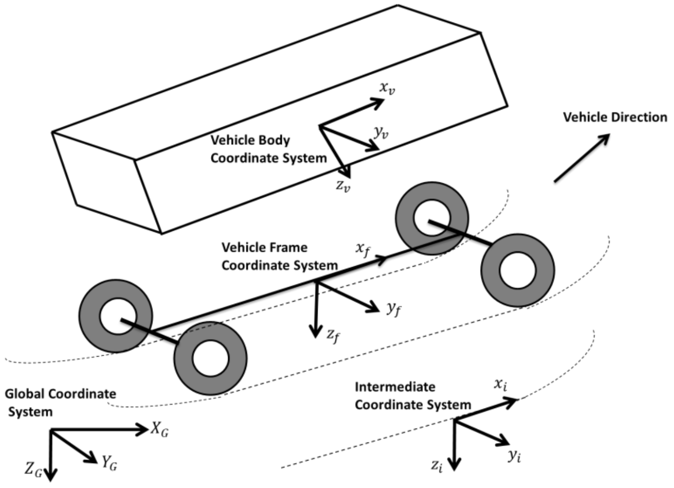

Figure 4.1. Coordinate systems

The body coordinate system is attached to the vehicle body. The frame coordinate system is attached to the unsprung mass of the vehicle. The direction of *z*-axis of the intermediate coordinate system is the same as the global coordinate system. The intermediate coordinate system is rotating around the *z*-axis with the same yaw rate as the vehicle. In the next section, the kinematic relations between angular velocities in these coordinate systems are investigated to calculate the rates of changes in the road bank and grade angles.

4.1.2 Kinematic relations between vehicle body, frame and road angular rates

Roll rate ($\dot{\phi}_f$), pitch rate ($\dot{\theta}_f$) and yaw rate ($\dot{\psi}_f$) of the vehicle frame cannot be measured. However, these rates can be defined as a function of vehicle body angluar rates ($\dot{\phi}_v, \dot{\theta}_v, \dot{\psi}_v$) and measured rates ($\dot{\phi}_m, \dot{\theta}_m, \dot{\psi}_m$) by the 6-axis IMU sensor. The rotation matrix from the vehicle frame coordinate to the vehicle body coordinate is given by:

$$\boldsymbol{Q_{f\rightarrow v} = R_{\theta_v} R_{\phi_v}} \tag{4-1}$$

when R_{θ_v} and R_{ϕ_v} are rotation matrixes around y_f and x_f, respectively , and can be written as:

$$\boldsymbol{R_{\phi_v}} = \begin{bmatrix} \boldsymbol{1} & \boldsymbol{0} & \boldsymbol{0} \\ \boldsymbol{0} & \boldsymbol{cos(\phi_v)} & \boldsymbol{sin(\phi_v)} \\ \boldsymbol{0} & \boldsymbol{-sin(\phi_v)} & \boldsymbol{cos(\phi_v)} \end{bmatrix} \tag{4-2}$$

$$\boldsymbol{R_{\theta_v}} = \begin{bmatrix} \boldsymbol{cos(\theta_v)} & \boldsymbol{0} & \boldsymbol{-sin(\theta_v)} \\ \boldsymbol{0} & \boldsymbol{1} & \boldsymbol{0} \\ \boldsymbol{sin(\theta_v)} & \boldsymbol{0} & \boldsymbol{cos(\theta_v)} \end{bmatrix} \tag{4-3}$$

Using the above transformations, the relation between measured rates and frame rates is given by the following equation:

$$\begin{bmatrix} \dot{\boldsymbol{\phi}}_{\boldsymbol{m}} \\ \dot{\boldsymbol{\theta}}_{\boldsymbol{m}} \\ \dot{\boldsymbol{\psi}}_{\boldsymbol{m}} \end{bmatrix} = \begin{bmatrix} \dot{\boldsymbol{\phi}}_{\boldsymbol{v}} \\ \dot{\boldsymbol{\theta}}_{\boldsymbol{v}} \\ \dot{\boldsymbol{\psi}}_{\boldsymbol{v}} \end{bmatrix} + \boldsymbol{Q_{f\rightarrow b}} \begin{bmatrix} \dot{\boldsymbol{\phi}}_{\boldsymbol{f}} \\ \dot{\boldsymbol{\theta}}_{\boldsymbol{f}} \\ \dot{\boldsymbol{\psi}}_{\boldsymbol{f}} \end{bmatrix} \tag{4-4}$$

The equation can be reorganized as:

$$\begin{bmatrix} \dot{\boldsymbol{\phi}}_{\boldsymbol{f}} \\ \dot{\boldsymbol{\theta}}_{\boldsymbol{f}} \\ \dot{\boldsymbol{\psi}}_{\boldsymbol{f}} \end{bmatrix} = \left(\boldsymbol{Q_{f\rightarrow v}}\right)^{\boldsymbol{-1}} \left(\begin{bmatrix} \dot{\boldsymbol{\phi}}_{\boldsymbol{m}} \\ \dot{\boldsymbol{\theta}}_{\boldsymbol{m}} \\ \dot{\boldsymbol{\psi}}_{\boldsymbol{m}} \end{bmatrix} - \begin{bmatrix} \dot{\boldsymbol{\phi}}_{\boldsymbol{v}} \\ \dot{\boldsymbol{\theta}}_{\boldsymbol{v}} \\ \dot{\boldsymbol{\psi}}_{\boldsymbol{v}} \end{bmatrix} \right) \tag{4-5}$$

Additionally, the kinematic relation between the vehicle frame coordinate and the global coordinate is defined. By using the rotation angles of the vehicle frame, the transformation matrix from the vehicle frame coordinate to the global coordinate or vice versa can be calculated as:

$$\begin{bmatrix} \dot{\boldsymbol{\phi}}_{\boldsymbol{f}} \\ \dot{\boldsymbol{\theta}}_{\boldsymbol{f}} \\ \dot{\boldsymbol{\psi}}_{\boldsymbol{f}} \end{bmatrix} = \boldsymbol{R_{\phi_v}} \begin{bmatrix} \dot{\boldsymbol{\phi}} \\ \boldsymbol{0} \\ \boldsymbol{0} \end{bmatrix} + \boldsymbol{R_{\phi}}\ \boldsymbol{R_{\theta}} \begin{bmatrix} \boldsymbol{0} \\ \dot{\boldsymbol{\theta}} \\ \boldsymbol{0} \end{bmatrix} + \boldsymbol{R_{\phi}}\ \boldsymbol{R_{\theta}}\ \boldsymbol{R_{\psi}} \begin{bmatrix} \boldsymbol{0} \\ \boldsymbol{0} \\ \dot{\boldsymbol{\psi}} \end{bmatrix} = \boldsymbol{Q_{G\rightarrow f}} \begin{bmatrix} \dot{\boldsymbol{\phi}} \\ \dot{\boldsymbol{\theta}} \\ \dot{\boldsymbol{\psi}} \end{bmatrix} \tag{4-6}$$

where

$$R_{\psi} = \begin{bmatrix} \cos(\psi) & \sin(\psi) & 0 \\ -\sin(\psi) & \cos(\psi) & 0 \\ 0 & 0 & 1 \end{bmatrix}. \tag{4-7}$$

In (4-6), the first rotation is by angle ψ around the z- axis, the second rotation is by angle θ around the y- axis, and the last rotation is by ϕ around the x- axis. Therefore, the relation between the angular velocity of the vehicle frame coordinate and the change in the Euler angles can be written as:

$$\begin{bmatrix} \dot{\phi} \\ \dot{\theta} \\ \dot{\psi} \end{bmatrix} = Q_{G\to f}^{-1} \begin{bmatrix} \dot{\phi}_f \\ \dot{\theta}_f \\ \dot{\psi}_f \end{bmatrix} = \begin{bmatrix} 1 & -\sin(\phi)\tan(\theta) & \cos(\phi)\tan(\theta) \\ 0 & \cos(\phi) & -\sin(\phi) \\ 0 & -\sin(\phi)/\cos(\theta) & \cos(\phi)/\cos(\theta) \end{bmatrix} \begin{bmatrix} \dot{\phi}_f \\ \dot{\theta}_f \\ \dot{\psi}_f \end{bmatrix} \tag{4-8}$$

However, to calculate the changes in the road bank angle ($\dot{\phi}_r$) or road grade ($\dot{\theta}_r$), one needs to find the angular velocity vector represented in the intermediate coordinate system [87]. This relation can be written as:

$$\begin{bmatrix} \dot{\phi}_r \\ \dot{\theta}_r \\ \dot{\psi}_r \end{bmatrix} = \begin{bmatrix} \cos(\theta) & 0 & 0 \\ 0 & 1 & 0 \\ -\sin(\theta) & 0 & 0 \end{bmatrix} \begin{bmatrix} \dot{\phi} \\ \dot{\theta} \\ \dot{\psi} \end{bmatrix} \tag{4-9}$$

Substitution of (4-8) in (4-9) gives the relationship between the angular velocity vector represented in the intermediate coordinate and the same vector described in the vehicle frame coordinate:

$$\begin{bmatrix} \dot{\phi}_r \\ \dot{\theta}_r \\ \dot{\psi}_r \end{bmatrix} = Q_{f\to i} \begin{bmatrix} \dot{\phi}_f \\ \dot{\theta}_f \\ \dot{\psi}_f \end{bmatrix} \tag{4-10}$$

where

$$Q_{f\to i} = \begin{bmatrix} \cos(\theta) & -\sin(\phi)\sin(\theta) & \cos(\phi)\tan(\theta) \\ 0 & \cos(\phi) & -\sin(\phi) \\ -\sin(\theta) & \sin(\phi)\tan(\theta)\sin(\theta) & -\cos(\phi)\sin(\theta)\tan(\theta) \end{bmatrix} \tag{4-11}$$

The above kinematics equations will be used in the proposed road angle identification algorithm presented in the next sections. Since the vehicle frame angles with respect to the intermediate coordinate system are road angles, angles in (4-11) can be interpreted as the road angles.

4.1.3 Overall identification algorithm

Sensory data used in the proposed identification algorithm (Figure 4.2) are the roll rate ($\dot{\phi}_m$), pitch rate ($\dot{\theta}_m$), longitudinal acceleration ($a_{x,m}$), and lateral acceleration ($a_{y,m}$). Vehicle body angles are the estimated angles in Section 3.1, vehicle longitudinal velocity is the estimated velocity in Section 3.3.1. The rates of estimated vehicle body angles are used to calculate the angular velocity of the vehicle frame coordinates by using (4-5). Then, these signals and the identified bank angle and road grade from the previous step by (A) and (B) in Figure 4.2 are used to calculate the changes in road angles using (4-10). In the next sections, the blocks will be explained in detail.

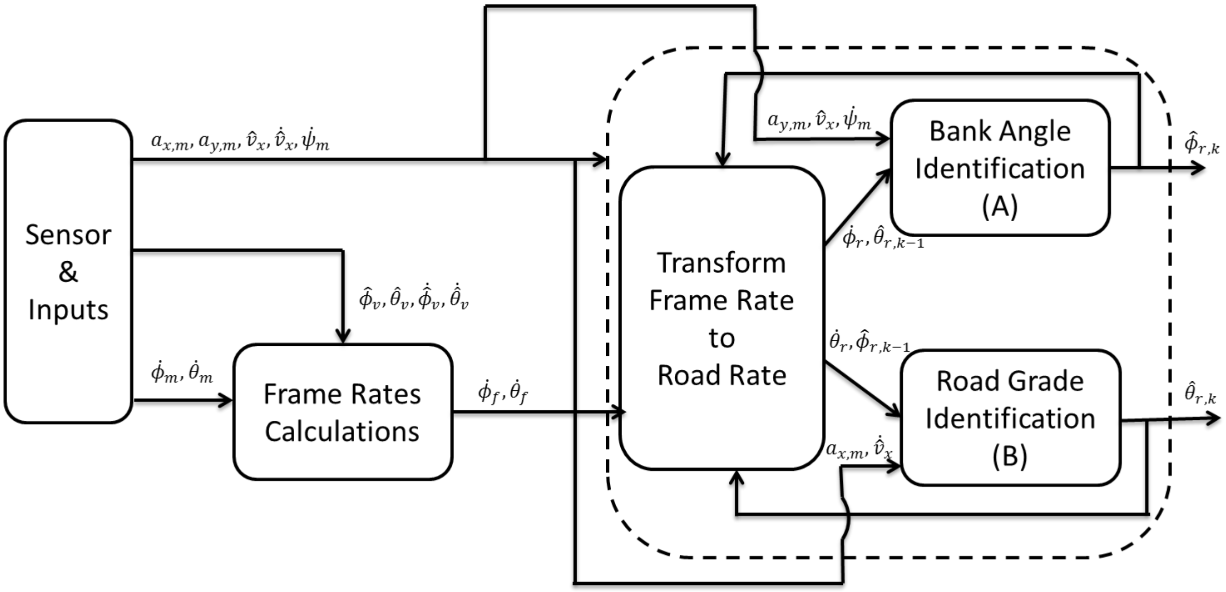

Figure 4.2. Overall identification algorithm structure

4.1.4 Road bank angle identification

In steady state conditions, the changes in vehicle lateral velocity ($\dot{v}_y$) are small; so the road bank angle can be calculated using the lateral kinematics relation:

$$\dot{\boldsymbol{v}}_{\boldsymbol{y}} = \boldsymbol{a}_{\boldsymbol{y,m}} - \dot{\boldsymbol{\psi}}_{\boldsymbol{m}}\, \boldsymbol{v}_{\boldsymbol{x}} - \boldsymbol{g}\boldsymbol{sin}(\boldsymbol{\phi}_{\boldsymbol{v}} + \boldsymbol{\phi}_{\boldsymbol{r}}) \tag{4-12}$$

$$\dot{\boldsymbol{v}}_{\boldsymbol{y}} \approx \boldsymbol{0} \rightarrow \boldsymbol{\phi}_{\boldsymbol{r,s}} = \boldsymbol{sin}^{-\boldsymbol{1}}\left(\frac{\boldsymbol{a}_{\boldsymbol{y,m}} - \dot{\boldsymbol{\psi}}_{\boldsymbol{m}}\boldsymbol{v}_{\boldsymbol{x}}}{\boldsymbol{g}}\right) - \widehat{\boldsymbol{\phi}}_{\boldsymbol{v}} \tag{4-13}$$

However, this is not valid when vehicle is excited in lateral direction ($\dot{v}_y \neq 0$). In this situation, the angular velocity vector in (4-10) is used to calculate the bank angle. The following relationships present the proposed road bank angle observer.

$$\dot{\widehat{\boldsymbol{\phi}}}_{\boldsymbol{r}} = \dot{\boldsymbol{\phi}}_{\boldsymbol{r}} + \boldsymbol{K}_{\boldsymbol{p}}\boldsymbol{e}_{\boldsymbol{bank}} + \boldsymbol{K}_{\boldsymbol{i}}\int \boldsymbol{e}_{\boldsymbol{bank}}\, \boldsymbol{dt} + \boldsymbol{K}_{\boldsymbol{D}}\, \frac{\boldsymbol{de}_{\boldsymbol{bank}}}{\boldsymbol{dt}} \tag{4-14}$$

$$\dot{\widehat{\boldsymbol{\phi}}}_{\boldsymbol{r,f}} = \boldsymbol{a}\, \widehat{\boldsymbol{\phi}}_{\boldsymbol{r,f}} + \boldsymbol{b}\, \widehat{\boldsymbol{\phi}}_{\boldsymbol{r}} + \boldsymbol{K}_{\boldsymbol{1}}\, \boldsymbol{e}_{\boldsymbol{bank}} \tag{4-15}$$

$$\boldsymbol{e}_{\boldsymbol{bank}} = \boldsymbol{\phi}_{\boldsymbol{r,s,f}} - \widehat{\boldsymbol{\phi}}_{\boldsymbol{r,f}} \tag{4-16}$$

where a and b are the low-pass filter coefficient (used in LPF blocks in Figure 4.3), $\hat{\phi}_{r,f}$ is the filtered estimated bank angle, $\phi_{r,s,f}$ is the filtered calculated bank angle in steady state conditions. The estimated bank angle is filtered using the same low-pass filter. In (4-14) the correction terms are in the form of a proportional-integral-derivative (PID) observer. The PID observer's gains (K_p, K_i, and K_D) can be tuned according to test data obtained from the test vehicle as described in Chapter 5. Other correction term in (4-15) has a gain, K_1, that is set to a small value.

Figure 4.3 shows the structure of the bank angle observer. The lateral excitation block monitors the changes in yaw rate and differentiates the yaw rate to recognize the situation when the vehicle is laterally excited. When the vehicle is excited in lateral direction, the yaw rate or its rate is large. In this condition, the output of lateral excitation block would be zero because the calculated $\phi_{r,s}$ is not accurate. Otherwise, the output is unity.

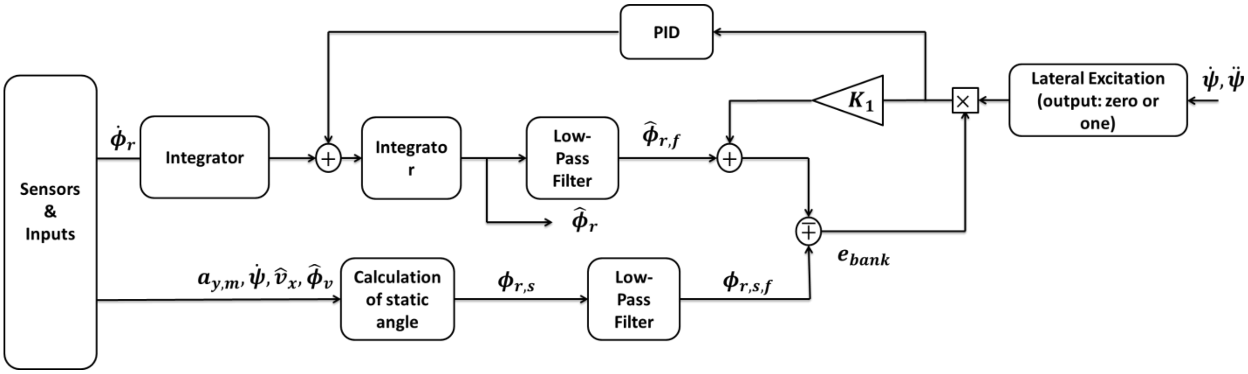

Figure 4.3. Bank angle identification algorithm

4.1.5 Road grade identification

In the longitudinal kinematic relation of the vehicle, (4-17), $\dot{\psi}v_y$ is usually small especially when the vehicle is not excited in the lateral direction.

$$\dot{v}_x = a_{x,m} + \dot{\psi}v_y - g\sin(\hat{\theta}_v + \theta_r) \tag{4-17}$$

When the vehicle is not excited in the lateral direction, the road grade can be calculated as:

$$\theta_{r,s} = a\sin\left(\frac{\dot{v}_x - a_{x,m}}{g}\right) - \hat{\theta}_v \tag{4-18}$$

Therefore, the proposed identifier for the road grade converges to the angle calculated in (4-18) when the vehicle does not have excitation in the lateral direction. When the vehicle is excited in the lateral direction, the road grade will be calculated using $\dot{\theta}_r$ as shown in (4-10). Switching between these two modes can be achieved by a dynamic detector block which has the same logic as discussed in the previous section. The following relationships describe the road grade observer:

$$\boldsymbol{\dot{\hat{\theta}}_r = \dot{\theta}_r + K'_p e_{grade} + K'_i \int e_{grade}\, dt + K'_D \frac{de_{grade}}{dt}} \tag{4-19}$$

$$\boldsymbol{\dot{\hat{\theta}}_{r,f} = a'\, \hat{\theta}_{r,f} + b'\, \hat{\theta}_r + K'_1\, e_{grade}} \tag{4-20}$$

$$\boldsymbol{e_{grade} = \theta_{r,s,f} - \hat{\theta}_{r,f}} \tag{4-21}$$

where a' and b' are the low-pass filter coefficient, $\hat{\theta}_{r,f}$ is the filtered estimated road grade, and $\theta_{r,s,f}$ is the filtered calculated road grade using (4-19) and (4-20). K'_1 is the observer gain which is set to a small value. The PID correction terms used in (4-19) are tuned during experiments.

4.2 Vehicle inertial parameters

In this section, the parameters that have significant effect on the vehicle state estimation algorithms presented in the previous chapter are recognized using a sensitivity analysis. Then, an identification algorithm is developed to identify this parameter.

4.2.1 Sensitivity analysis

The following vehicle inertial parameters are used in the estimation algorithms

- vehicle mass (m)
- COG's longitudinal location (L_f),
- COG's lateral location (Y_{COG}),
- COG's height location (H_{COG}),
- moment of inertia about z-axis (I_{zz}).

These parameters are depicted in Figure 4.4.

The vehicle COG's location and moment of inertia change with changes in the vehicle mass. Vehicle mass changes when extra persons or bags are added into the vehicle. Table 4.1 shows the effect of changes of vehicle mass on these parameters. The information in this table is according to Chevrolet Equinox 2011 specifications. It is assumed that the mass of each person is 80 (kg), and each bag weights 30 (kg).

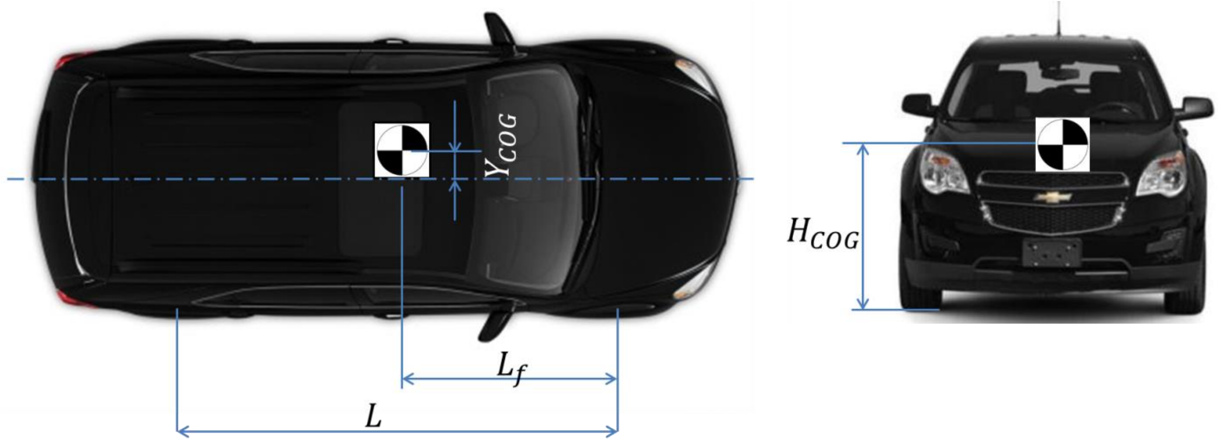

Figure 4.4. Vehicle COG location

This table shows that the maximum changes in the longitudinal location (L_f) of COG, height of COG and moment of inertia around z-axis occur when the driver, 3 passengers and 2 bags are in the vehicle. The longitudinal location of the COG moves back by 122 mm compared to its unloaded position. The height of the COG moves down by 29 mm. The vehicle inertial moment around the z-axis increases by 39.5 kg m^2 The maximum change in the lateral location of COG (Y_{COG}) is encountered when the driver is added to the vehicle. In this case, the lateral location of the COG moves towards the left side of the vehicle by 12.45 mm.

A sensitivity analysis will be applied using the ranges of changes in the vehicle inertial parameters shown in Table 4.1. The purpose of this sensitivity analysis is recognizing the parameters that have significant role on the estimation algorithms proposed in Chapter 3.

The performance of the estimation algorithms in Chapter 3 is evaluated using normalized root mean square error (NRMS), which is calculated as follows:

$$\boldsymbol{NRMS} = \frac{\sqrt{\sum_{i=1}^{N}\left(\boldsymbol{A_{measured}} - \widehat{\boldsymbol{A}}_{\boldsymbol{estimated}}\right)^{2}/\boldsymbol{N}}}{\boldsymbol{max}(|\boldsymbol{A_{measured}}|)} \tag{4-22}$$

where $A_{measured}$ is the measured signal, and $\hat{A}_{estimated}$ is the estimated signal, and N is the number of collected samples during the vehicle maneuver considered in the analysis. The NRMS error considers the whole measured and estimated signals in each maneuver. Therefore, it is used to evaluate the overall performance of the proposed estimation structure during different maneuvers.

Table 4.1. Changes in vehicle inertial parameters

Vehicle mass (kg)	L_f (mm)	Y_{COG} (mm)	H_{COG} (mm)	I_{zz} (kg m^2)
Empty	1421.2	-3.07	647.47	4600
Case1: Empty + Driver	1429.6	-9.38	640.87	4600.5
Case2: Empty + Driver +1 person (front-right)	1437.3	2.86	634.40	4600.6
Case3: Empty + Driver +2 persons (front-right & rear-left)	1471	-8.62	628.72	4606.6
Case4: Empty + Driver +3 Persons (front-right & rear-left & rear-right)	1502.20	2.69	623.20	4617.1
Case5: Empty + Driver +3 persons +2 Bags (front-right & rear-left & rear-right)	1543.3	2.63	618.48	4639.5

4.2.1.1 Sensitivity analysis for tire force estimation algorithms

In this section, the effects of changes in vehicle inertial parameters on tire force estimation algorithms, proposed in Chapter 3, are investigated to recognize the vehicle inertial parameters that need to be identified. The slalom maneuver is selected for this analysis because during this maneuver both longitudinal and lateral dynamics are excited. Figure 4.5 depicts the measured torques acting on each wheel, steering wheel angle, longitudinal and lateral acceleration signals during this maneuver. According to this figure, the vehicle is excited in both longitudinal and lateral directions. During this experimental test, a driver and one passenger are in the vehicle. The tire force estimation algorithms in

Chapter 3 are used for each of the test cases in Table 4.1 to evaluate the effect of changes in each of the parameters by varying one parameter at a time. Table 4.3 to Table 4.7 show the effect of changes in vehicle inertial parameters on the estimated forces.

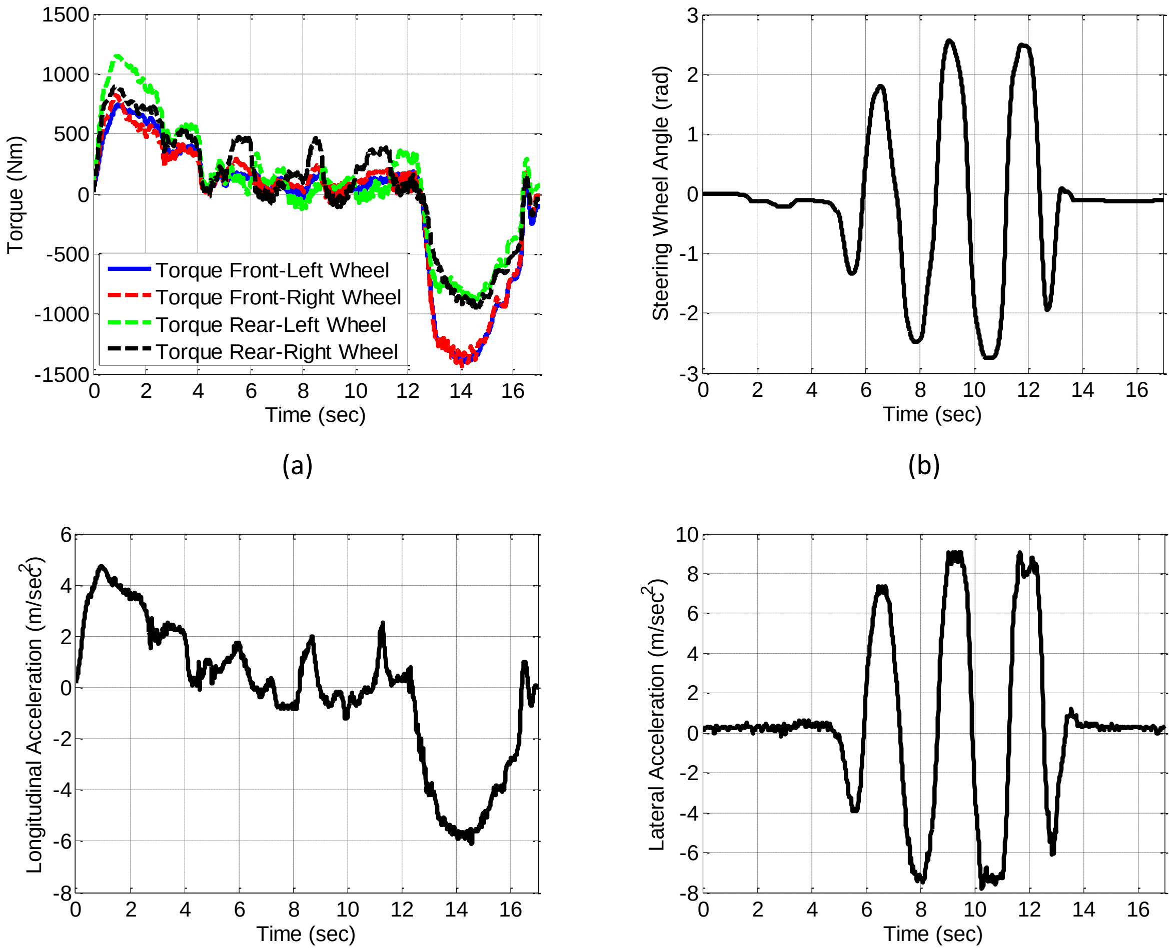

Figure 4.5. Measured signals: (a) torques acting on each wheel, (b) steering wheel angle, (c) longitudinal acceleration, (d) lateral acceleration.

Table 4.2 shows the minimum and maximum values of the measured forces in the vertical and lateral directions. For instance, the differences between minimum and maximum values of the vertical and lateral forces acting on the rear left tire are 6655 N and 9096 N, respectively.

Table 4.2. Minimum and maximum values of the measured vertical and lateral forces

	F_{zfl}(N)	F_{zfr}(N)	F_{zrl}(N)	F_{zrr}(N)	F_{yfl}(N)	F_{yfr}(N)	F_{yrl}(N)	F_{yrr}(N)
Min	1602	1370	1313	1326	-7562	-2953	-5748	-3116
Max	10600	11440	7968	8745	2892	8674	3348	8220

Effect of changes in vehicle mass on the force estimation algorithm

In this section, the sensitivity of the proposed estimation algorithms to changes in vehicle mass is investigated. It is assumed that vehicle mass is the only parameter that changes. These changes are according to cases 1 to 5 discussed in Table 4.1. It is worth mentioning that the proposed estimations algorithm for the longitudinal forces does not use the vehicle mass. Therefore, it is not sensitive to this vehicle parameter.

Table 4.3 shows the effect of changes in the vehicle mass on the estimated vertical and lateral forces acting on each wheel. The variations in the vehicle mass have significant effect on the estimated vertical forces. For example, NRMSE variations are 6.88% to 11.6% for the rear-left tire. The changes in the vehicle mass have an effect on the estimated lateral forces. However, the variations in the calculated NRMSEs in the estimated lateral forces are less than variations of NRMSEs in the estimated vertical forces.

Effect of changes in longitudinal location of the COG on the force estimation algorithm

Table 4.4 shows that the changes in the longitudinal location of the COG have an effect on the estimated vertical forces and lateral forces. NRMSEs for the estimated vertical force of the rear-left wheel show the maximum variations, which are between 7.23% to 10.10%. NRMSEs of the estimated vertical forces for the other tires do not show significant changes. NRMSEs of the estimated lateral forces have small variations. For instance, the variations of NRMSEs for the rear left are between 13.50% to 14.20%.

Table 4.3 Sensitivity of (a) vertical force and (b) lateral estimation algorithm to changes in the vehicle mass

	NRMS (%)				
	Case 1	Case 2	Case 3	Case 4	Case 5
F_{zfl}	7.02	6.91	7.47	8.56	9.62
F_{zfr}	6.39	6.21	6.88	7.67	8.66
F_{zrl}	6.88	7.37	8.56	10.19	11.60
F_{zrr}	6.9	6.29	6.00	6.36	7.24
F_{yfl}	7.49	7.47	7.70	8.11	8.53
F_{yfr}	5.80	5.76	6.37	7.12	7.77
F_{yrl}	13.53	13.52	13.70	14.02	14.36
F_{yrr}	12.75	12.75	12.40	12.15	12.03

Table 4.4 Sensitivity of (a) vertical force and (b) lateral force estimation algorithms to the changes in the longitudinal location of COG

	NRMS (%)				
	Case 1	Case 2	Case 3	Case 4	Case 5
F_{zfl}	6.96	6.85	6.91	7.13	7.90
F_{zfr}	6.24	6.21	6.33	6.62	7.01
F_{zrl}	7.23	7.80	8.61	9.59	10.10
F_{zrr}	6.4	6.08	6.00	6.19	7.16
F_{yfl}	7.49	7.47	7.47	7.53	7.69
F_{yfr}	5.83	5.76	5.51	5.43	5.45
F_{yrl}	13.51	13.52	13.71	13.89	14.20
F_{yrr}	12.82	12.75	12.39	12.23	12.07

Effect of changes in height of COG on the force estimation algorithm

Even though changes in the height of COG have effects on the estimated vertical and lateral force, these effects are not significant according to Table 4.5.

Table 4.5 Sensitivity of (a) vertical force and (b) lateral force estimation algorithm to changes in the height of COG

	NRMS (%)				
	Case 1	Case 2	Case 3	Case 4	Case 5
F_{zfl}	6.84	6.85	7.22	7.30	7.39
F_{zfr}	6.18	6.21	6.44	6.51	6.57
F_{zrl}	7.34	7.80	7.51	7.55	7.59
F_{zrr}	6.28	6.08	6.35	6.38	6.41
F_{yfl}	7.38	7.47	7.81	7.90	7.99
F_{yfr}	5.78	5.76	5.76	5.76	5.76
F_{yrl}	13.62	13.52	13.22	13.75	13.08
F_{yrr}	12.75	12.75	12.75	12.75	12.75

Effect of changes in lateral location of COG on the force estimation algorithm

According to Table 4.6, changes in the lateral location of COG do not have a significant effect on the estimated vehicle vertical and lateral forces.

Table 4.6 Sensitivity of (a) vertical force and (b) lateral force estimation algorithm to changes in the lateral location of COG

	NRMS (%)				
	Case 1	Case 2	Case 3	Case 4	Case 5
F_{zfl}	6.81	6.87	6.80	6.88	6.88
F_{zfr}	6.44	6.26	6.37	6.24	6.25
F_{zrl}	6.99	6.26	7.12	7.31	7.29
F_{zrr}	6.15	6.21	6.09	6.24	6.22
F_{yfl}	7.38	7.47	7.38	7.46	7.46
F_{yfr}	5.78	5.76	5.89	5.82	5.82
F_{yrl}	13.62	13.52	13.61	13.54	13.55
F_{yrr}	12.66	12.75	12.61	12.72	12.71

Effect of changes in moment of inertia around *z*-axis on the force estimation algorithm

The moment of inertia around the *z*-axis, I_{zz}, is only used in the lateral force estimation algorithm. According to Table 4.7, the estimated lateral forces are not sensitive to changes in this parameter.

Table 4.7 Sensitivity of lateral force estimation algorithm to changes in the moment of inertia around *z*-axis

	NRMS (%)				
	Case 1	Case 2	Case 3	Case 4	Case 5
F_{yfl}	7.49	7.47	7.48	7.48	7.47
F_{yfr}	5.80	5.76	5.79	5.78	5.76
F_{yrl}	13.53	13.52	13.52	13.52	13.52
F_{yrr}	12.75	12.75	12.75	12.75	12.75

4.2.1.2 Sensitivity analysis for velocity estimation algorithm

Vehicle inertia parameters used in the velocity estimation algorithms are: vehicle mass, longitudinal, lateral and vertical location of the COG. The slalom maneuver is selected to investigate the sensitivity of the estimation algorithm to these parameters. During this maneuver, minimum and maximum values of the lateral velocity are -2.26 m/sec and 2.30 m/sec. Changes in the longitudinal velocity are between 0 m/sec and 45.23km/hr.

According to Table 4.8 to Table 4.11, changes in the vehicle inertial parameters do not have a significant effect on the estimated lateral and longitudinal velocities. This is one of the benefits of using the kinematic model proposed in Section 3.3 in Chapter 3 to estimate vehicle velocity.

Table 4.8 Sensitivity of longitudinal and lateral velocity estimation algorithms to changes in vehicle mass

	NRMS (%)				
	Case 1	Case 2	Case 3	Case 4	Case 5
V_x	1.13	1.13	1.13	1.13	1.13
V_y	8.30	8.34	8.38	8.43	8.46

Table 4.9 Sensitivity of longitudinal and lateral velocity estimation algorithms to changes in longitudinal location of COG

	NRMS (%)				
	Case 1	Case 2	Case 3	Case 4	Case 5
V_x	1.13	1.13	1.13	1.13	1.13
V_y	8.30	8.34	8.38	8.43	8.46

Table 4.10 Sensitivity of longitudinal and lateral velocity estimation algorithms to changes in lateral location of COG

	NRMS (%)				
	Case 1	Case 2	Case 3	Case 4	Case 5
V_x	1.13	1.13	1.13	1.13	1.13
V_y	8.36	8.34	8.29	8.28	8.27

Table 4.11 Sensitivity of longitudinal and lateral velocity estimation algorithms to changes in moment of inertia around z-axis

	NRMS (%)				
	Case 1	Case 2	Case 3	Case 4	Case 5
V_x	1.13	1.13	1.13	1.13	1.13
V_y	8.36	8.34	8.29	8.28	8.27

4.2.1.3 Sensitivity analysis for roll and pitch angle estimation algorithm

Vehicle mass and height of the COG are two vehicle inertial parameters used in the roll and pitch angle estimation algorithms. It is assumed that the roll and pitch stiffnesses are constant in this analysis.

The double lane change (DLC) maneuver is used to investigate the sensitivity of the roll angle estimation algorithm to changes in the vehicle inertial parameters. During this maneuver, the measured roll angle of the vehicle body is between 3.842 deg and -4.12 deg. NRMSEs in Table 4.12 and Table 4.13 are calculated for the time window when the DLC maneuver is executed. Therefore, the parts of the maneuver where the vehicle is accelerating at the start and is braking at the end are not used in the calculation of these NRMSEs.

Acceleration and braking maneuver, executed in a straight line, is used to analyze the sensitivity of the pitch angle estimation algorithm to vehicle inertial parameters. In this maneuver, the measured pitch angle during this maneuver is between -0.79 deg to 1.35 deg. Figure 4.6 shows the measured longitudinal and lateral acceleration signals related to these maneuvers. In these maneuvers, the driver and two more persons are inside the test vehicle.

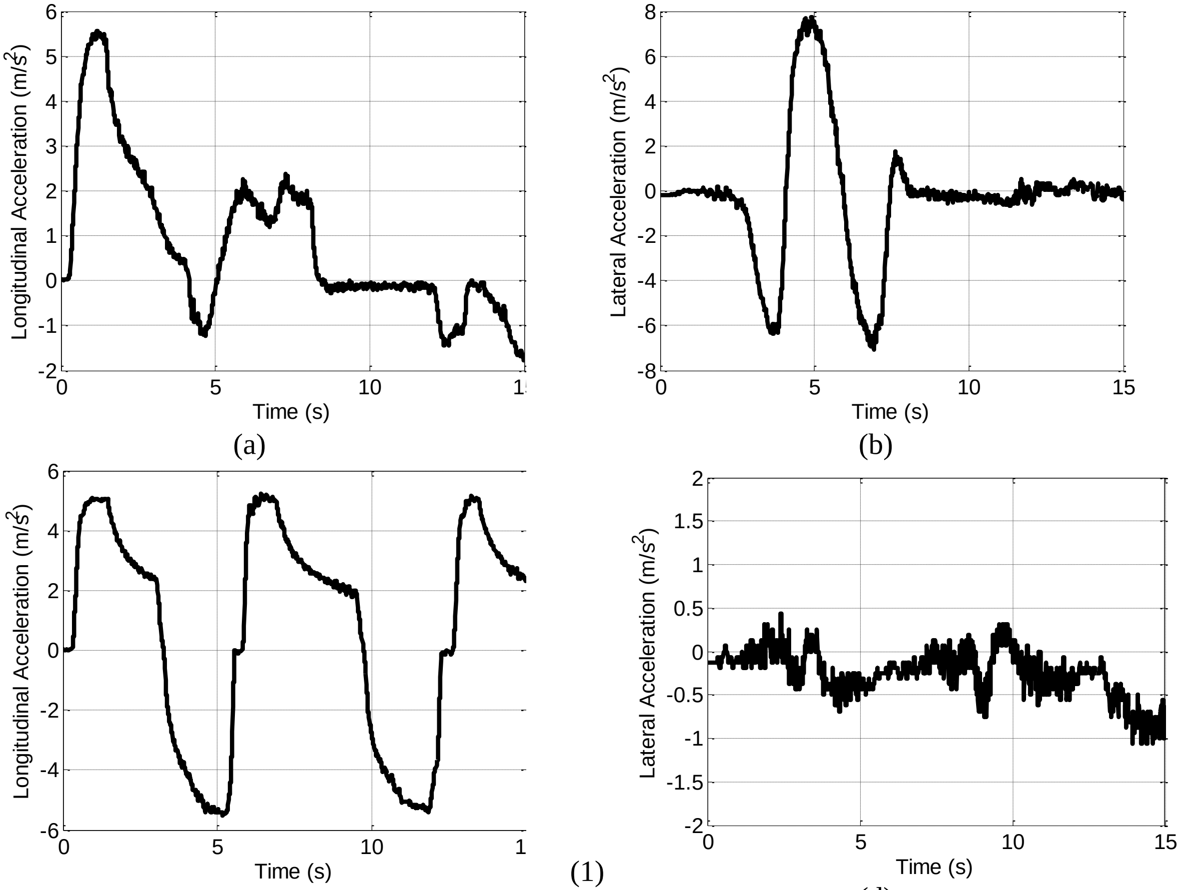

(a) (b)

(c) (1) (d)

Figure 4.6. (a),(b) Measured longitudinal and lateral acceleration during DLC maneuver, (c),(d) measured longitudinal and lateral acceleration during acceleration and brake maneuver.

Table 4.12 and Table 4.13 show the effect of changes in the vehicle mass and height of the COG on the estimated roll and pitch angles. According to these tables, the vehicle mass and height of the COG have visible effects on the estimated roll and pitch angles. However, the changes in vehicle mass have more effect on the estimated roll and pitch angles in comparison to changes in vertical location of the COG. The vertical location of COG does not have considerable effect on roll and pitch angles during the abovementioned maneuvers. Variations in pitch angle are between 6.55% and 9.19% because of changes in the vehicle mass, but variations in this angle are between 6.86% and 8% due to changes in the height of COG.

Table 4.12 Sensitivity of roll and pitch estimation algorithms to changes in vehicle mass

	NRMS (%)				
	Case 1	Case 2	Case 3	Case 4	Case 5
ϕ_v	6.92	5.87	5.39	5.62	6.22
θ_v	9.19	8.17	7.34	8.10	9.00

Table 4.13 Sensitivity of roll and pitch estimation algorithms to changes in height of the COG

	NRMS (%)				
	Case 1	Case 2	Case 3	Case 4	Case 5
ϕ_v	5.53	5.40	5.39	5.51	5.75
θ_v	6.86	7.07	7.34	7.64	8.00

Vehicle mass and longitudinal locations of the COG are the two parameters that have significant effects on the estimated vertical and lateral forces. According to the sensitivity analysis conducted in Section 4.2.1, between these two parameters, the changes in vehicle mass have more effect on the estimated forces.

The sensitivity analyses show that changes in lateral location of the COG and yaw moment of inertia around the *z*-axis do not have significant effects on the estimated forces, velocities and vehicle body angles.

Additionally, changes in the height of the COG have an effect on the estimated forces and roll/pitch angles. But, the impact of changes in this parameter is not comparable to changes in the vehicle mass on the estimated states and forces.

Figure 4.7 depicts the main observation from the results discussed above. It shows that, in this sensitivity analysis, the most important parameter among the vehicle inertial parameters is the mass.

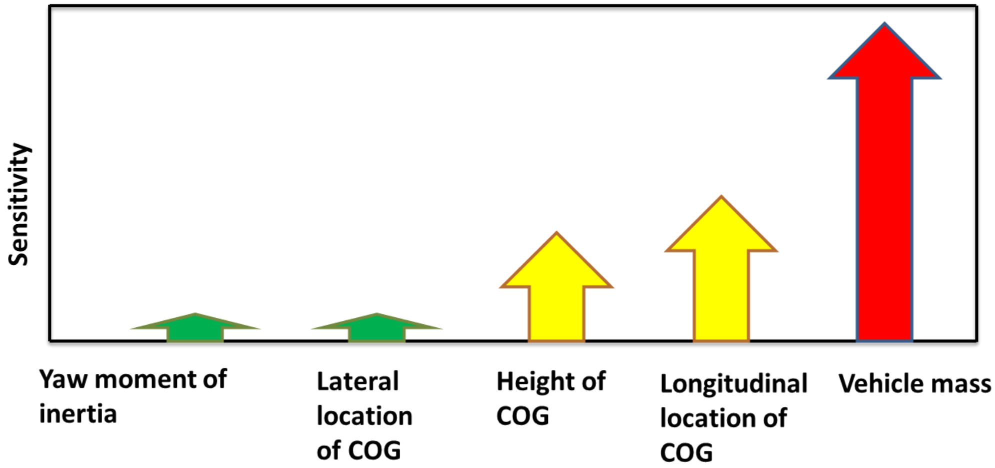

Figure 4.7. Sensitivity of estimation algorithms to the changes in vehicle inertial parameters

Therefore, a vehicle mass identification algorithm is proposed to improve the accuracy of the estimated vehicle states and forces. Furthermore, the identified mass can be further used to determine other vehicle parameters such as longitudinal or vertical location of the COG.

4.2.2 Vehicle mass identification

Extra passengers or luggage will change vehicle mass. In addition, the road grade is an unknown parameter that may change during each journey and has considerable effect on the longitudinal vehicle dynamics. Although, the road grade is identified in the previous section, it is assumed that this angle is an unknown parameter in this section to identify vehicle mass with an independent identification algorithm. In this way, the error that may happen during tests in the proposed algorithm in Section 4.1 does not have any effect on the proposed identification algorithm in this section.

In general, the sum of the vehicle longitudinal forces can be expressed in terms of the longitudinal acceleration as follows

$$\boldsymbol{ma_{x,m} = \Sigma F_x - \frac{1}{2} Q_a A_v v_x^2 - \gamma mg\, cos(\alpha) - mg\, sin(\alpha)} \tag{4-23}$$

where Q_a is the air drag coefficient, A_v is the vehicle front area, v_x is the longitudinal velocity (estimated in Section 3.3.1), γ is the rolling resistance coefficient, α is the summation of vehicle body pitch angle (θ_v) and road grade (θ_r), and g is the gravity constant. In this thesis, it is assumed that the air drag and rolling resistance coefficients are known and fixed. ΣF_x in (4-23) is defined as:

$$\boldsymbol{\Sigma F_x = F_{x,f}\, cos(\delta) - F_{y,f}\, sin(\delta) + F_{x,r}} \tag{4-24}$$

where

$$\boldsymbol{F_{x,f} = \hat{F}_{x,fl} + \hat{F}_{x,fr}} \tag{4-25}$$

$$\boldsymbol{F_{x,r} = \hat{F}_{x,rl} + \hat{F}_{x,rr}} \tag{4-26}$$

In (4-25) and (4-26), $\hat{F}_{x,fl}, \hat{F}_{x,fr}, \hat{F}_{x,rl}, \hat{F}_{x,rr}$ are the estimated longitudinal forces from Section 3.2.1. $F_{y,f}$ is the summation of lateral forces acting on front wheel. By using the moment around the z-axis acting on the rear wheel (see Figure 4.8), $F_{y,f}$ is calculated as:

$$\boldsymbol{I_{zz}\ddot{\psi} = \left(F_{y,f}\, cos(\delta) + F_{x,f}\, sin(\delta)\right)L + m\, a_{y,m} L_r} \tag{4-27}$$

$$\rightarrow \boldsymbol{F_{y,f} = \frac{\left(I_{zz}\ddot{\psi} - F_{x,f}\, sin(\delta)\, L\right)}{L\, cos(\delta)} - m\frac{a_{y,m} L_r}{L\, cos(\delta)}} \tag{4-28}$$

where I_{zz} is the moment of inertia around the z-axis, $\ddot{\psi}$ is the yaw angular acceleration, $a_{y,m}$ is the measured lateral acceleration, L is the wheelbase, L_r is the distance between rear axle of vehicle and the COG, δ is the wheel steering angle, and $F_{y,f}$ is the lateral force acting on the front axle.

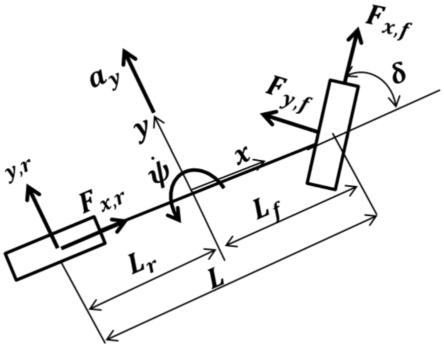

Figure 4.8. Bicycle vehicle model

With substitution of (4-24) and (4-28) in (4-23), the longitudinal dynamics can be presented in a new format:

$$\boldsymbol{Y = \phi_1^T \Psi_1} \tag{4-29}$$

where

$$\boldsymbol{Y = a_{x,m} - \frac{a_{y,m} L_r}{L} tan(\delta)} \tag{4-30}$$

$$\boldsymbol{\phi_1^T = [F_{x,f}\, cos(\delta) - \frac{\left(I_{zz}\ddot{\psi} \ - F_{x,f}\, sin(\delta)\, L\right)}{L} tan(\delta) + F_{x,r} - \frac{1}{2} Q A v^2 \quad - g]} \tag{4-31}$$

$$\boldsymbol{\Psi_1^T = [\frac{1}{m} \quad \gamma\, cos(\alpha) + sin(\alpha\,)]} \tag{4-32}$$

Y is a combination of the measured signals, ϕ_1 is the vector of known variables and parameters, and Ψ_1 is the vector of unknown parameters. The recursive least squares method is used to identify these unknown parameters [49]. Since there is enough excitation in the first part of each journey in the longitudinal direction, vehicle mass can be identified accurately in the first few seconds of each journey. Therefore, a switch is designed to run the recursive least squares (RLS) algorithm until the changes in the identified vehicle mass are small or less than a predefined limit over a period of time. After this time elapse, α is the only unknown parameter in (4-29) that can be calculated. In the remainder of this thesis, the mass according to the method proposed in this section will be used as the vehicle mass.

4.3 Sensitivity analysis for changes in tire parameters

In the longitudinal force estimation algorithms, the effective tire radius and wheel moment of inertia are used. The tire effective radius is used in the velocity estimation algorithm. Additionally, the Lugre tire model used in the lateral velocity estimation algorithm requires several parameters [85]. Therefore, the aim of this section is to conduct an investigation of the sensitivity of the lateral velocity estimation algorithm to changes in these tire parameters.

4.3.1 Sensitivity of the estimation algorithm to effective tire radius

The longitudinal velocity and longitudinal force estimation algorithms use the effective tire radius to estimate vehicle speed and longitudinal forces acting on each tire. This parameter for each tire changes according to load on the tire, wear and tire pressure. Therefore, a reasonable range of changes in the effective tire radius is required to perform the sensitivity analysis.

Information in Table 4.1 is used to calculate the load on each tire by adding extra mass to the vehicle. Next, tire deflection due to the load on each tire is calculated. The equation below [88] is used to calculate the effective tire radius for cases defined in Table 4.1.

$$\boldsymbol{R_{eff}} = \frac{\sin\left(\cos^{-1}\left(\frac{\boldsymbol{R_s}}{\boldsymbol{R_w}}\right)\right)}{\cos^{-1}\left(\frac{\boldsymbol{R_s}}{\boldsymbol{R_w}}\right)}\boldsymbol{R_w} \tag{4-33}$$

where R_s is the loaded radius and R_w is unloaded radius. According to this method, when there are four persons in the car with two bags, the deflection of each tire in the rear is close to 2 mm. Table 4.14 shows the results of a sensitivity analysis with the assumption that changes in the effective tire radius is between 0 mm to 5 mm which is more than twice the value calculated above using (4-33). These NRMSEs are calculated during a slalom maneuver that introduces large lateral load transfers according to Figure 4.5 and Table 4.2. According to Table 4.14, the velocity estimation algorithm is not significantly sensitive to changes in the effective tire radius. Additionally, the sensitivity of the longitudinal tire force estimation algorithm to changes in this parameter is not considerable.

Table 4.14 Sensitivity of longitudinal and lateral velocity and longitudinal forces acting on each wheel to changes in tire effective radius

	NRMS (%)				
	Case 1	Case 2	Case 3	Case 4	Case 5
V_x	1.23	1.39	1.57	1.77	1.99
V_y	8.17	8.36	8.50	8.70	8.80
F_{xfl}	6.35	6.40	6.44	6.49	6.53
F_{xfr}	10.13	10.17	10.22	10.26	10.31
F_{xrl}	7.73	7.75	7.77	7.79	7.82
F_{xrr}	7.30	7.32	7.35	7.37	7.40

4.3.2 Sensitivity of the estimation algorithm to parameters of Lugre tire model

The lateral velocity estimation algorithm uses the inverse Lugre tire model. The parameters of this tire model used in this estimation algorithm are σ_0, σ_1, K. Here, a sensitivity analysis is performed to investigate the sensitivity of the lateral velocity estimation algorithm to changes in these parameters. This sensitivity analysis is performed for a slalom maneuver (see Figure 4.5). In this sensitivity analysis, at each case, one of these parameters for all tires changes from -80% up to 100%. Table 4.15 shows the result of this analysis. This table clearly shows that the estimated lateral velocity in the slalom maneuver, where the vehicle is highly excited in the lateral direction, is not sensitive to changes in tire model parameters (σ_0, σ_1, K).

Table 4.15 Sensitivity analysis of lateral velocity estimation algorithm to changes in tire model parameters

	NRMS (%)				
	Case 1 (-80%)	Case 2 (-40%)	Case 3 (40%)	Case 4 (80%)	Case 5 (100%)
σ_0	8.38	8.34	8.34	8.34	8.34
σ_1	8.34	8.34	8.34	8.34	8.34
K	8.34	8.34	8.34	8.34	8.34

4.4 Summary

In this chapter, road bank and grade angles identification algorithms were proposed. These angles are used as the inputs for vehicle longitudinal and lateral velocity estimation algorithms proposed in Chapter 3. Sensitivity of the tire force estimation algorithm and vehicle state estimation algorithms to changes in parameters used in these algorithms were investigated. In addition, according to the results of the sensitivity analyses, a vehicle mass identification algorithm was proposed. The identified vehicle mass is used in the proposed vehicle state estimation and tire force estimation algorithms in Chapter 3. In the next chapter, the developed algorithms in Chapters 3 and 4 will be validated experimentally using a test vehicle in various road test scenarios.

Chapter 5

Test vehicle and experiments

This chapter begins by presenting the test vehicles. Several tests are defined to calculate the vehicle parameters such as vehicle mass and location of center of gravity. Different scenarios such as double lane change (DLC), slalom, launch, acceleration and brake maneuvers on the dry, slippery and icy roads are used to evaluate the performance of the proposed algorithms in Chapter 3 and 4. Normalized root mean square (NRMS) error is used to compare the measured and estimated signals. The test vehicles are tested in different test track facilities located at Waterloo Fire Department, General Motors Proving Grounds in Milford and Kinross in Michigan, US.

5.1 Test vehicle

Vehicles with different sources of energy, internal combustion engine (ICE) and electric vehicles (EV), and with different powertrain settings (four-wheel drive, rear-wheel drive) have been used to verify the developed estimation/identification algorithms presented in Chapter 3 and 4. These vehicles which are shown in Figure 5.1 are:

- 2006 Cadillac STS (ICE, four-wheel drive)
- 2008 Opel Corsa (EV, four-wheel drive)
- 2011 Equinox (EV, rear-wheel drive)
- 2011 Equinox (EV, four wheel drive)

These vehicles are equipped with multiple sensors and devices to measure the required data to validate the effectiveness of the proposed parameter estimation algorithm. Figure 5.2 shows the sensing equipment available on these vehicles. These sensors are:

- Wheel load measurement system (Figure 5.2 (a) and (e)): This measurement device, which is from the Michigan Scientific Corporation, is used to measure the tire forces (F_x, F_y, F_z), the acting torques on the center of each wheel (M_x, M_y, M_z), and the angular velocities of each wheel. The load wheel interface electronics is used for each wheel force transducer to handle coordinate transformation and the user interface. Figure 5.3 shows that this sensor measures the forces on the side of the wheel. Thus, the force measured at the sensor point should be adjusted based on the wheel geometry to generate the tire forces at the contact patch.

  The specifications of the electric motors (see Figure 5.4) utilized in the EV are used to calculate the drive torques in each wheel. Additionally, braking torques are calculated using the pressure in the braking system.

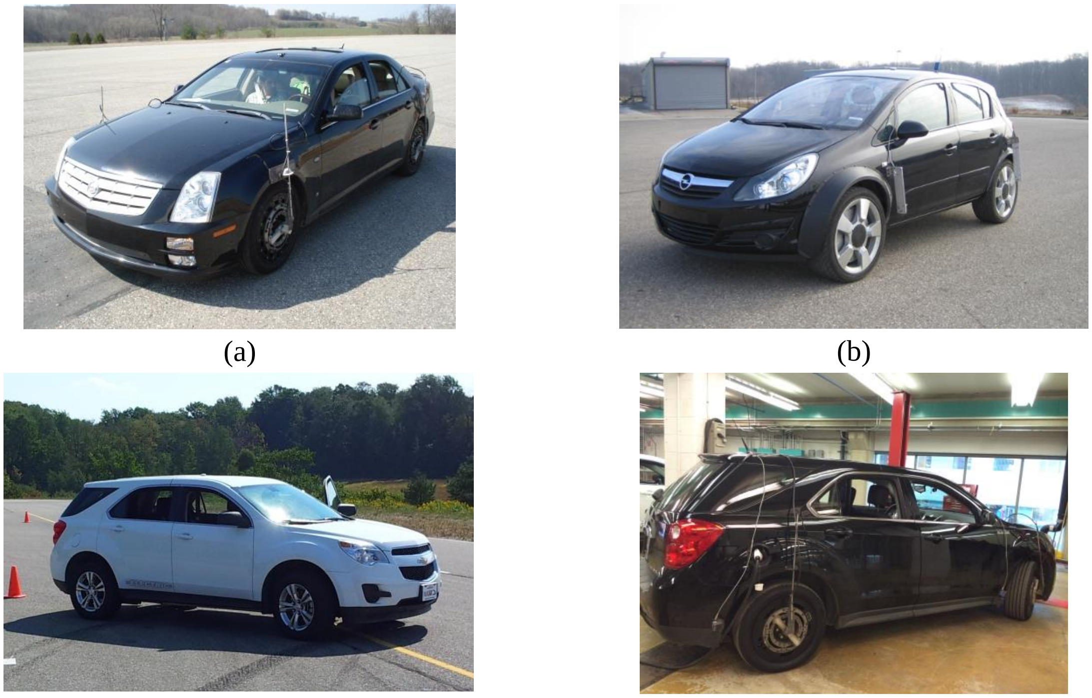

(a) (b)

(c) (d)

Figure 5.1. Test vehicles: (a) 2006 Cadillac STS which is a conventional vehicle, (b) 2008 Opel Corsa which is an EV and four wheel drive, (c) 2011 Chevrolet Equinox which is rear wheel drive and an EV, (d) 2011 Chevrolet Equinox which is four wheel drive and an EV.

(a) Wheel load sensor

(b) AutoBox

(c) Height sensor

(d) GPS antenna

(e) 6-axis IMU

(e) Load wheel interface

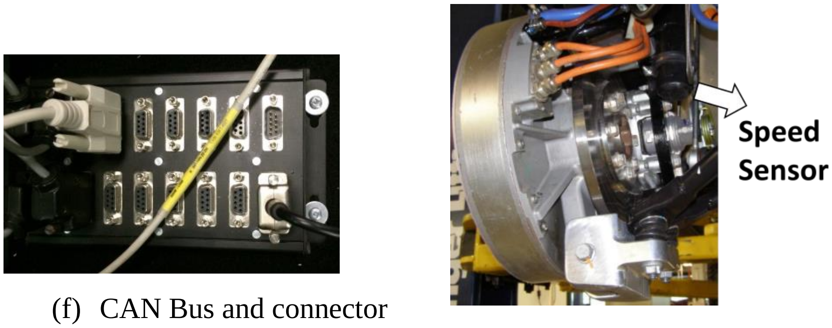

(f) CAN Bus and connector

(g) Speed sensor

Figure 5.2. Sensors and devices used to record data.

- Wheel angular velocity sensors (Figure 5.2 (g)): These signals are available from ABS sensors in the Cadillac vehicle in Figure 5.1 (a). Also, in EV vehicles (Figure 5.1 (b)-(d)), wheel encoders are used to measure the wheel angular velocity.

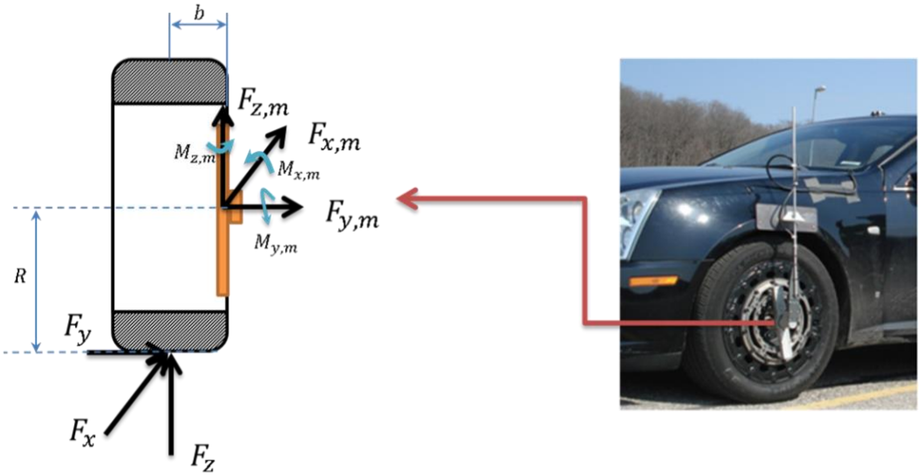

Figure 5.3. Location of measurement unit

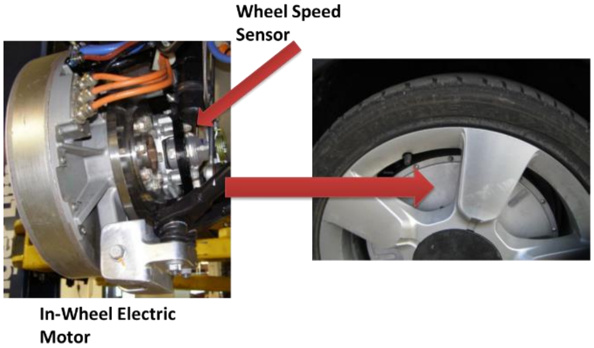

Figure 5.4. In-wheel motor

- Inertial and GPS navigation system (Figure 5.2 (d) and (e)): The RT2500 Inertial and GPS Navigation System from OxTS Company is used in the experiments. This product is a compact device that includes the inertial measurement unit (IMU) and GPS. The IMU is a six axis unit that can measure longitudinal, lateral and vertical accelerations, as well as roll, yaw and pitch rates. Longitudinal and lateral velocity of the vehicle and location of the vehicle are the measured signals using the GPS.

- Optical sensor: This sensor is used to measure the longitudinal and lateral velocity of the vehicle.
- 3-axis IMU: This sensor is the stock IMU used by vehicle stability control system. Yaw rate and longitudinal and lateral accelerations of the vehicle are measured using this sensor.
- Steering wheel angle sensor: The steering wheel angle is measured using an encoder. Therefore, the steering angle of the front wheels is available using the measured signal and the reduction ratio of the steering mechanism. To obtain this ratio, a simple test procedure was designed. Initially, the steering wheel was tuned. Then, its angle and the angle of front wheels were recorded for a number of predefined angles. Figure 5.5 depicts the way that the angle of the wheel was calculated.

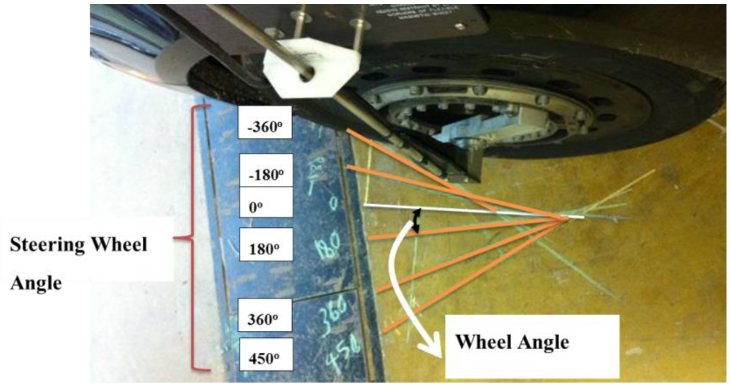

Figure 5.5. Calculated angles of the left-front wheel on the ground for gear ratio measurement

- Height sensors (Figure 5.2 (c)): These are laser sensors that are installed at each corner of the vehicle body to measure the vertical displacement of the vehicle body at that corner. In the stationary condition on a flat surface, the outputs of these sensors are not exactly the height of each corner, as they often have offsets, see Figure 5.6. Theses offsets are calculated to measure vertical displacements at each corner with higher accuracy. These vertical displacements are used to calculate the roll and pitch angles of vehicle body by:

$$\boldsymbol{\theta_{v,m}} = \left(\frac{\boldsymbol{h_{fl} + h_{fr} - (h_{rl} + h_{rr})}}{\boldsymbol{2L}}\right) \tag{5-1}$$

$$\boldsymbol{\phi_{v,m}} = \left(\frac{\boldsymbol{h_{fl} + h_{rl} - (h_{fr} + h_{rr})}}{\boldsymbol{2e_f}}\right) \tag{5-2}$$

where h_{fl}, h_{rl}, h_{fr}, h_{rr} are vertical displacement of front-left, rear-left, front-right and rear-right corners of vehicle, respectively. The calculated pitch angle and roll angle of the vehicle body are $\theta_{v,m}$ and $\phi_{v,m}$, respectively.

Figure 5.6. Difference between measured height with the height sensor and vertical distance between sensor and ground

Figure 5.7 shows the connection map of abovementioned sensor is used for gathering vehicle data. The sampling rate is 200 Hz. Control Area Network (CAN), and the load wheel interface electronic box sends the analog signals data to the AutoBox module. The Autobox is a box that contains processor and input/output boards, and is a convenient environment for using a dSpace real-time system for experiments. The proposed estimation algorithms developed in Chapters 3 and 4 are coded in MATLAB/SIMULINK and implemented on the real-time computer in the AutoBox. The data is then sent to a laptop computer for processing and visualization. This processing is done during the tests and in real-time.

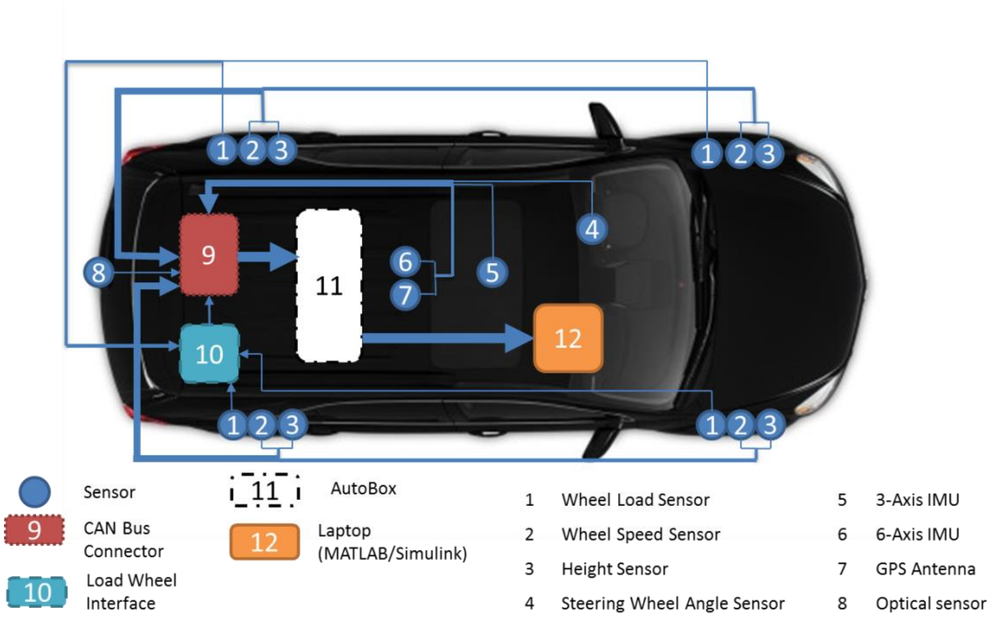

Figure 5.7. Experiment setup for data collection and online estimation

5.2 Vehicle parameters

Vehicle parameters such as the wheelbase, front and rear width tracks are quite easy to measure. However, parameters such as the center of gravity location and wheel moment of inertia require more calculations to compute. In this section, the methods used to calculate the vehicle parameters are discussed.

Center of gravity (COG) location

The location of the COG is an important parameter for the proposed estimation algorithms in Chapters 3 and 4. To calculate the location of the COG in the horizontal plane, four weight scales were used to measure the weight of the vehicle in the corners (see Figure 5.8). By using this static information, the location of the COG is calculated using:

$$L_f = \frac{F_{zrl} + F_{zrr}}{m\,g}\,L \tag{5-3}$$

$$L_r = L - L_f \tag{5-4}$$

$$L_{srl} = L_{sfl} = \frac{(F_{zfl} + F_{zrl})}{mg}\,e_f \tag{5-5}$$

$$L_{srr} = L_{sfr} = e_f - L_{sfl} \tag{5-6}$$

where L_f, L_r are the distances between the front and rear of the vehicle and the COG, respectively. The vehicle wheelbase is L, and F_{zfl} , F_{zrl} are the vertical forces acting on the front-left wheel and rear-left wheel, respectively. The front-track width is e_f, and L_{sfl}, L_{sfr}, L_{srl}, L_{srr} are the distances between the COG and the four corners of the vehicle. It is assumed that the front and rear track widths are the same.

To calculate the height of the COG, the vehicle is located on an inclined surface as shown in Figure 5.9. The vertical forces acting on the front and rear wheels and the surface angle (θ_h) are used to calculate height of the COG [89]-[90].

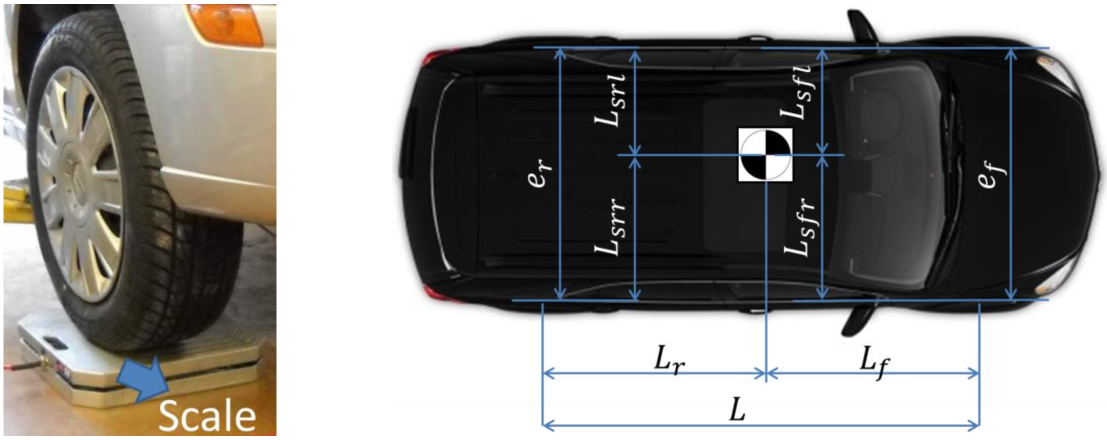

(a) (b)

Figure 5.8. (a) Scale used to measure weight at each corner, (b) location of COG

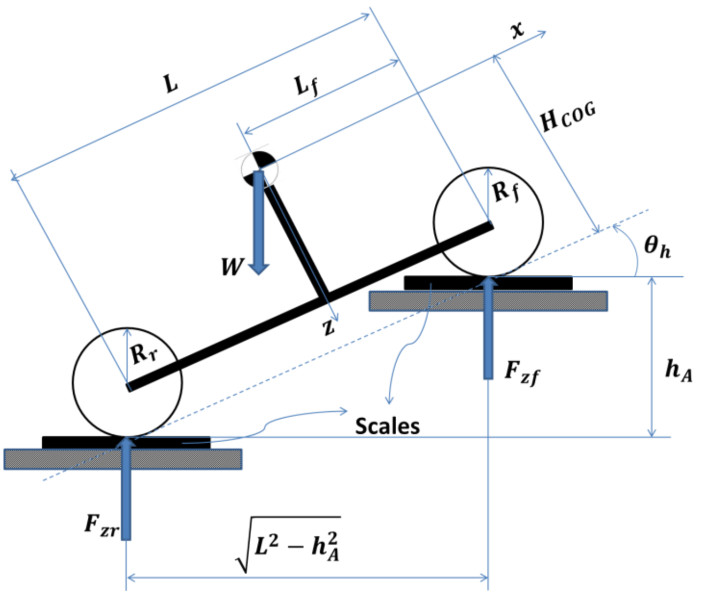

Figure 5.9. Vehicle sitting on the scale to measure height of COG

Summation of force moments about the front axle in Figure 5.9 yields:

$$\sum M_f = F_{zr}\sqrt{L^2 - h_A^2} - W\left(L_f Cos(\theta_h) + \left(H_{COG} - R_f\right)Sin(\theta_h)\right) = 0 \tag{5-7}$$

where h_A is the height of front wheels, θ_h is the angle of surface, R_f is the radius of front wheel. Solving (5-7) for H_{COG} gives:

$$H_{COG} = \frac{L\,(F_{zr} - F_{zr,s})\sqrt{L^2 - h_A^2}}{W\,h_A} + R_f \tag{5-8}$$

where $F_{zr,s}$ is the vertical force acting on the rear axle on the flat surface in the stationary case:

$$F_{zr,s} = \frac{L_f\,W}{L} \tag{5-9}$$

In (5-7) and (5-8), it is assumed that the rear and front tires have the same wheel radius.

Wheel moment of inertia

To calculate the wheel moment of inertia, the left and right front tires are removed and then connected together by a wire. The COG of the connected tires is located in the middle plane. Next, a roll test was designed to calculate the wheel moment of inertia based on [73]. The connected wheels were released from the top of an inclined surface, and the time t was recorded when the wheels reached the bottom of the surface. This test was performed 10 times for different ramp heights. The wheel moment of inertia was then calculated using:

$$\boldsymbol{I_w = \frac{1}{2}\left(\frac{2mghR^2t^2}{l^2} - mR^2\right)} \tag{5-10}$$

where m is the mass of wheels, h is the height of the ramp, l is the length of ramp, R is the wheel radius, and I_w is the wheel moment of inertia. This parameter was calculated for each test; the average of these parameters for all the tests was used as the wheel moment of inerta. Moreover, it is assumed that the wheel moment of inertia of the four wheels is the same.

5.3 Observers gain tuning

The gains in the developed estimation algorithms in Chapter 3 need to be tuned prior to implementation on actual vehicles. In this section, the observers gains tuning approach is discussed.

The observers gains in the roll and pitch angle estimation algorithms are tuned according to the vehicle behavior and based on the rules discussed in Section 3.1.2.

The same estimation algorithm is used to estimate the longitudinal forces acting on the four wheels. The range for each observer gain was calculated to satisfy the Lyapunov stability criteria discussed in Section 3.2.1. Table 5.1 shows the observer gains used in the experimental tests that will be discussed in the next section.

Table 5.1 PID gains used in longitudinal force estimation algorithm

K_p	K_i	K_d
100	1	0.001

The performance of UKF is compared with that of the EKF [80] for the same initial conditions and covariance matrices in the lateral force estimation algorithm. The required parameters for these methods are summarized in Table 5.2. In this table, n_{Fy} is the number of states, α_{Fy} and ϵ_{Fy} are responsible for distribution of the sigma points around the mean value of the states. α_{Fy} should be a small number $(10^{-4} \leq \alpha_{Fy} \leq 1)$ [84], and ϵ_{Fy} is set to a small number as well. Q_{Fy} is a pre-specified process noise covariance matrix. Uncertainties in the covariance prediction are represented by an average noise level $(Q_{Fy} = 0.1^2 I_{2\times2})$. R_{Fy} is measurement noise covariance matrix which is assumed to have a normal distribution with zero mean values. If the sensors have good measurement accuracy, the additive noises are small $(R_{Fy} = 0.01^2 I_{3\times3})$. Both R_{Fy} and Q_{Fy} are assumed to be diagonal matrixes. Consequently, the process and measurements noises are uncorrelated.

Table 5.2 UKF and EKF Parameters, matrixes and initial values used in lateral force estimation algorithm

Symbol	Quantity (UKF)	Quantity (EKF)
n_{Fy}	2	2
α_{Fy}	0.5	-
ϵ_{Fy}	0.1	-
β_{Fy}	2	-
Q_{Fy}	$0.1^2\mathbf{I}_{2\times2}$	$0.1^2\mathbf{I}_{2\times2}$
R_{Fy}	$0.01^2\mathbf{I}_{3\times3}$	$0.01^2\mathbf{I}_{3\times3}$
$X_{0,Fy}$	[0,0]	[0,0]

The Kalman filter used in the longitudinal velocity estimation algorithms requires the initial conditions, covariance matrix of the process noise and the covariance matrix of the measurement noise are listed in Table 5.3.

The tire model used in the lateral velocity estimation algorithm requires several parameters. These parameters have different values for the tires used in each test vehicle. For instance, tire parameters of the Opel Corsa are tabulated in Table 5.4. The Vehicle Researchteam at University of Waterloo has tuned these parameters according to experimental data.

Table 5.3 KF Parameters, matrixes and initial values used in longitudinal velocity estimation algorithms

Matrix	Value
$\boldsymbol{Q_{vx}}$	$0.01^2\ \mathbf{I}_{2\times2}$
$\boldsymbol{R_{vx}}$	$0.001^2\ \mathbf{I}_{4\times4}$
$\boldsymbol{X_{0,vx}}$	[0,0]

Table 5.4 Parameters of 1-D Lugre tire model.

Parameter Unit	$\boldsymbol{\sigma_0}$ $(\mathbf{1/m})$	$\boldsymbol{\sigma_1}$ $(\boldsymbol{s/m})$	$\boldsymbol{\sigma_2}$ $(\boldsymbol{s/m})$	$\boldsymbol{K}$ $(\mathbf{1/m})$	$\boldsymbol{\mu_C}$ (-)	$\boldsymbol{\mu_S}$ (-)	$\boldsymbol{R_{e,ij}}$ $(\boldsymbol{m})$
Front-left tire	100	0.8	0	18	1.1	1.4	0.351
Front-right tire	100	0.8	0	18	1.1	1.4	0.351
Rear-left tire	100	0.8	0	18	1.1	1.4	0.351
Rear-right tire	100	0.8	0	18	1.1	1.4	0.351

5.4 Test results

In this section, the performance of the developed estimation and identification algorithms in Chapters 3 and 4 are investigated. Estimated forces and states are compared with the output of sensors on the test vehicles, and parameters are compared with the actual ones. It must be mentioned that at each experiment, the number of passengers inside the vehicle was recorded to calculate the actual values of the vehicle parameters.

5.4.1 Roll and pitch angle estimation algorithms

The performance of the roll and pitch angles estimation algorithms is evaluated during two harsh maneuvers that excite the vehicle in both longitudinal and lateral directions.

5.4.1.1 Acceleration and braking maneuver

In the first maneuver, the vehicle is accelerated from zero speed and then the driver pushes down the brake pedal, fast. The driver repeates this maneuver two more times in a straight line. In this maneuver, the vehicle is highly excited in the longitudinal direction. Figure 5.10 shows the measurment signals, which are longitudinal and lateral accelerations, steering wheel angle and vehicle longitudinal speed. The longitudinal acceleration is changing between -5.5 $\mathrm{m/sec^2}$ and 5 $\mathrm{m/sec^2}$, and the lateral acceleration between -1 $\mathrm{m/sec^2}$ and 0.5 $\mathrm{m/sec^2}$.

Figure 5.11 shows a comparison between the measured and estimated vehicle body's pitch and roll angles. This figure shows that vehicle pitch angle estimated accurately. The calculated NRMSE discussed in Section 4.2.1 during this test is 6.28% for pitch angle. The maximum of the vehicle body pitch angle is 1.68 deg which happens because of longitudinal load transfer. The estimated pitch angle is accurately following the calculated angle obtained using the height sensors on the test vehicle with (5-1) and (5-2). The calculated NRMSE for roll angle is 22.56%. In this test, the roll angle of vehicle body is small and its maximum value is less than one degree. Therefore, the RMS error between the estimated and measured roll angles is less than 0.2 deg.

5.4.1.2 Double lane change (DLC) maneuver

According to Figure 5.12, in this maneuver, the vehicle is accelerated and then excited in the lateral direction while applying the steering angle. In addition, during time 5 s to 8 s, the vhicle is also excited in the longitudinal direction. Therefore, in this maneuver, there are three types of excitation: 1-longitudinal excitation, 2-lateral excitation, 3- combination of longitudinal and lateral excitation.

Figure 5.13 compares the angles from the estimation algorithm and the measured angles. The estimated roll angle is accurately tracking the measured roll angle of vehicle body. During this maneuver the roll angle of vehicle body is between -4 deg to 3.8 deg. The calculated NRMSE between estimated and measured signals is 7.88% for the roll angle. The estimated pitch angle is also following the measured pitch angle of the vehicle body. The maximum pitch angle, which is 1.5 deg, is related to the first part of the maneuver that is estimated accurately. In addition, when the vehicle is exciting in both longitudinal and lateral direction, the pitch angle is estimated accurately, as well. NRMSE between measured and estimated signals is 9.63% for the pitch angle.

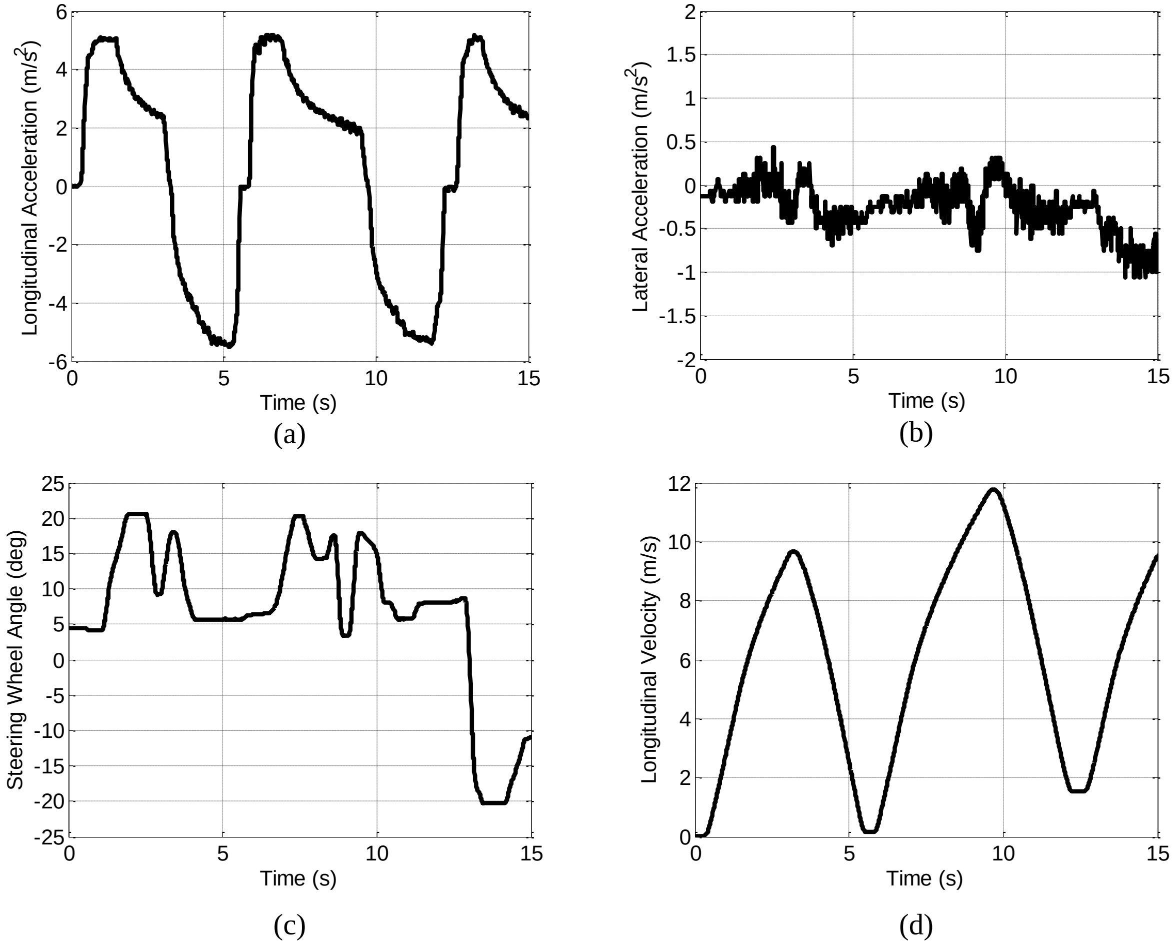

Figure 5.10. Acceleration and braking maneuver: (a) vehicle longitudinal acceleration, (b) lateral acceleration, (c) steering wheel angle, (d) longitudinal velocity.

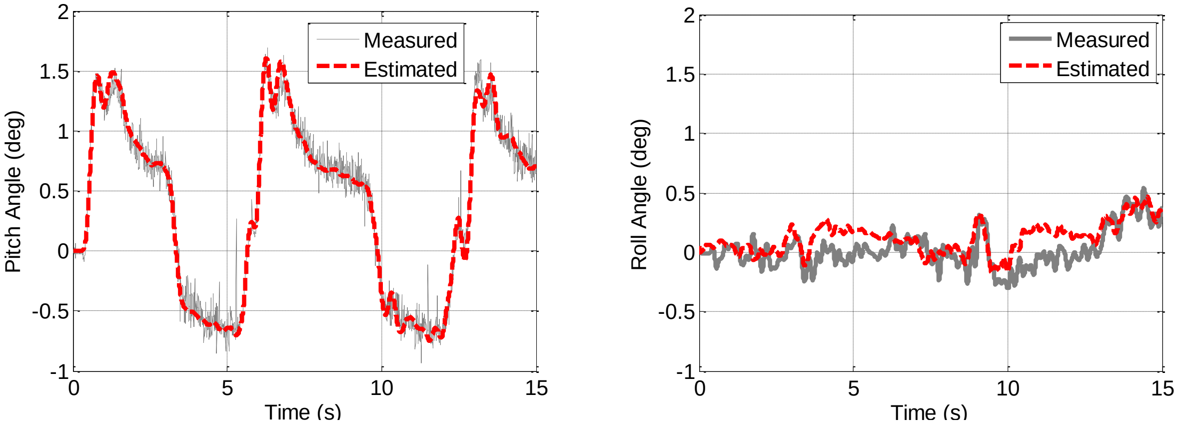

(a) (b)

Figure 5.11. Acceleration and braking maneuver: (a) estimated pitch angle, (b) estimated roll angle

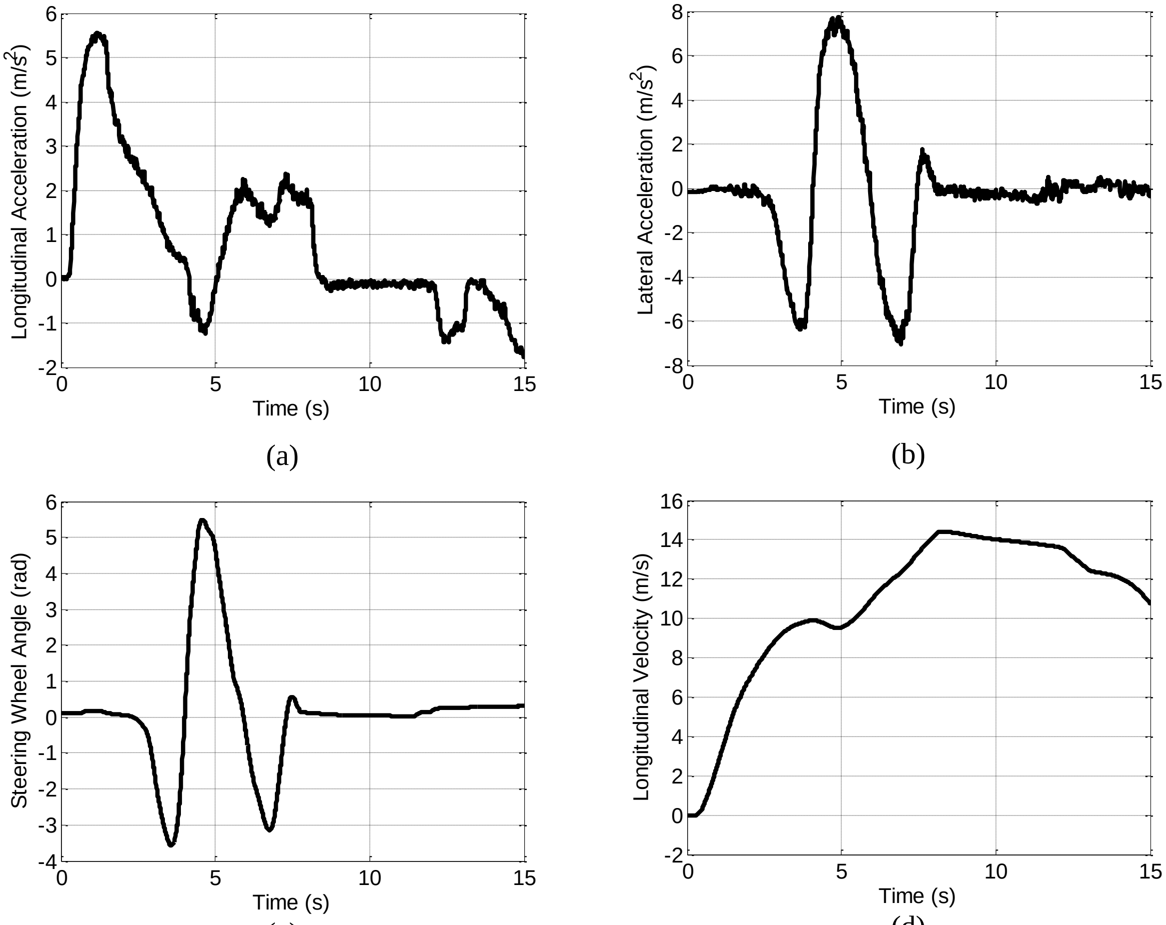

(a) (b)

(c) (d)

Figure 5.12. DLC maneuver: (a) vehicle longitudinal acceleration, (b) vehicle lateral acceleration, (c) vehicle steering angle, (d) vehicle speed.

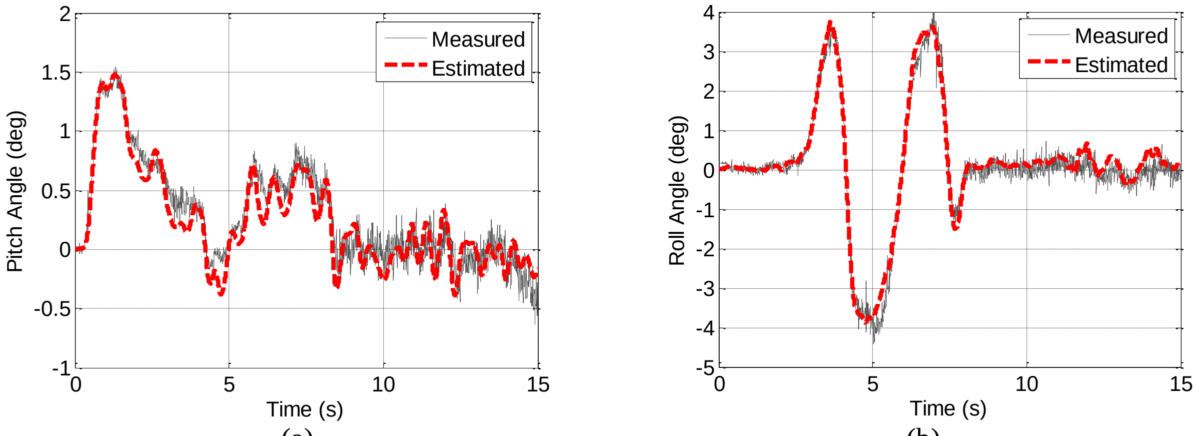

(a) (b)

Figure 5.13. DLC maneuver: (a) estimated pitch angle, (b) estimated roll angle

5.4.2 Tire force estimation algorithm and vehicle mass identification algorithm

In this section, the experiment results for three different scenarios are discussed. Two maneuvers have been done on the dry road, and the last one has been done on the slippery road. The performance of UKF is compared with that of the EKF for the same initial conditions and covariance matrices to estimate the lateral forces acting on each wheel.

5.4.2.1 Slalom test

In this test, as shown in Figure 5.14, a slalom maneuver is performed at a constant velocity of 55 $\mathrm{km/hr}$. High lateral acceleration in the range of $-7.83 \leq a_{y,m} \leq 8.94\ \mathrm{m\ s^{-2}}$ was observed during the maneuver, which enables assessment of the estimation performance for nonlinear tire regions. Additionally, in the first part of the maneuver, the vehicle is accelerated to $a_{x,m} = 4.75\ \mathrm{m\ s^{-2}}$, and the friction brakes when applied to all wheels during the time between $12\ \mathrm{s}$ and $16\ \mathrm{s}$. The minimum longitudinal acceleration is $-6.05\ \mathrm{m\ s^{-2}}$ for this maneuver.

a) Identification of vehicle mass

Since the vehicle is accelerated in the first part of the maneuver, there is enough excitation in the longitudinal direction to identify the vehicle mass. Figure 5.15 shows the performance of the proposed identification algorithm in Section 4.2.2. The error between the identified vehicle mass and the actual mass is 2.91%. Also, the identification algorithm’s output converges to the final estimate in less than 5 seconds.

b) Estimation of longitudinal tire forces

Figure 5.16 depicts the comparison between estimated and measured longitudinal tire forces during the slalom maneuver. The test vehicle is a four-wheel drive and the torques distribution for front and rear wheels are different. Figure 5.16 demonstrates that the estimation algorithm’s performance is accurate in estimating the longitudinal forces for such maneuver and the convergence speed is reasonably fast. Nevertheless, there are small differences between the measured and estimated longitudinal forces in some regions. The main source of these discrepancies is the unmodeled rolling resistance and air drag forces. However, based on the results given in Table 5.5, the performance of the estimator is satisfactory. NRMS errors for all wheels are between 4.44% and 7.07%.

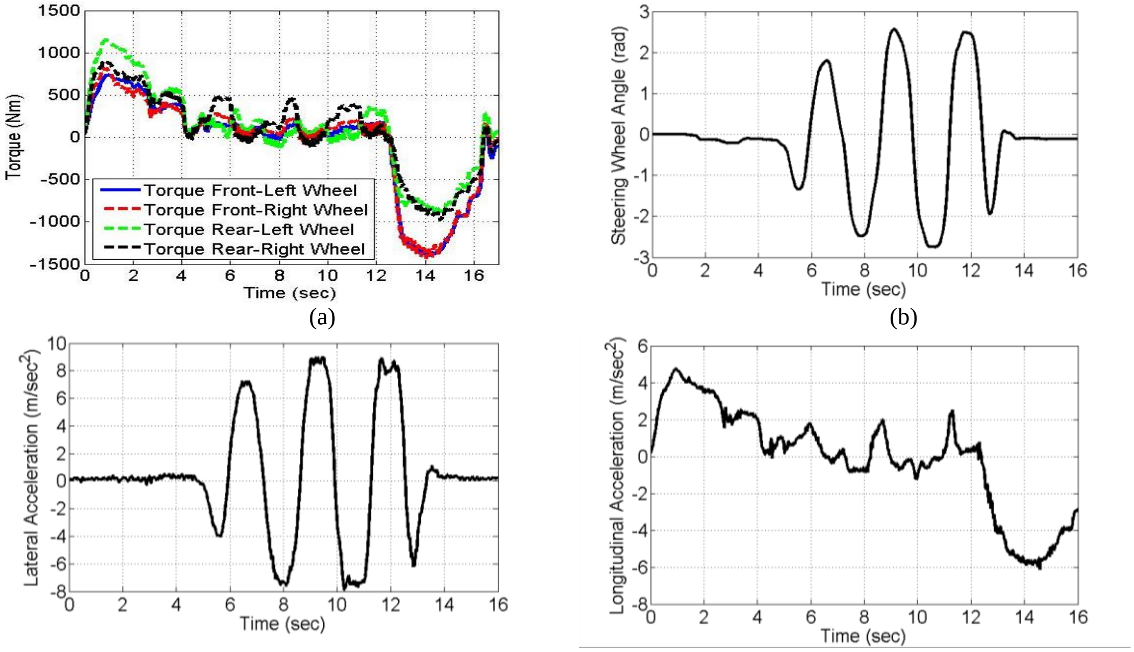

(a) (b)

(c) (d)

Figure 5.14. Slalom maneuver: (a) Torques acting on each wheel, (b) Steering wheel angle, (c) Lateral acceleration, (d) Longitudinal acceleration

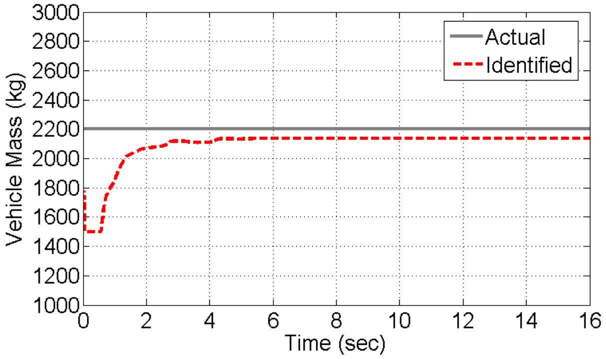

Figure 5.15. Comparison between the actual vehicle mass and identified mass.

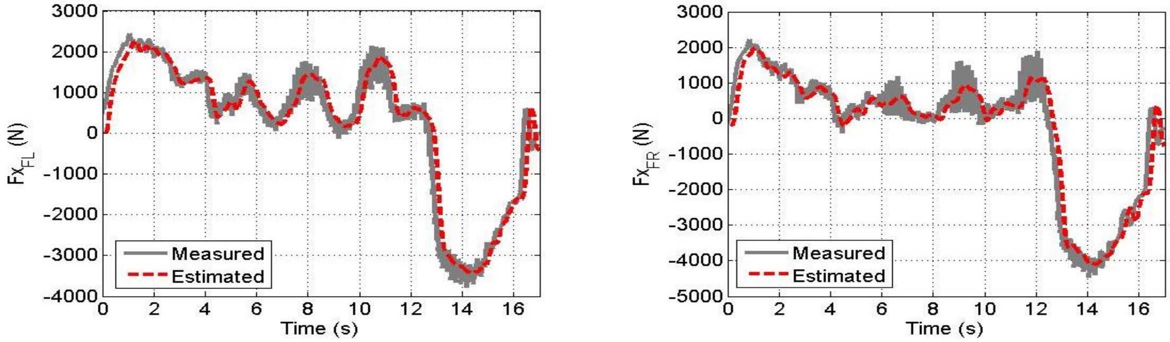

(a) Front-left tire (b) Front-right tire

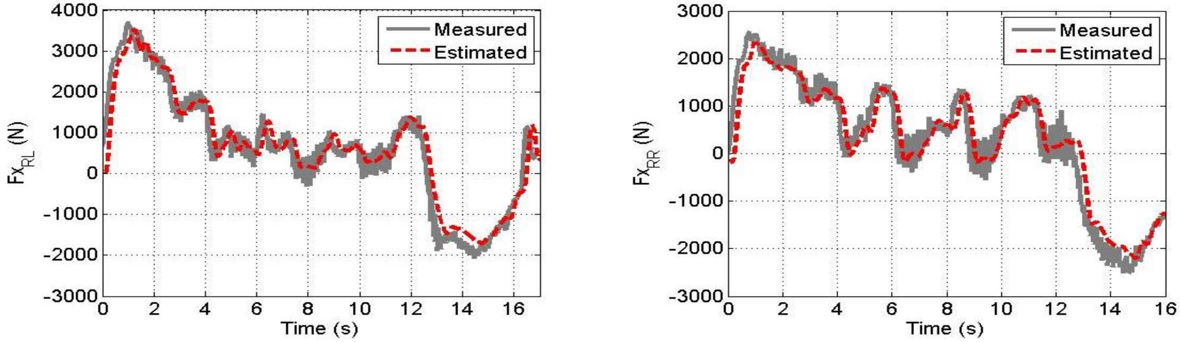

(c) Rear-left tire (d) Rear-right tire

Figure 5.16. Estimation results for longitudinal tire forces

Table 5.5. NRMS errors and maximum longitudinal forces acting on four wheels

	$F_{x_{fl}}$	$F_{x_{fr}}$	$F_{x_{rl}}$	$F_{x_{rr}}$
$Max\ \lvert.\rvert\ (N)$	3986.7	4691.3	3710.3	2799.7
$NRMS\ (\%)$	5.16	4.44	7.07	6.67

c) Calculation of vertical tire forces

Figure 5.17 depicts calculated vertical tire forces versus their measured signals. The results in the figure show that the calculated tire vertical forces match the measured forces by the wheel load measurement system. There are differences between calculated and measured forces in the first part of the maneuver because of the initial error in the identified vehicle mass. As a result of the longitudinal load transfer to the back of vehicle, these errors are larger on the rear wheels. Additionally, uncertainties in the estimates of other vehicle inertial parameters such as location of centre of gravity contribute to these errors. NRMS errors and maximum absolute normal forces are tabulated in Table 5.6. NRMS errors are less than 7% for all four wheels.

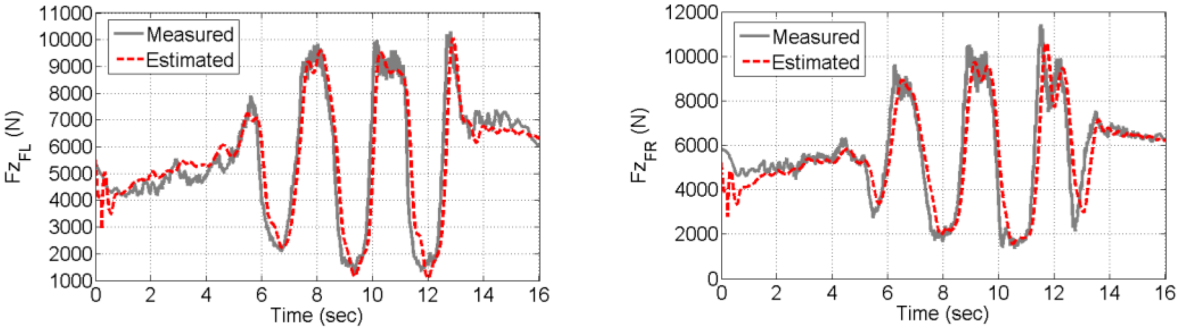

(a) Front-left tire (b) Front-right tire

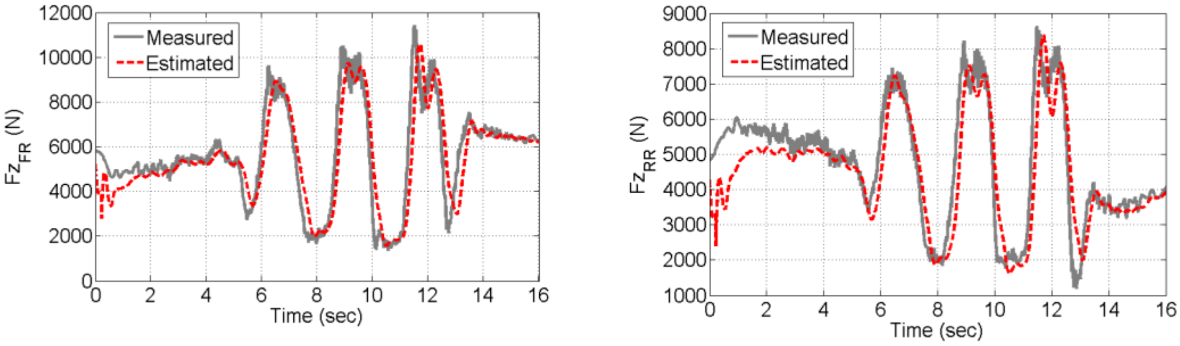

(c) Rear-left tire (d) Rear-right tire

Figure 5.17. Estimation results for vertical tire-road friction force by using 6-axis IMU signals

Table 5.6. NRMS errors and maximum normal forces acting on four wheels

	$F_{z_{fl}}$	$F_{z_{fr}}$	$F_{z_{rl}}$	$F_{z_{rr}}$
$Max\,|.|\,(N)$	10305	11436	7859	8645
$NRMS$ (%)	5.37	5.17	7.00	6.80

d) Estimation of lateral tire forces

Figure 5.18 shows the estimated and measured lateral tire forces acting on each wheel. The results in this figure indicate that the performances of EKF and UKF are comparable. Table 5.7 shows the maximum lateral force acting on each wheel and NRMS errors. NRMS errors between measured and estimated forces are between 7.2% and 13.54%. Because the vehicle is highly excited in lateral direction, there are several factors that contribute to the errors in Table 5.7. Camber angle is one of these factors. The test vehicle's wheels have positive camber angle. Uncertainties in vehicle inertial parameters are other source of errors between estimated and measured lateral forces.

Table 5.7. NRMS errors and maximum lateral forces acting on four wheels

	${F_y}_{fl}$	${F_y}_{fr}$	${F_y}_{rl}$	${F_y}_{rr}$
$Max\ \lvert . \rvert\ (N)$	7993.9	9089.3	4884.6	7420.3
$NRMS$ (%)	9.3	7.2	13.54	11.25

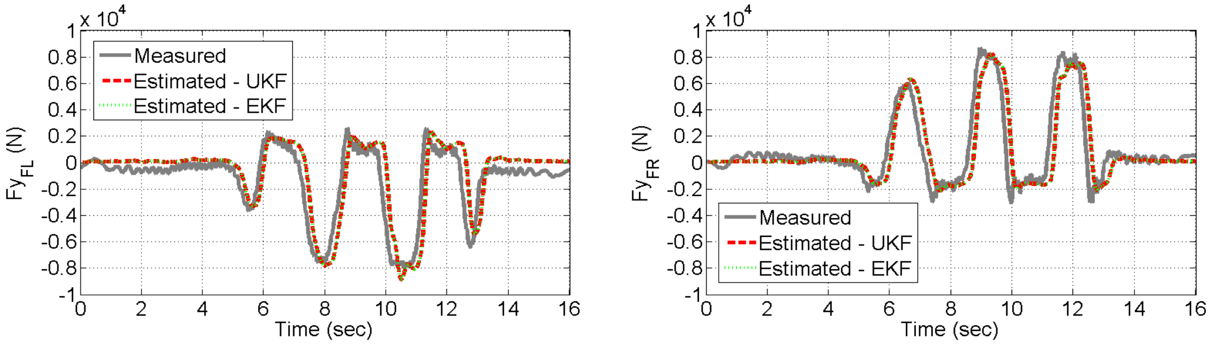

(a) Front-left tire (b) Front-right tire

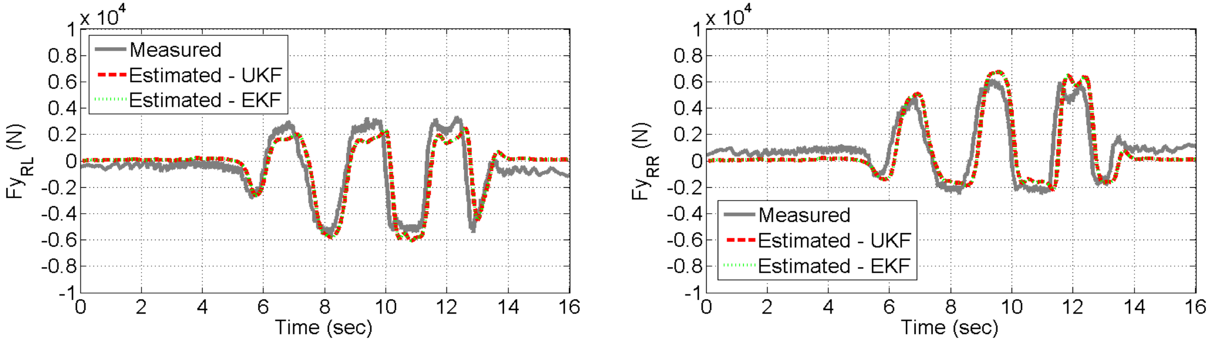

(c) Rear-left tire (d) Rear-right tire

Figure 5.18. Estimation results for lateral tire force using UKF.

5.4.2.2 Double lane change (DLC) test

The DLC is another common maneuver, performed at a constant speed that mostly excites the lateral vehicle dynamics. Figure 5.19 shows wheel torques, steering wheel angle, and vehicle longitudinal and lateral acceleration during this maneuver. The double lane change maneuver is performed with a constant velocity ($\approx 50\ \mathrm{km/hr}$). In Figure 5.19, the test vehicle is highly excited in both longitudinal and lateral directions ($-3.91 \leq a_{x,m} \leq 4.60\ \mathrm{m\ s^{-2}}$ and $-5.92 \leq a_{y,m} \leq 6.64\ \mathrm{m\ s^{-2}}$).

a) Identification of vehicle mass

Figure 5.20 shows the identified vehicle mass in this maneuver. The error between the identified vehicle mass and actual mass is 0.68%. The vehicle mass is identified in less than 4 seconds.

b) Estimation of longitudinal tire forces

Figure 5.21 depicts the measured and estimated longitudinal tire forces for the four wheels. The measured results demonstrate the accurate performance of the longitudinal force estimation. Table 5.8 shows that NRMS errors are between 5.36% and 6.22% for all wheels.

c) Estimation of vertical tire forces

In the DLC maneuver, between time 7 sec and 12.5 sec, a lateral load transfer is observed (Figure 5.22). The estimated vertical forces are presenting by dashed lines in Figure 5.22. The calculated forces have good agreement with the measured ones. All NRMS errors for four wheels are less than 6.68% (Table 5.9). In the first part of the maneuver, because of the longitudinal load transfer to the back of the vehicle and errors in the identified vehicle mass, there are errors between the estimated forces and measured forces acting on the rear wheels.

d) Estimation of lateral tire forces

Figure 5.23 compares the estimated and measured lateral tire forces. Similar to the previous discussion for the slalom maneuver, UKF and EKF have comparable performances during the DLC maneuver.

Table 5.10 shows that the maximum forces acting on the four wheels and the NRMS errors of the UKF estimator presented in Chapter 3. The NRMS errors for all wheels are between 5.47% and 18.29%. The time delay between the estimated forces and measured ones in Figure 5.23 are due to the low-pass filtering of the sensory data. The biggest NRMSE is that of the rear-right wheel especially when the vehicle is moving in a straight line. The main reason is the effect of un-modelled camber angle.

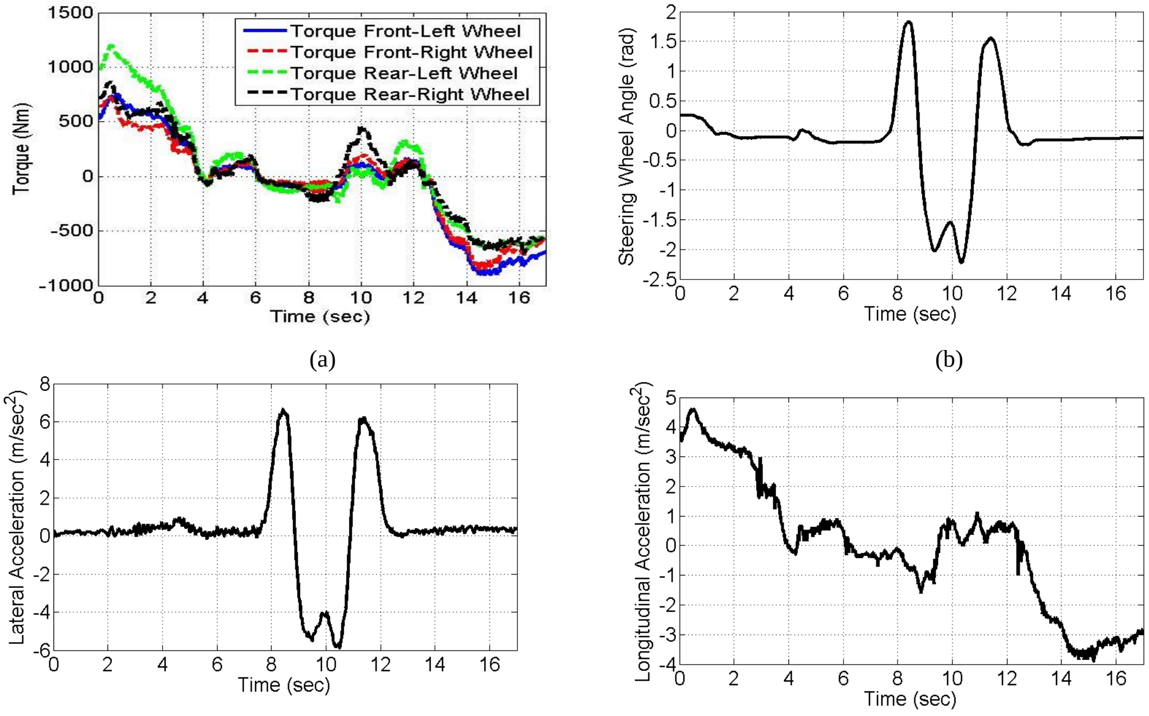

(a) (b)

(c) (d)

Figure 5.19. DLC maneuver: (a) Torques acting on each wheel, (b) Steering wheel angle, (c) Lateral acceleration, (d) Longitudinal acceleration

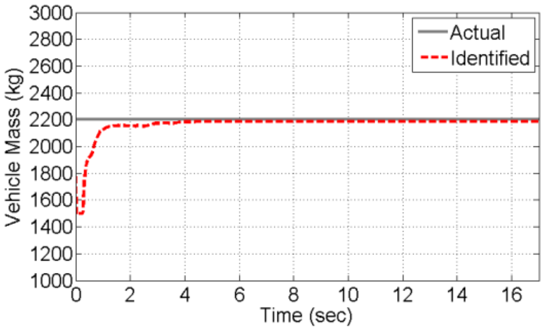

Figure 5.20. Comparison between the actual vehicle mass and identified mass.

Table 5.8. NRMS errors and maximum longitudinal forces acting on four wheels

	$F_{x_{fl}}$	$F_{x_{fr}}$	$F_{x_{rl}}$	$F_{x_{rr}}$
$Max\ \lvert . \rvert\ (N)$	2547.9	2713.6	3680.9	2295.1
$NRMS\ (\%)$	5.63	5.36	6.02	6.22

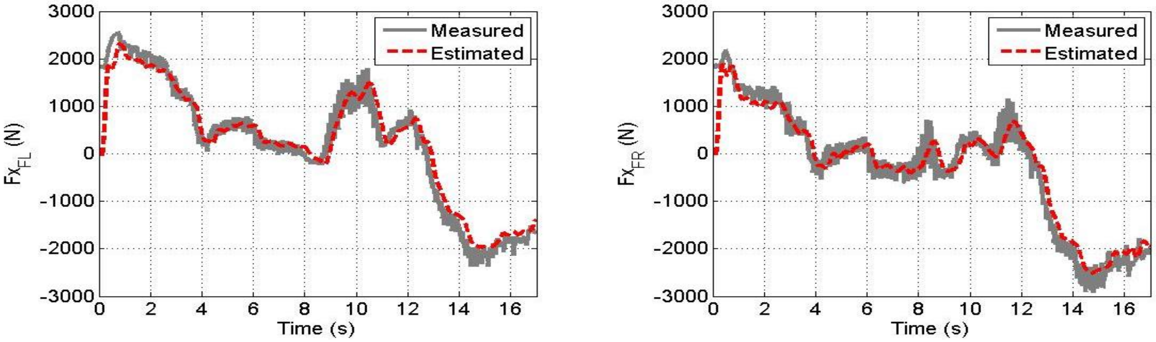

(a) Front-left tire (b) Front-right tire

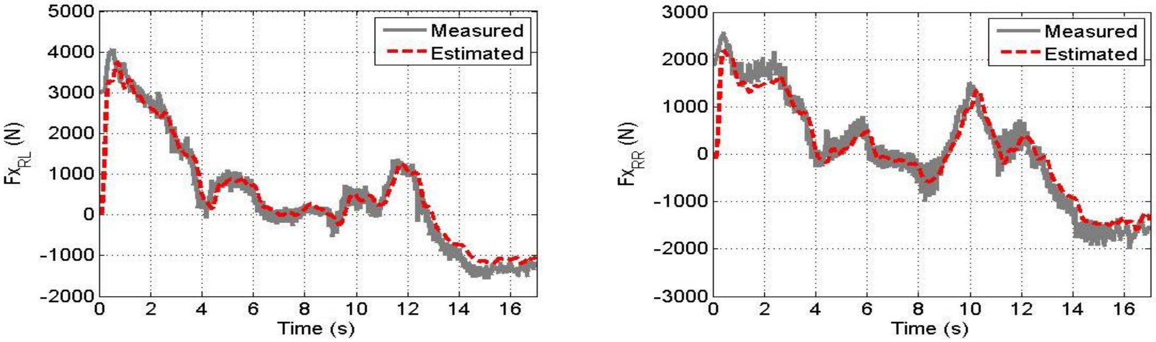

(c) Rear-left tire (d) Rear-right tire

Figure 5.21. Estimation results for longitudinal tire forces.

Table 5.9. NRMS errors and maximum normal forces acting on three wheels

	$F_{z_{fl}}$	$F_{z_{fr}}$	$F_{z_{rl}}$	$F_{z_{rr}}$
$Max\ \lvert . \rvert\ (N)$	9107.4	9482.9	6858.6	7336.4
$NRMS\ (\%)$	5.21	4.66	5.89	6.68

Table 5.10. NRMS errors and maximum lateral forces acting on wheels

	$F_{y_{fl}}$	$F_{y_{fr}}$	$F_{y_{rl}}$	$\mathrm{F}_{\mathrm{y}_{\mathrm{rr}}}$
$Max\ \lvert . \rvert\ (N)$	5835.5	5715.2	3574	4855.8
$NRMS\ (\%)$	5.47	5.93	14.47	18.29

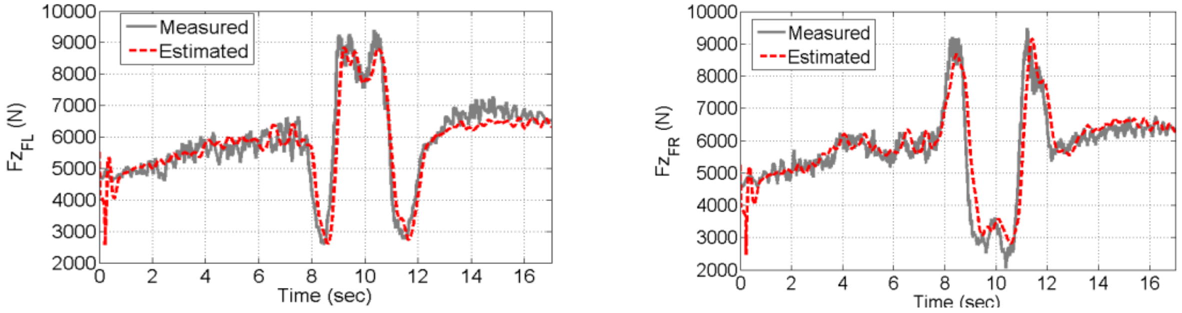

(a) Front-left tire (b) Front-right tire

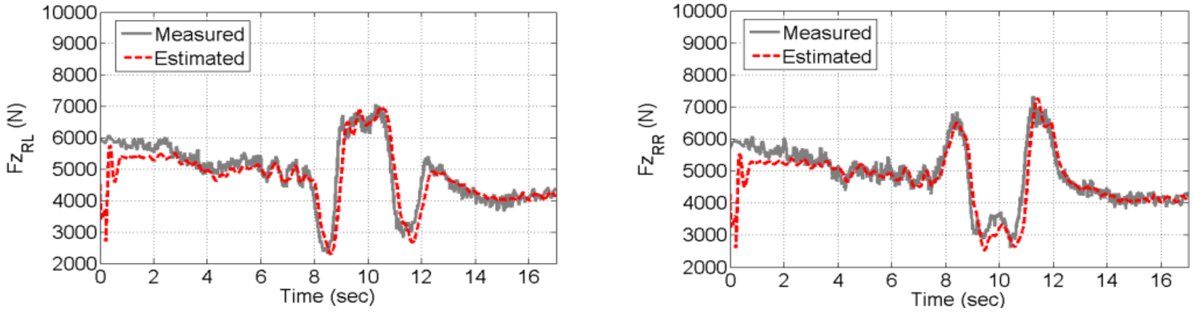

(c) Rear-left tire (d) Rear-right tire

Figure 5.22. Estimation results for vertical tire forces

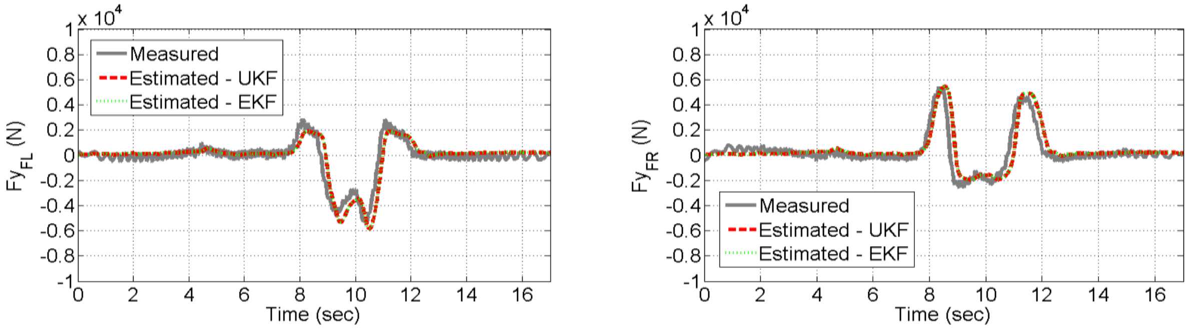

(a) Front-left tire

(b) Front-right tire

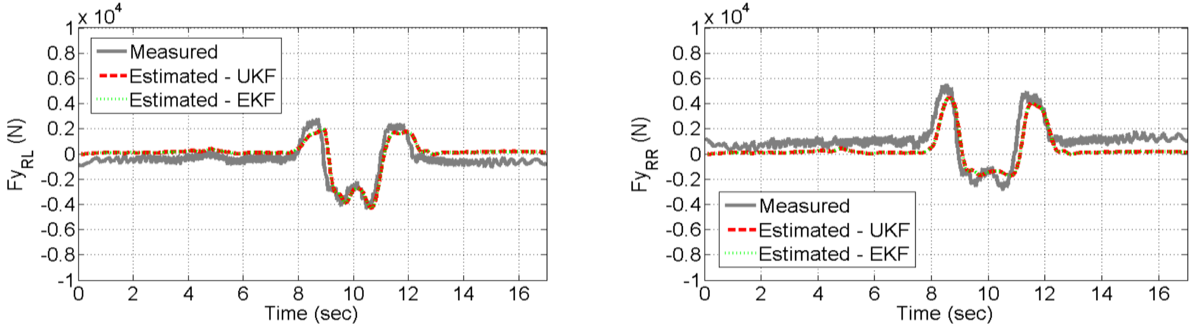

(c) Rear-left tire (d) Rear-right tire

Figure 5.23. Estimation results for lateral tire force using UKF.

5.4.2.3 Slalom maneuver on a slippery road and higher vehicle mass

In this section the vehicle is tested on a slippery road. The vehicle is moving in the straight line and then a sine wave steering angle is applied in a constant velocity (≈25 km/hr). Figure 5.24 shows the vehicle accelerations, wheel torques and steering wheel angle in this maneuver. Additionally, in this test, more weight (200 kg) has been added to the vehicle. Figure 5.25 shows that the mass identification algorithm is robust against changes in the road conditions. The mass identification algorithm can identify the vehicle mass with 2.54% error. Figure 5.26 shows a comparison between the estimated longitudinal forces and the measured forces. In addition, Table 5.11 shows the NRMS errors and maximum forces applied to each wheel in the longitudinal direction.

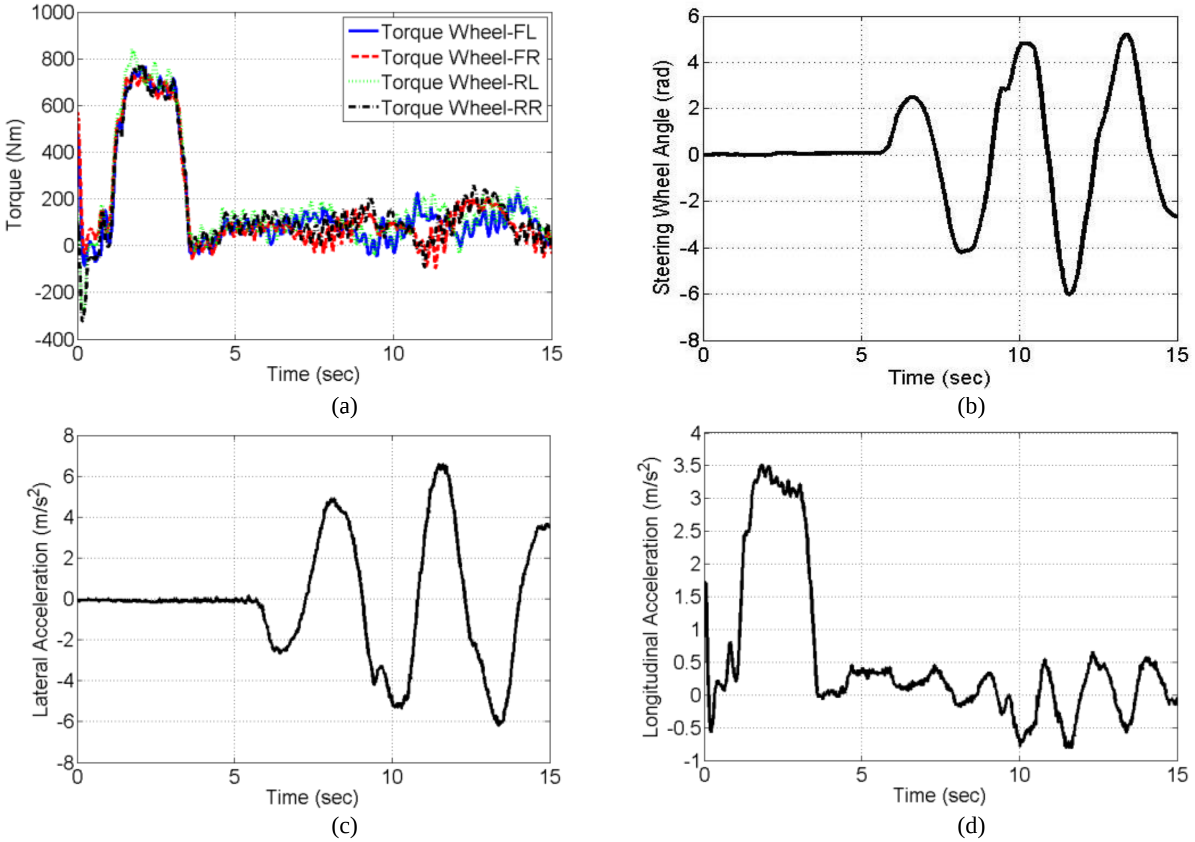

(a) (b)

(c) (d)

Figure 5.24. Slalom maneuver: (a) Torques acting on each wheel, (b) Steering wheel angle, (c) Lateral acceleration, (d) Longitudinal acceleration

The results for estimation of vertical forces are shown in Figure 5.27. The algorithm can reliably estimate the vertical forces with NRMS errors less than 4.28%. The errors in the identified vehicle mass in the first part of the maneuver mainly contribute to the vertical tire force estimation errors. Figure 5.28 demonstrates the performance of the lateral force estimation algorithm on the slippery road. The vehicle is not moving before time 1.16 s, and there are errors between the measured and estimated forces during that time. These errors have different signs for left and right wheels because of the camber angle effect. However, after the vehicle moves, the measured lateral forces is close to zero because the vehicle is not excited in lateral direction until $t = 6$ s. Same as the previous tests, UKF and EKF have comparable performances. NRMS errors for all wheels are less than 13.46% (Table 5.13).

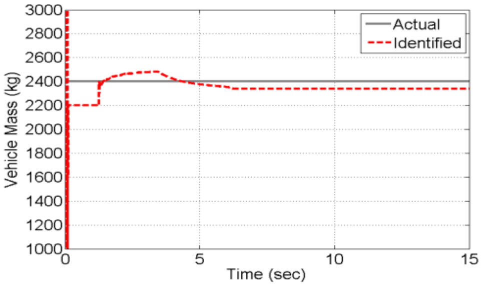

Figure 5.25. Comparison between the actual vehicle mass and identified mass

Table 5.11. NRMS errors and maximum longitudinal forces acting on four wheels

	$F_{x_{fl}}$	$F_{x_{fr}}$	$F_{x_{rl}}$	$F_{x_{rr}}$
$Max\ \lvert.\rvert\ (N)$	2471	2189	2561	2285
$NRMS\ (\%)$	6.23	6.39	5.87	7.04

Table 5.12. NRMS errors and maximum normal forces acting on three wheels

	$F_{z_{fl}}$	$F_{z_{fr}}$	$F_{z_{rl}}$	$F_{z_{rr}}$
$Max\ \lvert.\rvert\ (N)$	9058	9557	8399	8589
$NRMS\ (\%)$	1.78	2.34	3.61	4.28

Table 5.13. NRMS errors and maximum lateral forces acting on three wheels

	$F_{y_{fl}}$	$F_{y_{fr}}$	$F_{y_{rl}}$	$F_{y_{rr}}$
$Max\ \lvert.\rvert\ (N)$	6907	7647	4580	5114
$NRMS\ (\%)$	9.74	8.91	13.46	9.20

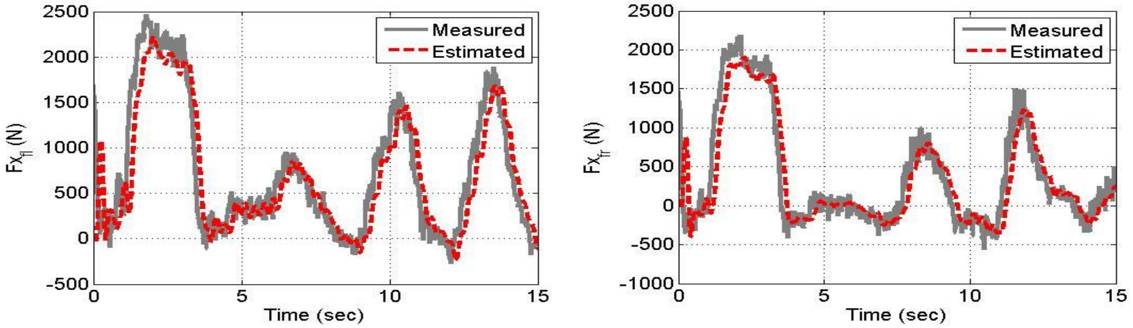

(a) Front-left tire (b) Front-right tire

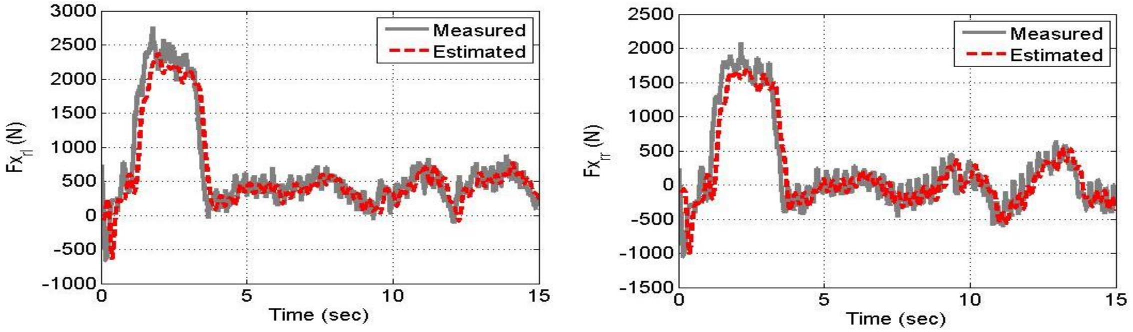

(c) Rear-left tire (d) Rear-right tire

Figure 5.26. Estimation results for longitudinal tire forces

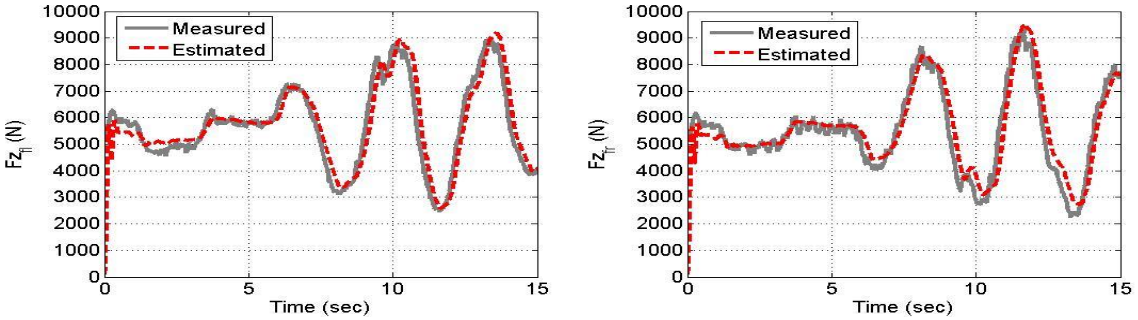

(a) Front-left tire (b) Front-right tire

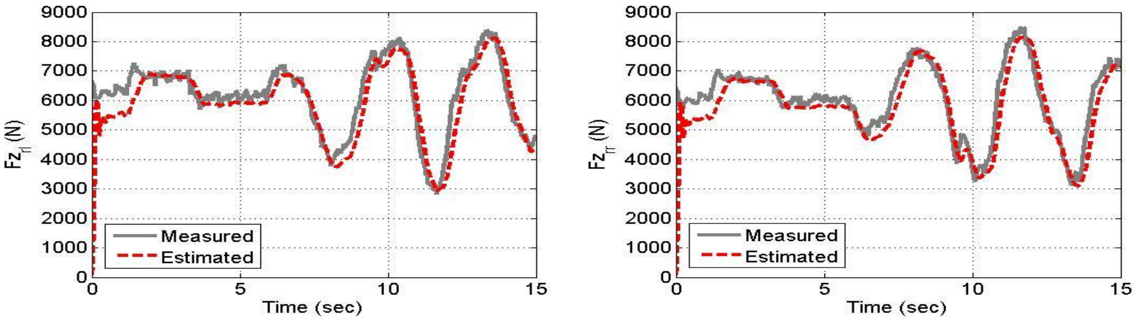

(c) Rear-left tire (d) Rear-right tire

Figure 5.27. Estimation results for vertical tire forces

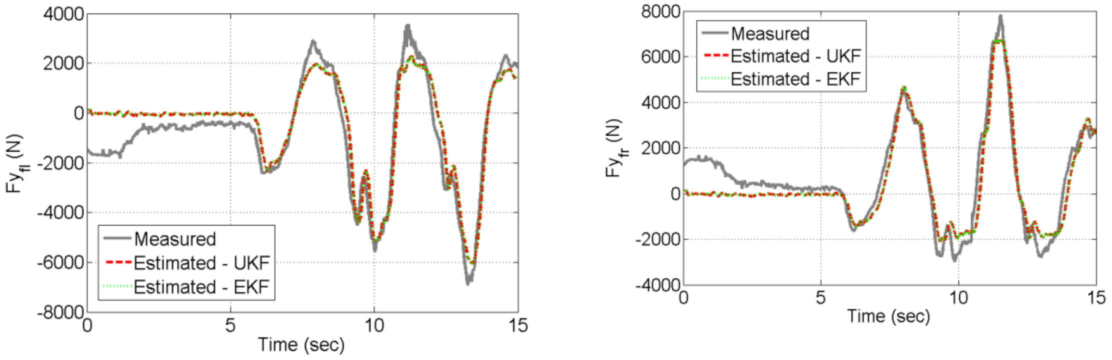

(a) Front-left tire

(b) Front-right tire

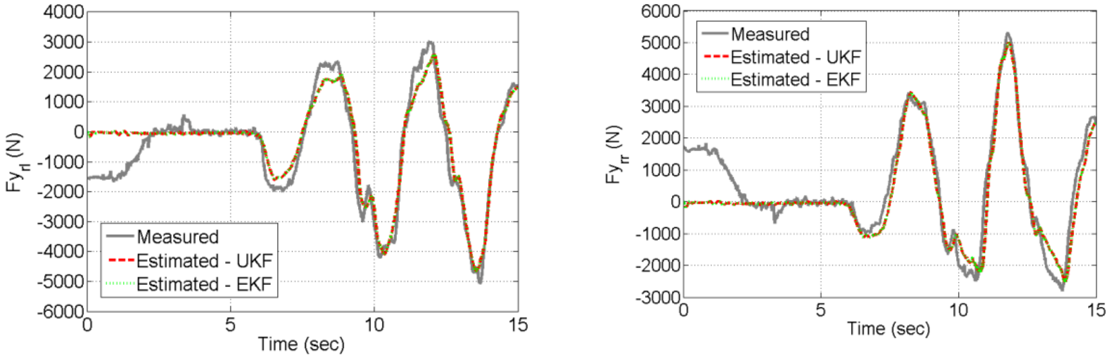

(c) Rear-left tire

(d) Rear-right tire

Figure 5.28. Estimation results for lateral tire force using EKF and UKF.

5.4.3 Velocity estimation algorithm

In this section, the performance of the proposed velocity estimation algorithm is investigated. In addition, the estimated longitudinal velocity is compared with the output of the proposed approach in [39] which uses the motor torque on each wheel to detect excessive slippage. In this thesis, the proposed estimation algorithm does not use any torque information. However, the algorithm proposed in [39] needs the braking torque acting on each wheel for the braking maneuvers. Even in electric vehicles, the conventional friction braking system is also used as the back-up in conjunction with the regenerative braking system. An accurate calculation of the braking torques in all driving conditions is not an easy task. In the conventional friction-based braking system, magnitude of braking torques can be affected by many factors such as humidity between rotor and braking pads.

5.4.3.1 Slalom maneuver

Figure 5.29 shows the longitudinal and lateral acceleration of vehicle body, wheel steering angle, and wheel torques acting on the four wheels in this maneuver. The vehicle is moving at the constant velocity of ≈32 km/h during time 12 sec to 23.7 sec and in this time window the slalom maneuver is performed. In this time window, the vehicle is highly excited in the lateral direction and the range of lateral acceleration is $-9.75(\mathrm{m\,s^{-2}}) \leq a_{y,m} \leq 9.84\ \mathrm{m\,s^{-2}}$. Finally, the friction brakes are applied, especially on the front wheels, to stop the vehicle at time 25 sec. It is noted that the driving torques of all four wheels are the same during the traction in the first part of the maneuver and slalom maneuver.

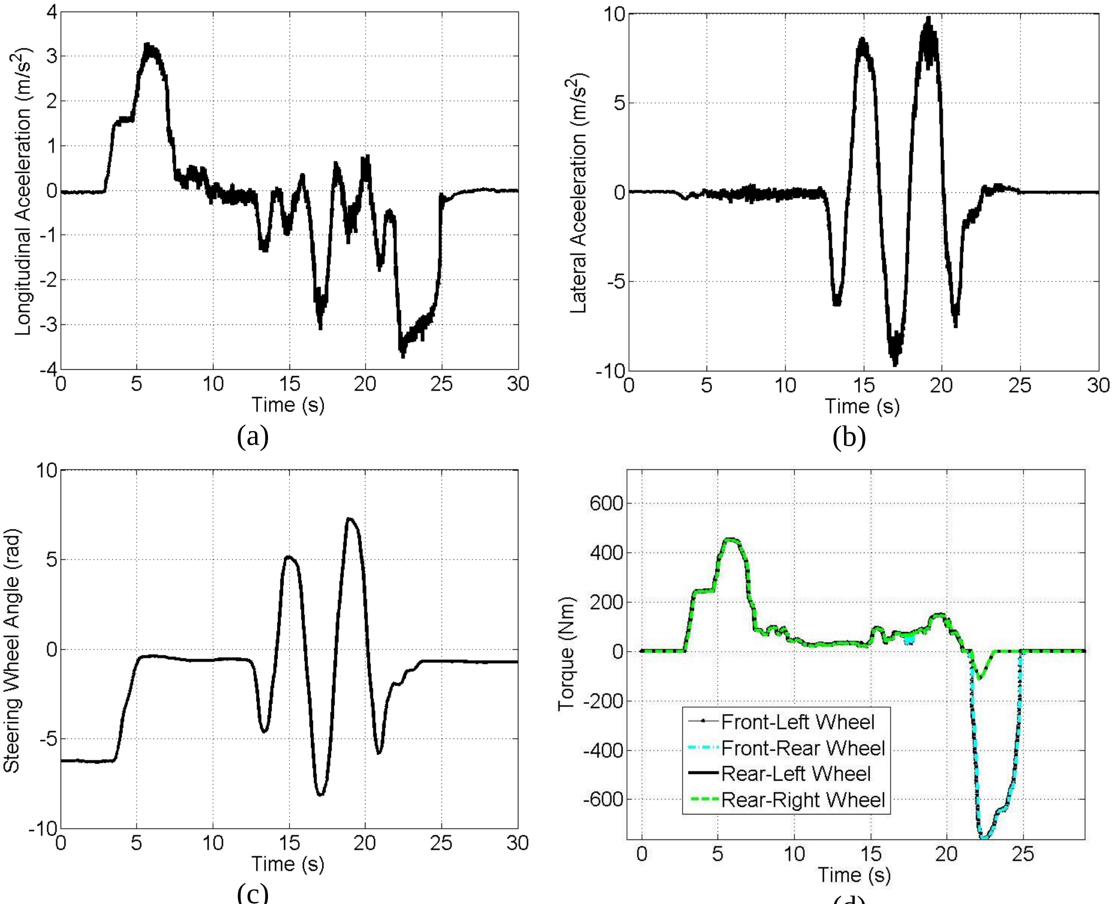

(a) (b)

(c) (d)

Figure 5.29. Salaom maneuver: (a) longitudinal acceleration, (b) lateral acceleration, (c) steering wheel angle, (d) torque acting on each wheel.

Figure 5.30 (a) depicts the wheels speeds, which are varying during the lateral excitation. Figure 5.30 (b) shows the comparison between estimated and measured longitudinal velocity of the vehicle and the estimated longitudinal velocity according to the approach in [39]. The results in this figure clearly show that the performance of the proposed estimation algorithm and the longitudinal velocity estimation algorithm in [39] are comparable. The estimated velocity does not have any drift and the NRMS error between the estimated signal and the measured one is 0.74%.

Figure 5.31 (a) shows the estimated lateral velocity of the vehicle and measured lateral velocity of the GPS. The NRMS error between the estimated velocity and the measured one is 6.29%. To evaluate the performance of the proposed velocity estimation structure and bias effect, the estimated lateral velocity is compared with calculated velocity using pure integration of (3-61). The latter is depicted in Figure 5.31(b).

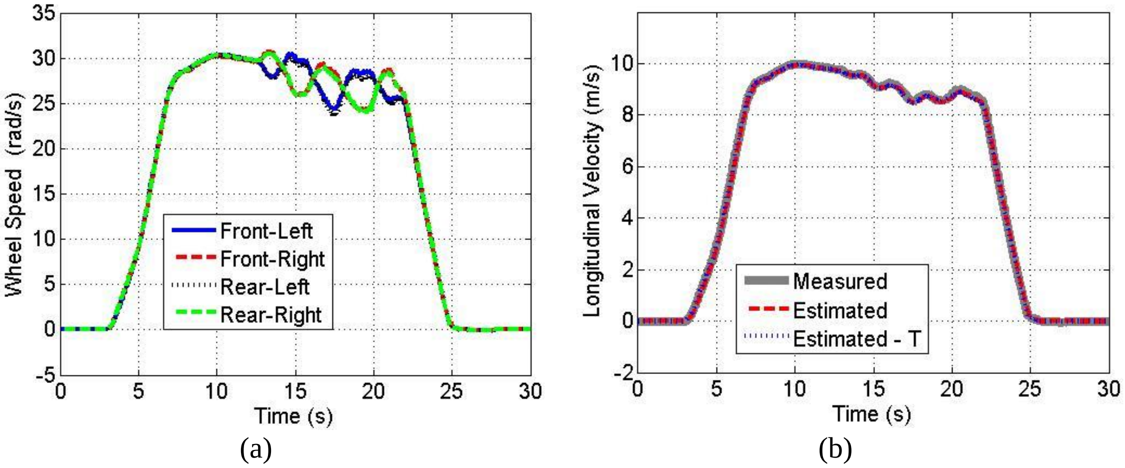

Figure 5.30. (a) Wheels' speeds, (b) comparison between measured vehicle longitudinal velocity (using GPS) and estimated velocity.

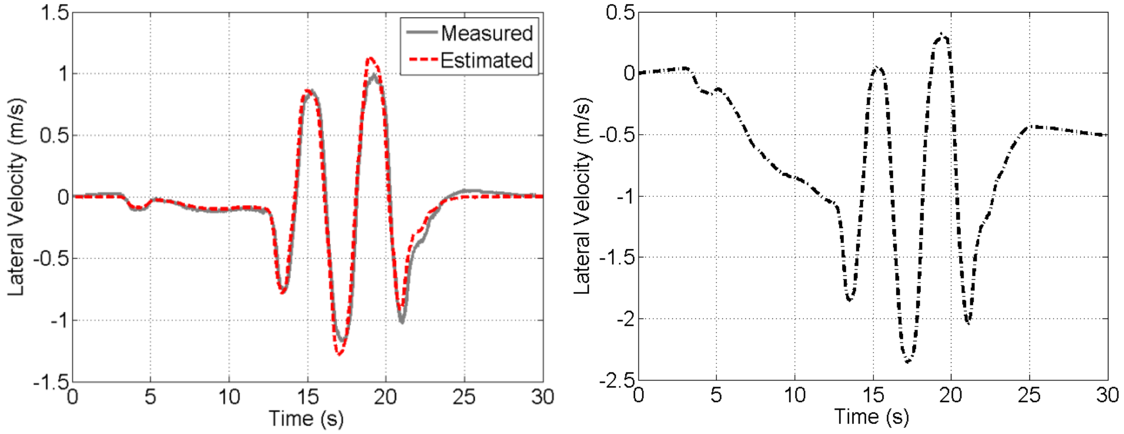

(a) (b)

Figure 5.31. (a) Comparison between estimated vehicle lateral velocity and measured lateral velocity by GPS, (b) calculated vehicle lateral velocity using integration.

The comparison between the estimated lateral velocity (Figure 5.31 (a)) and calculated velocity based on pure integration (Figure 5.31 (b)) illustrates that the proposed estimation algorithm in Chapter 3 significantly removes the drift in the estimation. Figure 5.31 (b) shows that the drift appears in this maneuver when the vehicle is not excited in the lateral direction or changes in lateral direction are not fast.

5.4.3.2 Slalom maneuver on a slippery road

This test is performed on a slippery road ($\mu \approx 0.4$). A sine wave steering angle is applied at a constant velocity 43 (km h^{-1}). After 10 (s), the friction brakes are applied to stop the vehicle. Figure 5.32 shows the vehicle accelerations, steering wheel angle and torques applied on each wheel by the in-wheel motors in the Opel.

Figure 5.33 (a) shows that the right and left wheels have different speeds because of the applied steering angle. After 10 (s), the front wheels are locked because the brake system is applied to lock the wheels and control the vehicle. Figure 5.33 (b) shows that the performances of the proposed longitudinal velocity estimation algorithm in this thesis and the approach in [39] are comparable. Additionally, it shows the performance of the longitudinal velocity estimation algorithm when the vehicle is moving on the slippery surface. It shows that the estimation algorithm does not use the speed information of the front wheels especially when these wheels are slipping and their speeds are zero. Additionally, there is no fluctuation or drift in the estimated velocity. The NRMS errors between the estimated signals and the measured ones are 7.43%. Figure 5.34(a) shows a comparison between calculated and estimated lateral velocities. The NRMS errors between the estimated signals and the measured ones are 8.34%. After time 11.51 (s), there is drift in the calculated velocity using integration because slower changes in the lateral dynamics after time 11.51 (s) until the end of the maneuver.

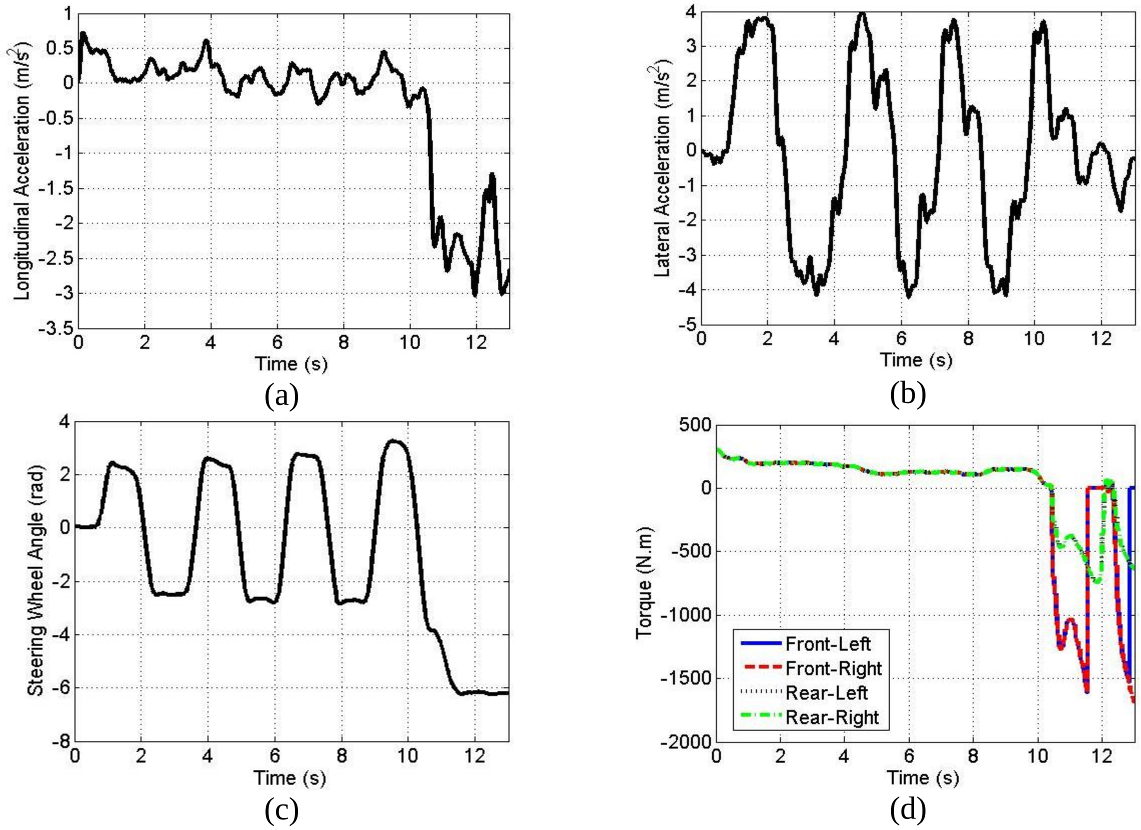

Figure 5.32. (a) Longitudinal acceleration, (b) lateral acceleration, (c) steering wheel angle, (d) torque acting on each wheel.

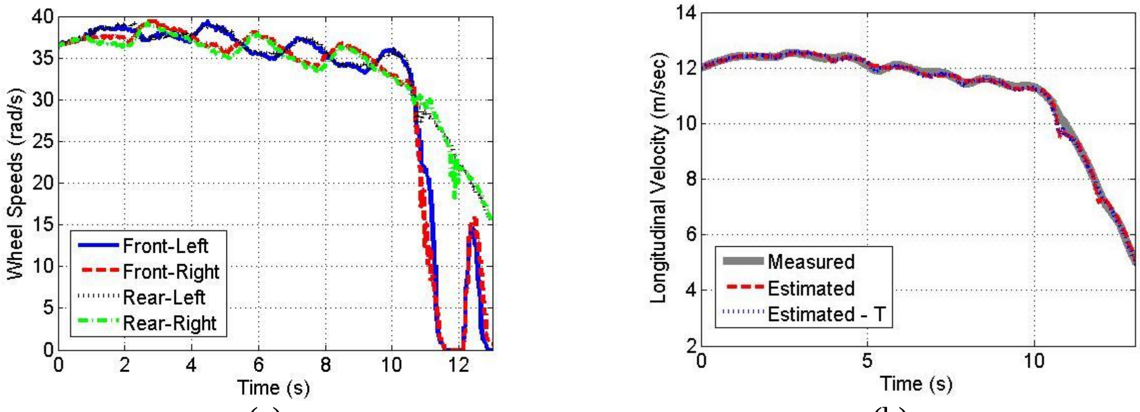

(a) (b)

Figure 5.33. (a) Wheels' speeds. After 10 (s), front wheels are locked by the brake system. (b) comparison between measured vehicle longitudinal velocity (using GPS) and estimated velocity.

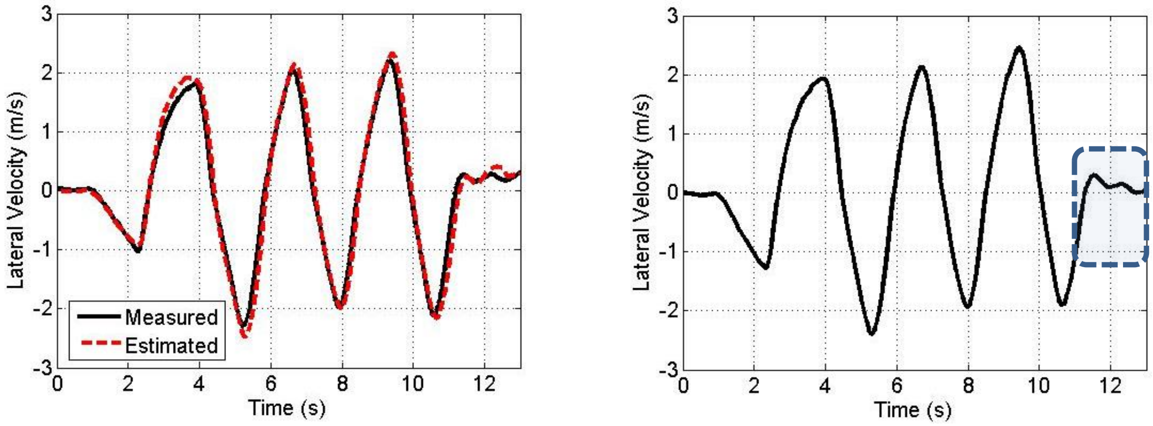

(a) (b)

Figure 5.34. (a) Comparison between estimated vehicle lateral velocity and measured lateral velocity by GPS, (b) calculated vehicle lateral velocity using integration.

5.4.3.3 Launch maneuver on an icy road

In this maneuver, the road surface is icy and $\mu \approx 0.1$. The test vehicle starts moving from zero velocity, and reaches a final speed of 25 (km h^{-1}). Figure 5.35 shows the measured longitudinal and lateral accelerations, wheel torques and steering wheel angle. During this test, the traction control was off. In less than 1 second traction torques suddenly increase, and after that it start decreasing in less than 2 seconds (see Figure 5.35(d)). According to Figure 5.36 (a), all four wheels are slipping during time 1.55 (sec) to 8.38 (sec). After this time window, the wheels return to normal rotation without high slip.

These slippages are detected using the slip detection block presented in Figure 3.8. Therefore, the wheels speeds are not used in the longitudinal velocity estimation algorithm during the abovementioned period of time. Figure 5.36 (b) shows a comparison between the estimated and measured longitudinal velocity of the vehicle. The absolute error between measured and estimated velocity in this period of time is less than 0.2 (m s^{-1}). And, NRMS errors between the estimated signals and the measured ones are 1.95%. The results in Figure 5.36(b) indicate that the performance of the proposed algorithm in Section 2 and that in [39] are comparable in the launch maneuverer on the icy road with all four wheels excessively slipping.

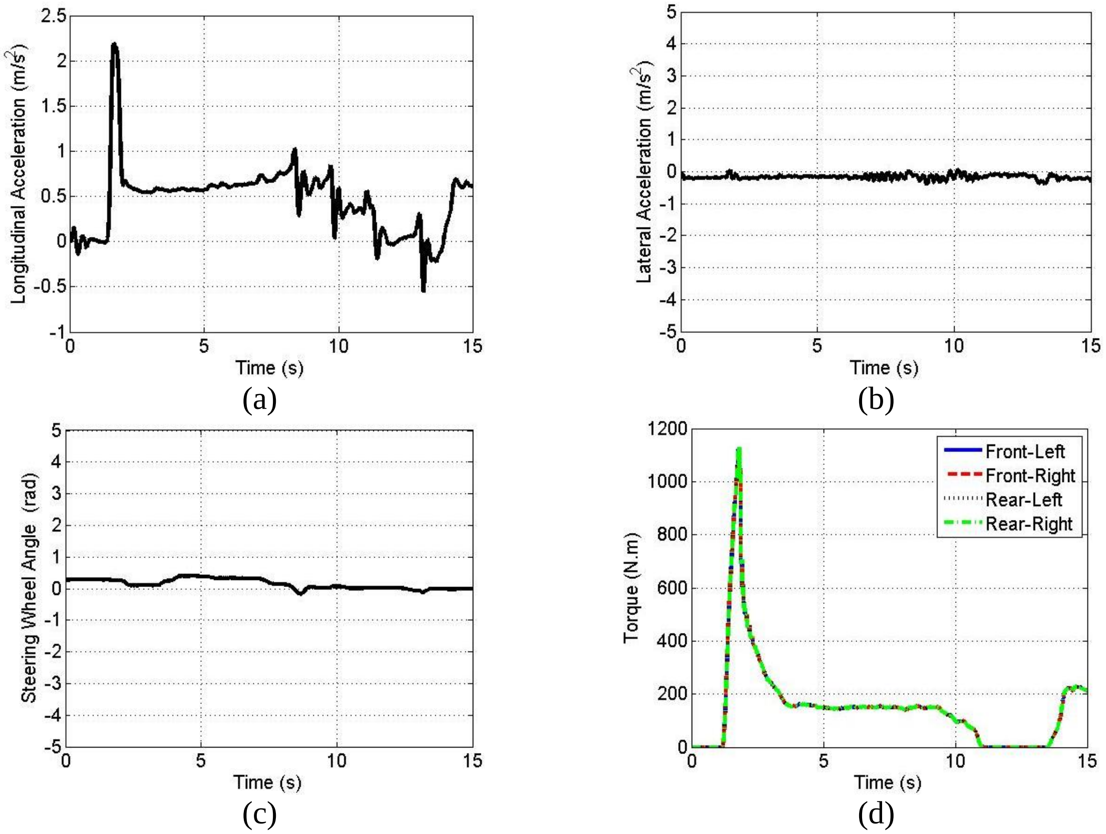

(a) (b)

(c) (d)

Figure 5.35. (a) Longitudinal acceleration, (b) lateral acceleration, (c) steering wheel angle, (d) torque acting on each wheel.

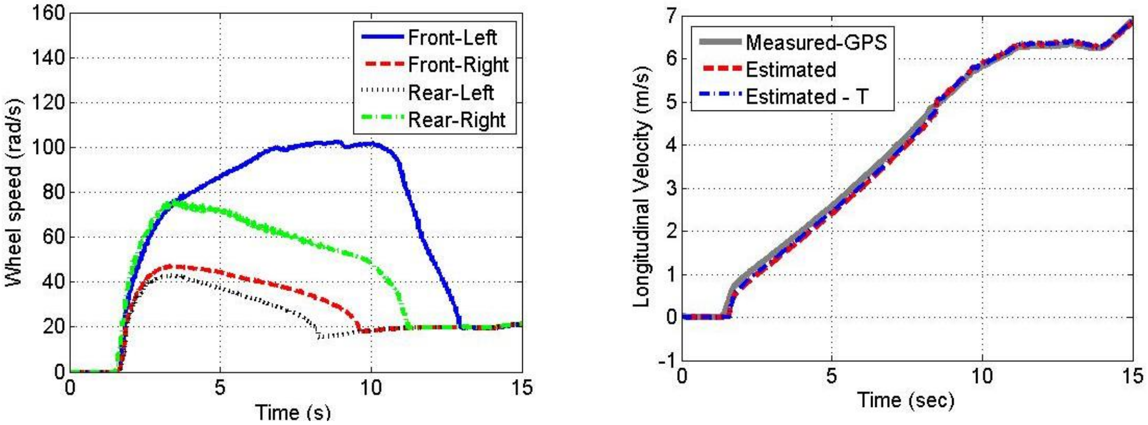

(a) (b)

Figure 5.36. (a) Wheels' speeds. Four wheels are slipping during acceleration. (b) Comparison between measured vehicle longitudinal velocity (using GPS) and estimated velocity.

Figure 5.37 (a) shows the estimated lateral velocity which is close to zero, because the vehicle is moving in a straight line. There is no drift in the estimated velocity. Minor differences between the measured lateral velocity using the GPS and the estimated one are less than 0.05 (m s^{-1}). Figure 5.37 (b) shows the calculated lateral velocity using numerical integration. This figure clearly shows the drift because of noise in measured signals and bias in the measured lateral acceleration signal, which is -0.18(m s^{-2}).

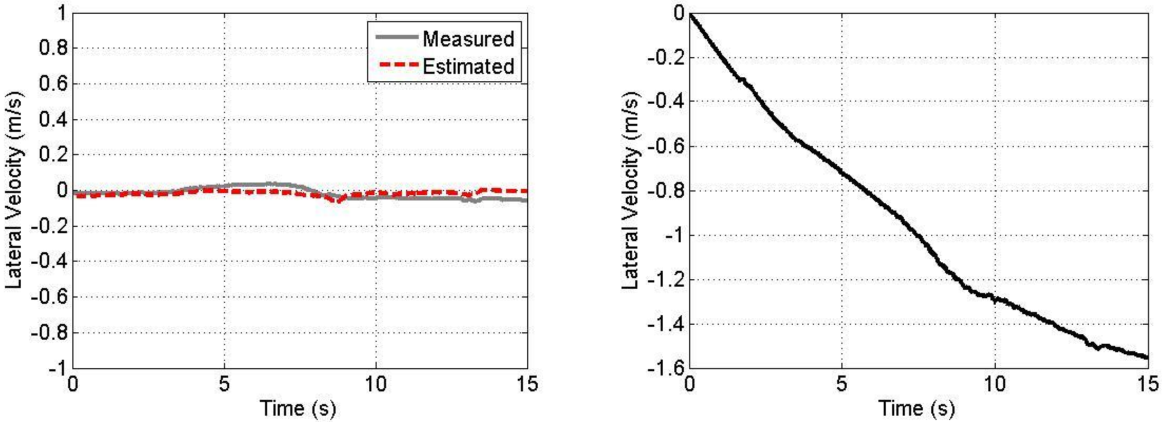

(a) (b)

Figure 5.37. (a) Comparison between estimated vehicle lateral velocity and measured lateral velocity by GPS, (b) calculated vehicle lateral velocity using integration.

5.4.4 Road bank and grade identification algorithms

In this section, two scenarios will be discussed to demonstrate the performance of road bank and grade angle identification algorithms. These scenarios are on a banked road and an inclined road, respectively.

Because the vehicle has not been equipped with a device to measure the road angle, it is not possible to compare the identified angles with the measurements. Therefore, for comparison purposes the equations below are used as the calculated road angles in the regions when the vehicle is moving on the constant road angle [5]:

$$\phi_{r,cal} = \sin^{-1}\left(\frac{a_{y,m} - \dot{v}_{y,m} - \dot{\psi}_m v_{x,m}}{g}\right) - \phi_{v,m} \tag{5-11}$$

$$\theta_{r,cal} = \sin^{-1}\left(\frac{a_{x,m} - \dot{v}_{x,m} + \dot{\psi}_m v_{y,m}}{g}\right) - \theta_{v,m} \tag{5-12}$$

The lateral and longitudinal accelerations $\dot{v}_{y,m}$ and $\dot{v}_{x,m}$ are calculated from the measured lateral velocity and longitudinal velocity, respectively. It is noted to mention that the outputs of above equations are filtered with a first order low-pass filter.

5.4.4.1 Test on banked road

In the first part of this test, the vehicle is approximately on a flat road. Then, the vehicle starts moving on the banked road. Also, there is a transition part between flat road and banked road that has both bank and grade angles.

Figure 5.38 shows the measured longitudinal and lateral acceleration, steering wheel angle, vehicle speed and location of the vehicle for this test. According to Figure 5.38 (e), the vehicle is moving in straight line and then it enters into a road section that looks like a bowel with the bank angle. The road is similar to highway exit ramps. The vehicle speed is between 0 m/s to 10.5 m/s, longitudinal acceleration is between 0 m/s^2 to 3 m/s^2, and lateral acceleration is between 2.5 m/s^2 and -1.5 m/s^2.

Figure 5.39 (a) shows the comparison between the identified bank angle, calculated bank angle with (5-11) and the reference angle based on the available GM literature . According to Figure 5.39 (a), the identified bank angle is following the reference signal. In the first part of the maneuver, the road has a small bank angle close to 1.5 deg, and after the transition part (from 4.5 s to 6.5 s), the road bank angle increases to approximately 15 deg.

Figure 5.39 (b) shows the identified road grade and the calculated angle with (5-12). The identified road grade before and after the transition part is smaller than one degree. However, during the transition part, the road grade increases and then decreases. This happens because the vehicle is moving up from a flat horizontal surface to the large bank angle.

5.4.4.2 Test on uphill

In this test, the vehicle is moving on an uphill in a straight line. The grade angle of this road is close to 16% which is 9.09 deg. As shown in Figure 5.40, the vehicle is accelerated form 4.4 m/s to the constant speed close to 5.5 m/s. The lateral acceleration is constant and close to -0.3 m/s^2. Figure 5.40 shows the complete path that the vehicle is driven on.

Figure 5.41 shows the identified bank and grade angles. Figure 5.41 (a) shows that the identified bank angle is following the calculated signal based on (5-12). The identified bank angle is between -0.5 deg to 2 deg. The delay at the first part of the identification process is because of the low-pass filter used for the static bank angle calculation as explained in Section 4.1.4 of Chapter 4.

Figure 5.41 (b) shows the identified road grade and the reference angle reproduced from existing GM literature . The identified road grade closely matches the reference values. The constant road grade is identified in 1.2 s.

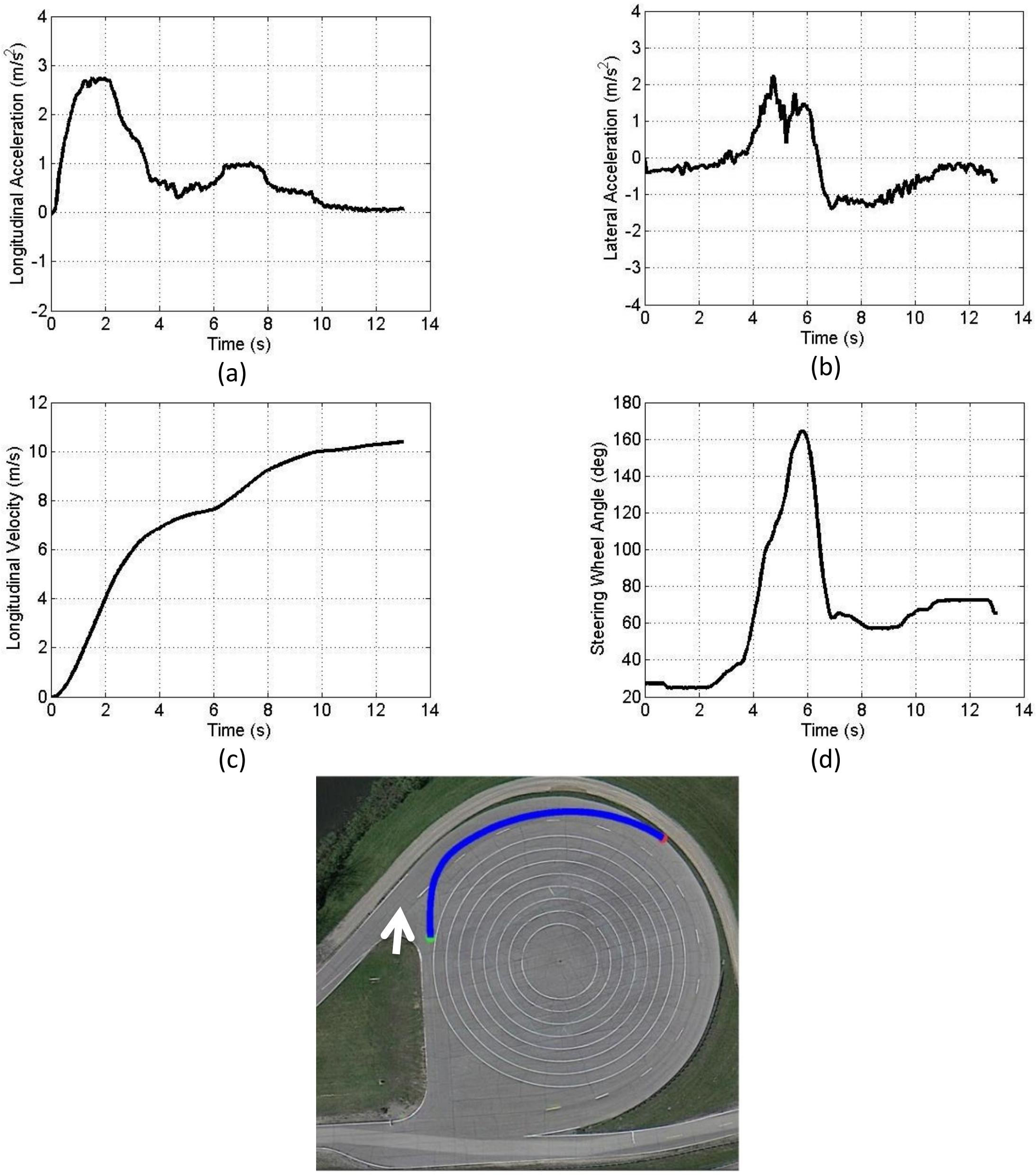

Figure 5.38. Banked road test (a) longitudinal acceleration, (b) lateral acceleration, (c) vehicle speed, (d) wheel steering angle, (e) path driven by vehicle during maneuver

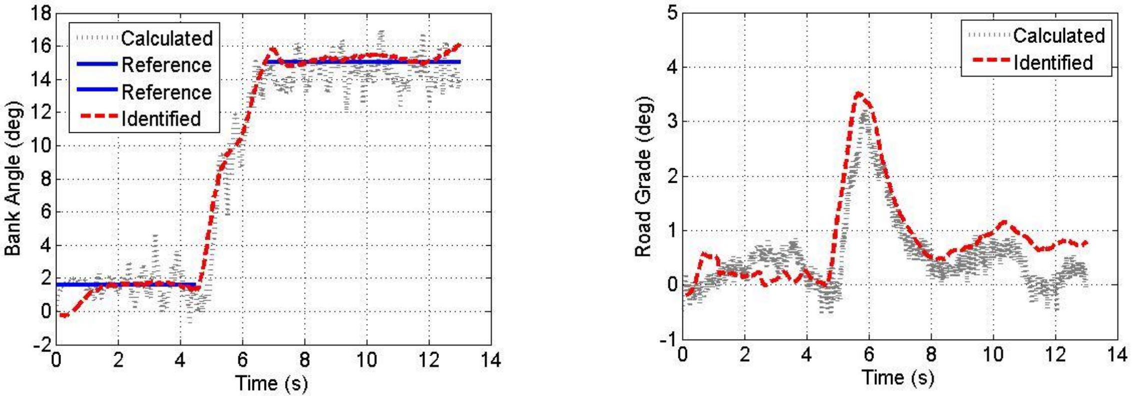

(a) (b)

Figure 5.39. Identified road angles: (a) identified bank angle, (b) identified road grade

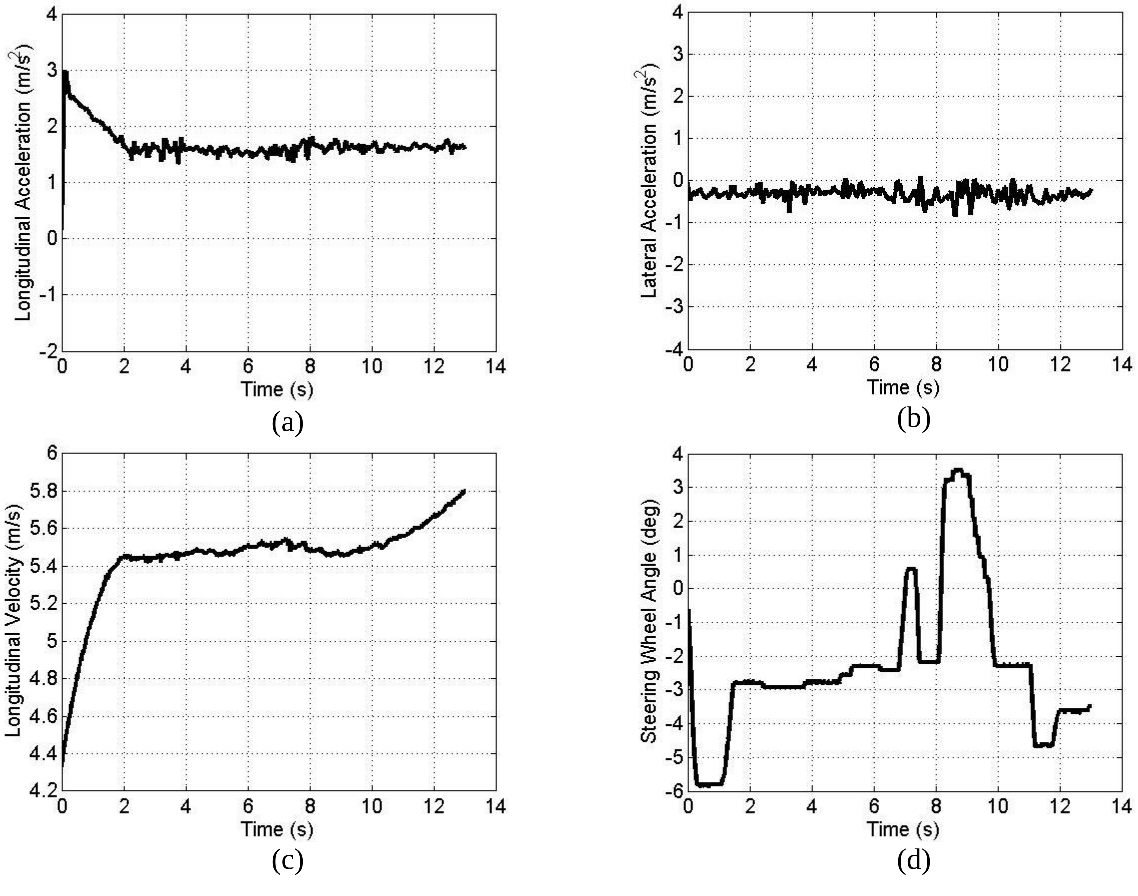

(a) (b)

(c) (d)

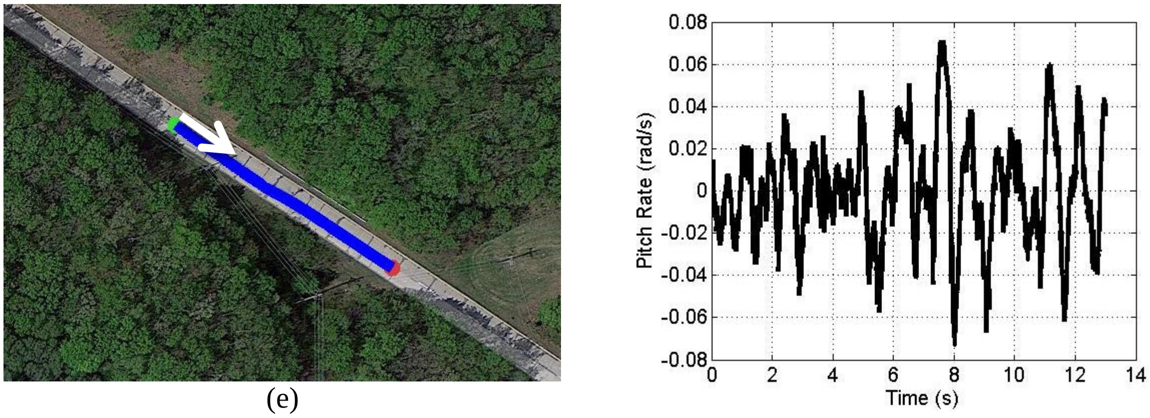

(e) (f)

Figure 5.40. Uphill test: (a) longitudinal acceleration, (b) lateral acceleration, (c) vehicle speed, (d) wheel steering angle, (e) path driven by vehicle during maneuver, (f) pitch rate

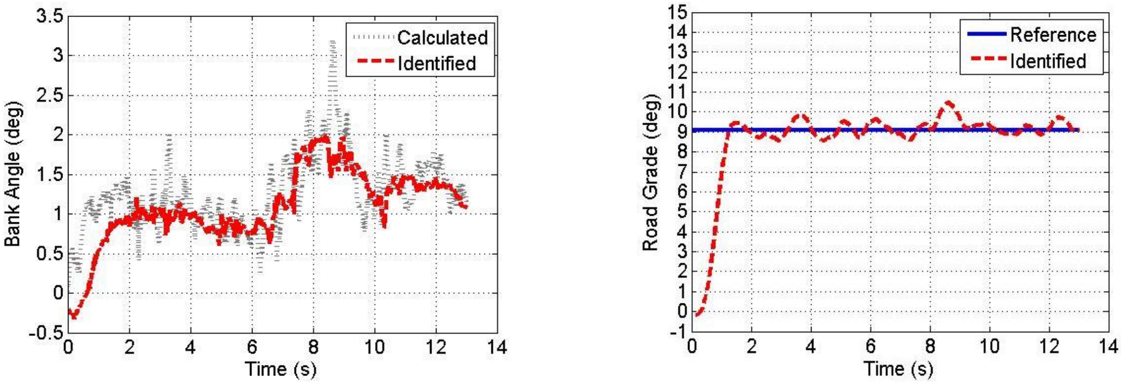

(a) (b)

Figure 5.41. Identified road angles: (a) identified bank angle, (b) identified road grade

5.4.4.3 Effect of road angles on the velocity estimation algorithm

Road angles are inputs to the proposed velocity estimation algorithm in Chapter 3. Hence, in this section we investigate the effect of these angles on the estimated longitudinal and lateral velocities.

Banked road test

Figure 5.42 shows the performance of the velocity estimation algorithm on the banked road. According to Figure 5.42 (a), the estimated velocity without use of information about the actual bank angle diverges and does not provide accurate estimation. The measured lateral velocity with the GPS has a drift and is not accurate. Therefore, the measured lateral velocity by means of an optical sensor is used to verify the estimation algorithm performance. The estimated lateral velocity is following the measured signal from the optical sensor with no visible drift. Figure 5.42(b) shows the performance of the estimation algorithm with and without utilization of road grade identification. The estimated longitudinal velocities in these two conditions are the same, because the estimation algorithm is using the measured wheel speeds to correct the errors in the prediction step of Kalman filter (see Section 2.3). According to Figure 5.42(c), considerable slip does not happen in the wheels. Therefore, the slip detection block enables the Kalman filter to use all of these measured signals to estimate longitudinal velocity.

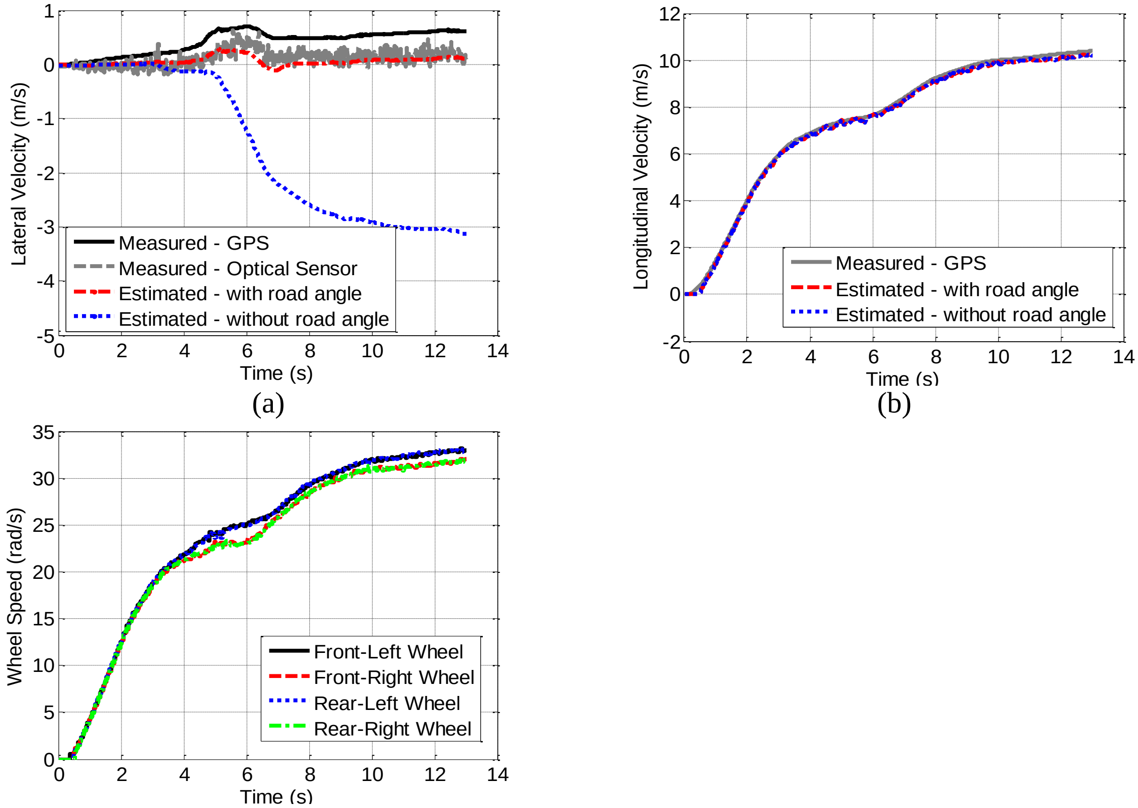

(a) (b) (c)

Figure 5.42. Performance of velocity estimation algorithm: (a) lateral velocity estimation algorithm, (b) longitudinal velocity estimation algorithm, (c) wheels' speeds

Uphill test

Figure 5.43 shows the performance of the velocity estimation algorithm on the uphill course shown in Figure 5.40(e). Same as in the previous section, the measured velocity using GPS has a drift in the first part of the test. The estimated lateral velocity with and without road grade are comparable because the road does not have significant bank angle. The estimated lateral velocity is following the measured signal obtained from the optical sensor. The estimated longitudinal velocities with and without the identified road grade have comparable performance (shown in Figure 5.43 (b)). This happens because there is not an excessive slippage in the measured wheel angular velocity of all wheels (see Figure 5.43 (c)).

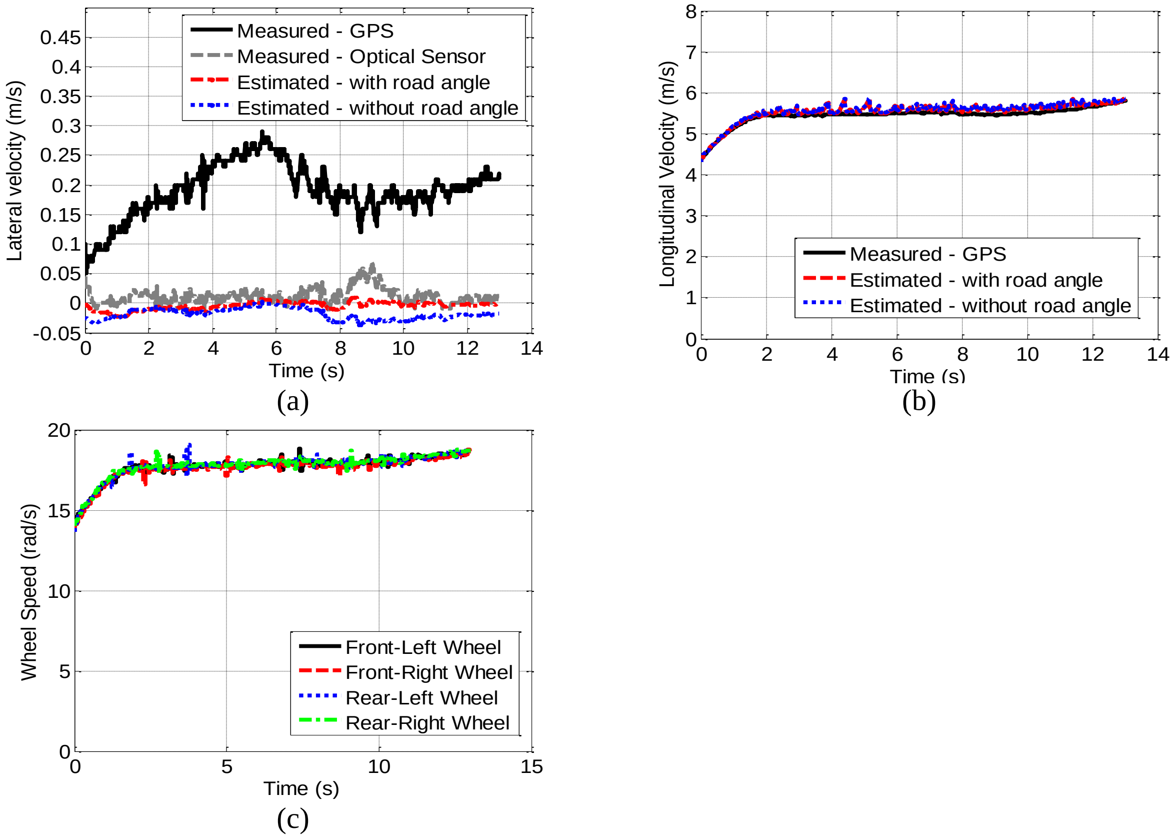

(a) (b)

(c)

Figure 5.43. Performance of velocity estimation algorithm: (a) lateral velocity estimation algorithm, (b) longitudinal velocity estimation algorithm, (c) wheels' speeds

5.5 Summary

In this chapter, the performance of the developed estimation and identification algorithms in Chapters 3 and 4 was investigated. Four different instrumented vehicles were used to examine the performance of the proposed algorithms for the selected maneuvers that excite various vehicle dynamics.

Roll and pitch angle estimation algorithms were tested with two scenarios. In the first scenario, the vehicle was excited in longitudinal direction during acceleration and brake maneuvers. In the second scenario, the vehicle was excited in the lateral direction during a DLC maneuver.

Tire force estimation and vehicle mass identification algorithms were tested in three scenarios, one DLC on dry road and two slalom maneuvers on dry and slippery roads. During these maneuvers, tire force estimation algorithms were examined in both longitudinal and lateral dynamic excitations.

The proposed vehicle velocity estimation algorithm in Chapter 3 was tested during three scenarios. Two slalom maneuvers on the dry and slippery roads and one launch maneuver on an icy road. The vehicle was excited in both longitudinal and lateral directions during two first maneuvers, and was excited in the longitudinal direction in the last maneuver.

In the last part of this chapter, road bank and grade angle identification algorithms were tested. In the first scenario the vehicle was driven on a banked road, and in the second scenario the vehicle was driven uphill. In addition, the effect of the road angles on the velocity estimation algorithm was investigated.

The accuracy of the estimated forces, vehicle body angles, vehicle velocity, identified vehicle mass and road angles were analysed, and NRMS error between measured and estimated or identified signals were calculated for the abovementioned scenarios. The test results showed the accuracy of the proposed estimation and identification algorithms during excitation of vehicle in various directions.

Chapter 6

Conclusions and future work

6.1 Conclusions and Summary

In this thesis, a unified estimation/identification structure was developed to estimate vehicle states and tire forces, and to identify vehicle mass and road bank and grade angles. The accuracy of the developed structure was verified through experiments in different test scenarios. Conventional and electrified vehicles with different type of powertrain settings (rear-wheel drive and four-wheel drive) were used to conduct the verification tests.

The developed structure is modular. Each of the proposed estimation algorithms can be substituted with a different estimation algorithm that might use a different set of sensory data. Because of the modularity of the developed structure, it can be used in a vehicle with different power sources or different powertrain systems. The estimation and identification algorithms developed in this thesis are briefly reviewed here.

- Roll and pitch estimation algorithm: roll angle of the vehicle body is estimated by this algorithm using measured roll rate and lateral acceleration. Measured pitch rate and longitudinal acceleration are used in the vehicle pitch estimation algorithm to estimate the pitch angle of the vehicle body. The observer estimated the roll angle according to the behavior of a vehicle in steady state and transient conditions in the lateral direction. Therefore, the proposed roll angle estimation algorithm considered both low excitation and large excitation of vehicle in the lateral direction.

  The proposed pitch angle estimation algorithm had a similar structure as above. It considered the longitudinal excitation instead of the lateral excitation. The experimental results in harsh maneuvers, including acceleration-brake and DLC maneuvers, show that the proposed roll and pitch angle estimation algorithms are accurate during both low and high excitations.

- Tire force estimation algorithm: tire forces in longitudinal, lateral and vertical directions for each individual wheel are estimated by this algorithm. The developed estimation algorithm did not require any tire model. Therefore, it was not sensitive to tire parameters. It was assumed that the wheel torques were available in this structure. The resultant torque acting on each wheel and wheel angular velocity of each wheel were used to estimate longitudinal forces.

  Vertical forces are estimated according to longitudinal and lateral load transfers. Measured longitudinal, lateral and vertical acceleration signals were used to estimate these forces. Estimated pitch and roll angles were used to calculate more accurate load transfers during longitudinal and lateral excitations.

  Estimated longitudinal and vertical forces were used to estimate lateral forces acting on each wheel. Measured yaw rate, lateral and longitudinal acceleration are required signals for the measurement model of the unscented Kalman filter used to estimate these forces. Vertical force distribution was used in the proposed estimation algorithm to calculate the lateral force acting on each wheel.

  Experiments (three maneuvers; two slalom maneuvers and one DLC) on dry and slippery roads verified the proposed estimation structure. In all maneuvers, the maximum NRMS error at any wheel was 7.00% for the vertical tire forces, and 7.07% for the longitudinal tire forces. Maximum NRMS errors at any wheel were 18.29% for the lateral tire forces.

- Vehicle velocity estimation algorithm: a parallel estimation algorithm was proposed to estimate longitudinal and lateral velocity concurrently. An adaptive Kalman filter was used to estimate the longitudinal velocity of the vehicle. A slip detection block was used to determine the wheels encountering no slip. Then, the measured speed of these wheels was utilized as the measured signals in Kalman filter model to estimate the longitudinal speed of the vehicle. In this algorithm, the measured longitudinal acceleration, yaw rate, estimated lateral velocity from previous step, estimated pitch angle and road grade were used for the longitudinal model in the Kalman filter. This algorithm was not sensitive to changes in tire parameters because it did not require a tire model.

Vehicle lateral velocity was estimated according to the behavior of the vehicle in the lateral direction. When the vehicle was not highly excited in the lateral direction, the inverse tire model was used to estimate the lateral velocity. When the vehicle was highly excited in the lateral direction, the proposed algorithm used the lateral vehicle kinematic model to estimate the lateral velocity of the vehicle. Measured vehicle lateral acceleration, yaw rate, wheels' speeds, and estimated vehicle longitudinal velocity from previous step, estimated roll angle and identified bank angle were the signals used in this estimation algorithm. Sensitivity analysis conducted in Chapter 4 revealed that the estimation algorithm was not sensitive to changes in the tire model parameters.

The proposed algorithm was tested on dry, slippery and icy roads in slalom and launch maneuvers. The results verify the effectiveness of the proposed estimation algorithm during maneuvers with longitudinal and lateral excitations.

- Vehicle mass identification algorithm: according to the sensitivity analysis in Section 4.2.1, the vehicle mass was the most important parameter with a significant effect on the accuracy of the vertical forces, roll and pitch angle estimation algorithms. Therefore, an identification algorithm was specifically developed to identify vehicle mass based on longitudinal and lateral dynamics of the vehicle. A RLS approach was used to identify the unknown mass during each journey. Torque acting on each wheel, wheels speeds, longitudinal acceleration, lateral acceleration, yaw rate and estimated longitudinal velocity were the signals used in the identification algorithm. The test results demonstrated the accuracy of the developed identification algorithm. The maximum error of the identified vehicle mass algorithm was 2.91% in three maneuvers (slalom and DLC on the dry road, and slalom on the slippery road).

- Road bank and road grade angles identification: these two unknown parameters are the inputs of the velocity estimation algorithm and hence need to be identified. According to the relationship between the vehicle coordinate systems in Figure 4.1, the road angles rates were calculated. Then, an observer that utilizes the vehicle dynamics behavior was developed to identify road bank and grade angles concurrently. The accuracy of this algorithm was verified in experiments on the banked road and uphill road. In addition, the effect of these angles on the estimated vehicle velocity in longitudinal and lateral directions was investigated. The results demonstrate that the bank angle has significant effect on the estimated lateral velocity. The road grade does not have a significant effect on the estimated longitudinal velocity because of the use of wheel speed data in the estimation algorithm. Road grade has a significant effect on the accuracy of the estimated longitudinal velocity when all wheels are slipping at the same time.

6.2 Future work

To improve the accuracy and reliability of the algorithms developed in this thesis, the following directions for future research are suggested:

- The torque acting on each wheel is used in the tire force estimation algorithm and vehicle mass identification algorithm. Ability to estimate or calculate the traction and brake torques will extend the use of the developed structure on conventional vehicles.

- The effect of rolling resistance and drag force can be added to the longitudinal vehicle dynamic used in the longitudinal force estimation algorithm. An investigation of the effect of rolling resistance and drag on the accuracy of the estimated forces can be useful.
- The proposed structure can be utilized to design an adaptive tire model. Connecting the proposed algorithms in this thesis with a tire model can help identify tire parameters and road friction coefficient.
- Output of some estimation or identification algorithms are used as inputs in other estimation or identification algorithms. Hence, it will be beneficial to provide maximum and minimum bounds for the states and parameters in different conditions. By defining adaptive boundaries for the outputs of each algorithm, impact potential of failures in one estimated state or in an identified parameter on deteriorating the performance of whole structure can be reduced.
- Considering the effect of camber angle on the lateral force estimation can improve the accuracy of the estimated forces at both low and high excitation scenarios.
- Suspension dynamics can be considered in the tire normal force estimation algorithm to enhance the accuracy of vertical force estimation.

Bibliography

[1] M. Rozyn and N. Zhang, "A method for estimation of vehicle inertial parameters," *Veh. Syst. Dyn. Int. J. Veh. Mech. Mobil.*, vol. 48, no. 5, pp. 547–565, May 2010.

[2] H. Ohnishi, J. Ishii, M. Kayano, and H. Katayama, "A study on road slope estimation for automatic transmission control," *JSAE Rev.*, vol. 21, no. 2, pp. 235–240, 2000.

[3] S. Solmaz, M. Akar, and R. Shorten, "Online Center of Gravity Estimation in Automotive Vehicles using Multiple Models and Switching," in *Control, Automation, Robotics and Vision, 2006. ICARCV'06. 9th International Conference on*, 2006, pp. 1–7.

[4] R. Limpert, *Brake Design and Safety, Third Edition*. SAE International, 2011.

[5] J. Kim, H. Lee, and S. Choi, "A robust road bank angle estimation based on a proportional–integral H∞ filter," *Proc. Inst. Mech. Eng. Part D J. Automob. Eng.*, 2012.

[6] R. Ghandour, A. Victorino, M. Doumiati, and A. Charara, "Tire/road friction coefficient estimation applied to road safety," in *Control & Automation (MED), 2010 18th Mediterranean Conference on*, 2010, pp. 1485–1490.

[7] Hans Pacejka, "Tire and Vehicle Dynamics," *Elsevier Butterworth-Heinemann*, 2002. [Online]. Available: https://www.elsevier.com/books/tire-and-vehicle-dynamics/besselink/978-0-08-097016-5. [Accessed: 03-Sep-2014].

[8] M. Doumiati, a. Victorino, a. Charara, and D. Lechner, "Lateral load transfer and normal forces estimation for vehicle safety: experimental test," *Veh. Syst. Dyn.*, vol. 47, no. 12, pp. 1511–1533, Dec. 2009.

[9] M. Doumiati, A. Victorino, D. Lechner, G. Baffet, and A. Charara, "Observers for vehicle tyre/road forces estimation: experimental validation," *Veh. Syst. Dyn. Int. J. Veh. Mech. Mobility*, vol. 48, no. 11, pp. 1345–1378, Nov. 2010.

[10] W. Cho, J. Yoon, S. Yim, B. Koo, and K. Yi, "Estimation of Tire Forces for Application to Vehicle Stability Control," *IEEE Trans. Veh. Technol.*, vol. 59, no. 2, pp. 638–649, 2010.

[11] R. Rajamani, G. Phanomchoeng, D. Piyabongkarn, and J. Y. Lew, "Algorithms for Real-Time Estimation of Individual Wheel Tire-Road Friction Coefficients," *IEEE/ASME Trans. Mechatronics*, vol. 17, no. 6, pp. 1183–1195, Dec. 2012.

[12] B. Jaballah, N. K. M'Sidri, A. Naamane, and H. Messaoud, "Estimation of Vehicle Longitudinal Tire Force with FOSMO & SOSMO," *Int. J. Sci. Tech. Autom. Control Comput. Eng.*, vol. 5, no. 1, pp. 1516–1531, 2011.

[13] A. Rabhi, N. K. M'Sirdi, and A. Elhajjaji, "Estimation of contact forces and tire road friction," in *Control & Automation, 2007. MED'07. Mediterranean Conference on*, 2007, pp. 1–6.

[14] K. Huh, C. Seo, J. Kim, and D. Hong, "Active Steering Control Based on The Estimated Tire Forces," in *Proceedings of the American Control Conference*, 1999, no. June.

[15] J. Ryu, S. Chen, and N. K. Moshchuk, "Estiamtion of vehicle roll rate and roll angle using suspension deflection sensors," 2007.

[16] A. Hac, T. Brown, and J. Martens, "Detection of Vehicle Rollover," in *SAE Technical Paper*, 2004, vol. 2004, no. 724.

[17] A. Rehm, "Estimation of Vehicle Roll Angle," in *Proceedings of the 4th International Symposium on Communications, Control and Signal Processing*, 2010, no. March.

[18] J. Oh and S. B. Choi, "Vehicle roll and pitch angle estimation using a cost-effective six-dimensional inertial measurement unit," *Proc. Inst. Mech. Eng. Part D J. Automob. Eng.*, vol. 227, no. 4, pp. 577–590, Oct. 2013.

[19] J. Ryu, E. J. Rossetter, and J. C. Gerdes, "Vehicle Sideslip and Roll Parameter Estimation using GPS," in *6th international sympusiom on advanced vehicle Control, Hiroshima, Japan*, 2002.

[20] L. Imsland, T. A. Johansen, T. I. Fossen, J. C. Kalkkuhl, and A. Suissa, "Nonlinear observer for vehicle velocity estimation," in *SAE Technical Paper*, 2006.

[21] L. Imsland, H. Grip, T. Johansen, T. I. Fossen, J. Kalkkuhl, and A. Suissa, "Nonlinear Observer for Vehicle Velocity with Friction and Road Bank Angle Adaptation- Validation and Comparison with an Extended Kalman Filter," in *SAE Technical Paper*, 2007.

[22] H. F. Grip, L. Imsland, T. A. Johansen, J. C. Kalkkuhl, and A. Suissa, "Vehicle Sideslip Estimation Design , implementation , and experimental validation," *IEEE Control Syst. Mag.*, vol. 29, no. 5, pp. 36–52, 2009.

[23] L.-H. Zhao, Z.-Y. Liu, and H. Chen, "Design of a Nonlinear Observer for Vehicle Velocity Estimation and Experiments," *IEEE Trans. Control Syst. Technol.*, vol. 19, no. 3, pp. 664–672, May 2011.

[24] L. K. and Q. H. L. Li, J. Song, "Vehicle velocity estimation for real-time dynamic stability control," *Int. J. Automot. Technol.*, vol. 10, no. 6, pp. 675–685, 2009.

[25] C. Troy, M. I. Us, W. C. Lin, and T. Mi, "Vehicle stability enhancement control," 2004.

[26] J. Ryu, N. K. Moshchuk, and S.-K. Chen, "Vehicle State Estimation for Roll Control System," *2007 Am. Control Conf.*, no. 1, pp. 1618–1623, Jul. 2007.

[27] J. Villagra, B. Andréa-novel, M. Fliess, and H. Mounier, “Estimation of longitudinal and lateral vehicle velocities : an algebraic approach,” in *2008 American Control Conference*, 2008, pp. 3941–3946.

[28] J. Farrelly and P. Wellstead, “Estimation of vehicle lateral velocity,” in *Proceeding of the 1996 IEEE International Conference on Control Applications*, 1996, pp. 552–557.

[29] H. Guo, Z. Wu, B. Xin, and H. Chen, “Vehicle velocities estimation based on mixed EKF,” *2011 Chinese Control Decis. Conf.*, pp. 2030–2035, May 2011.

[30] H. Guo, H. Chen, F. Xu, F. Wang, and G. Lu, “Implementation of EKF for Vehicle Velocities Estimation on FPGA,” *IEEE Trans. Ind. Electron.*, vol. 60, no. 9, pp. 3825–3835, 2013.

[31] L. R. Ray, “Nonlinear State and Tire Force Estimation for Advanced Vehicle Control,” *IEEE Trans. Control Syst. Technol.*, vol. 3, pp. 1–8, 1999.

[32] L. Chu, Y. Shi, Y. Zhang, H. Liu, and M. Xu, “Vehicle lateral and longitudinal velocity estimation based on Adaptive Kalman Filter,” in *2010 3rd International Conference on Advanced Computer Theory and Engineering(ICACTE)*, 2010, pp. 325–329.

[33] M. Oudghiri, M. Chadli, and A. El Hajjaji, “Lateral Vehicle Velocity Estimation Using Fuzzy Sliding Mode Observer,” in *Proceedings of the 15th Mediterranean Conference on Control & Automation*, 2007, no. 1.

[34] M. Tanelli, S. Savaresi, and C. Cantoni, “Longitudinal Vehicle Speed Estimation for Traction and Braking Control Systems,” *2006 IEEE Int. Conf. Control Appl.*, pp. 2790–2795, Oct. 2006.

[35] C. K. Song and J. K. Hedrick, “Vehicle Speed Estimation Using Accelerometer and Wheel Speed Measurements,” in *SAE Technical Paper*, 2002, no. 724.

[36] F. Jiang and Z. Gao, “An Adaptive Nonlinear Filter Approach to the Vehicle Velocity Estimation for ABS,” in *Proceedings of the 2000 IEEE International Conference Applications*, 2000, vol. 1, pp. 490–495.

[37] M. Basset, C. Zimmer, and G. L. Gissinger, “Fuzzy Approach to the Real Time Longitudinal Velocity Estimation of a FWD Car in Critical Situations Fuzzy Approach to the Real Time Longitudinal Velocity Estimation of a FWD Car in Critical Situations,” *Veh. Syst. Dyn. Int. J. Veh. Mech. Mobil.*, vol. 27, pp. 477–489, 1997.

[38] Y. Gao, Y. Feng, and L. Xiong, “Vehicle Longitudinal Velocity Estimation with Adaptive Kalman Filter,” in *Proceedings of the FISITA 2012 World Automotive Congress*, 2013, vol. 198, pp. 415–423.

[39] M. Klomp, Y. Gao, and F. Bruzelius, “Longitudinal velocity and road slope estimation in hybrid electric vehicles employing early detection of excessive wheel slip,” *Veh. Syst. Dyn. Int. J. Veh. Mech. Mobil.*, vol. 52, no. sup1, pp. 172–188, Mar. 2014.

[40] H. H. Kim and J. Ryu, “Sideslip angle estimation considering short-duration longitudinal velocity variation,” *Int. J. Automot. Technol.*, vol. 12, no. 4, pp. 545–553, 2011.

[41] A. Hac, D. Nichols, and D. Sygnarowicz, “Estimation of Vehicle Roll Angle and Side Slip for Crash Sensing,” *SAE Tech. Pap.*, pp. 1–529, 2010.

[42] X. Gao, Z. Yu, and T. Xu, “Longitudinal Velocity Estimation of Electric Vehicle with 4 In-wheel Motors,” in *SAE Technical Paper*, 2008, vol. 2008, no. 724.

[43] C. K. Song and J. K. Hedrick, “Vehicle Speed Estimation Using Accelerometer and Wheel Speed Measurements,” in *SAE Technical Paper*, 2012, no. 724.

[44] G. Heydinger, R. Bixel, and N. Durisek, “Effects of loading on vehicle handling,” *SAE Tech. Pap.*, 1998.

[45] T. Sun, Y. Zhang, and P. Barak, “4-DOF Vehicle Ride Model,” *SAE Tech. Pap.*, 2002.

[46] H. K. Fathy, D. Kang, and J. L. Stein, “Online Vehicle Mass Estimation Using Recursive Least Squares and Supervisory Data Extraction,” in *2008 American Control Conference*, pp. 1842–1848.

[47] S. T. M.C. Best, A.P. Newton, “The identifying extended Kalman filter : parametric system identification of a vehicle handling model,” *Proc. Inst. Mech. Eng. Part K J. Multi -body Dyn.*, vol. 221, no. 1, pp. 87–98, 2007.

[48] H. S. Bae, J. Ryu, and J. C. Gerdes, “Road grade and vehicle parameter estimation for longitudinal control using GPS,” in *IEEE Conference on Intelligent Transportation Systems, Proceedings, ITSC*, 2001, pp. 166–171.

[49] A. Vahidi, A. Stefanopoulou, and H. Peng, “Experiments for online estimation of heavy vehicle’s mass and time-varying road grade,” in *Proceedings of the ASME International Mechanical Engineering Congress and Exposition*, 2003.

[50] V. Winstead and I. V Kolmanovsky, “Estimation of road grade and vehicle mass via model predictive control,” in *Control Applications, 2005. CCA 2005. Proceedings of 2005 IEEE Conference on*, 2005, pp. 1588–1593.

[51] R. R. J. K. Hedrick, “Adaptive Observers for Active Automotive Suspensions: Theory and Experiment,” *Control Syst. Technol. IEEE Trans.*, vol. 3, no. I, pp. 86–93, 1995.

[52] H. Lee, K. Park, T. Hwang, K. Noh, S. J. Heo, J. I. Jeong, S. Choi, B. Kwak, and S. Kim, “Development of enhanced ESP system through vehicle parameter estimation,” *J. Mech. Sci. Technol.*, vol. 23, no. 4, pp. 1046–1049, 2009.

[53] K.-J. Han, I.-K. Kim, H. Y. Jo, and K.-S. Huh, “Development and experimental evaluation of an online estimation system for vehicle mass,” *Proc. Inst. Mech. Eng. Part D J. Automob. Eng.*, vol. 223, no. 2, pp. 167–177, Feb. 2009.

[54] S. A. M. Bolhasani, “Parameter Estimation of Vehicle Handling Model Using Genetic Algorithm,” in *SAE Technical Paper*, 2002, no. 724.

[55] N. Kidambi, R. L. Harne, Y. Fujii, G. M. Pietron, and K. W. Wang, “Methods in Vehicle Mass and Road Grade Estimation,” *SAE Int. J. Passeng. Cars*, vol. 7, no. 3, pp. 981–991, Apr. 2014.

[56] D. Piyabongkarn, R. Rajamani, J. A. Grogg, and J. Y. Lew, “Development and experimental evaluation of a slip angle estimator for vehicle stability control,” *Control Syst. Technol. IEEE Trans.*, vol. 17, no. 1, pp. 78–88, 2009.

[57] S.-H. You, J.-O. Hahn, and H. Lee, “New adaptive approaches to real-time estimation of vehicle sideslip angle,” *Control Eng. Pract.*, vol. 17, no. 12, pp. 1367–1379, Dec. 2009.

[58] B. F. Suissa A, Zomotor Z, “Method For Determining Variables Characterizing Vehicle Handling,” 1996.

[59] L. Imsland, T. a. Johansen, H. F. Grip, and T. I. Fossen, “On non-linear unknown input observers–applied to lateral vehicle velocity estimation on banked roads,” *Int. J. Control*, vol. 80, no. 11, pp. 1741–1750, Nov. 2007.

[60] J. C. Jihan Ryu, Erdes, “Estimation of Vehicle Roll and Road Bank Angle,” in *2004 American Control Conference*, 2004.

[61] H. E. Tseng, “Dynamic Estimation of Road Bank Angle,” *Veh. Syst. Dyn. Int. J. Veh. Mech. Mobil.*, vol. 36, no. 4–5, pp. 307–328, 2001.

[62] S. Mammar, S. Glaser, and M. Netto, “Vehicle lateral dynamics estimation using unknown input proportional-integral observers,” in *American Control Conference, 2006*, 2006, p. 6 pp.

[63] K. Kawashima, Y. Hori, T. Uchida, and S. Oh, “Robust bank angle estimation for rolling stability control on electric vehicle,” in *Advanced Motion Control, 2010 11th IEEE International Workshop on*, 2010, pp. 448–453.

[64] Y. Sebsadji, S. Glaser, S. Mammar, and M. Netto, “Vehicle roll and road bank angles estimation,” in *Proc. 17th IFAC World Congress*, 2008, pp. 7091–7097.

[65] D. Söffker, T.-J. Yu, and P. C. Müller, “State estimation of dynamical systems with nonlinearities by using proportional-integral observer,” *Int. J. Syst. Sci.*, vol. 26, no. 9, pp. 1571–1582, Sep. 1995.

[66] P. Sahlholm and K. Henrik Johansson, “Road grade estimation for look-ahead vehicle control using multiple measurement runs,” *Control Eng. Pract.*, vol. 18, no. 11, pp. 1328–1341, Nov. 2010.

[67] J. Parviainen, J. Hautamäki, J. Collin, and J. Takala, “Barometer-Aided Road Grade Estimation,” in *Proceedings of 13th IAIN World Congress, Stockholm, Sweden, 27-30 October, 2009*, 2009.

[68] J. Parviainen, J. Kantola, and J. Collin, “Differential barometry in personal navigation,” in *Position, Location and Navigation Symposium, 2008 IEEE/ION*, 2008, pp. 148–152.

[69] T. M. J. Barrho, M. Hiemer, U. Kiencke, “Estimation of elevation difference based on vehicle’s inertial sensors,” in *International Federation of Automatic Control*, 2005.

[70] H. F. Grip, L. Imsland, T. A. Johansen, J. C. Kalkkuhl, and A. Suissa, “Estimation of road inclination and bank angle in automotive vehicles,” in *American Control Conference, 2009. ACC’09.*, 2009, pp. 426–432.

[71] L.-Y. Hsu and T.-L. Chen, “Estimating Road Angles With the Knowledge of the Vehicle Yaw Angle,” *J. Dyn. Syst. Meas. Control*, vol. 132, no. 3, p. 031004, 2010.

[72] T. J. G. M.C. Best, “Combined state and parameter estimation of vehicle handling dynamics,” in *Proceeding of AVEC 2000 5th International Symposium on Advanced Vehicle Control*, 2000, no. August.

[73] C. Nuthong, “Estimation of Tire-Road Friction Forces using Kalman Filtering for Advanced Vehicle Control,” Institut für Steuer- und Regelungstechnik, Universität der Bundeswehr München, 2009.

[74] T. A. Wenzel, K. J. Burnham, M. V Blundell, and R. A. Williams, “Dual extended Kalman filter for vehicle state and parameter estimation,” *Veh. Syst. Dyn. Int. J. Veh. Mech. Mobil.*, vol. 44, no. 2, pp. 153–171, 2006.

[75] S. Hong, C. Lee, F. Borrelli, and J. K. Hedrick, “A Novel Approach for Vehicle Inertial Parameter Identification Using a Dual Kalman Filter,” *IEEE Trans. Intell. Transp. Syst.*, 2014.

[76] A. Rezaeian, R. Zarringhalam, M. S. Fallah, W. Melek, and A. Khajepour, “Joint Unscented Kalman Filter for Combined Estimation of Vehicle States and Parameters,” in *AVEC’12*, 2012.

[77] J. Kim and H. Lee, “Sensor fault detection and isolation algorithm for a continuous damping control system,” *Proc. Inst. Mech. Eng. Part D J. Automob. Eng.*, vol. 225, no. 10, pp. 1347–1364, Jul. 2011.

[78] M. L. Shannon, B. Youngberg, A. Millie, P. Schweizer, and J. C. Gerdes, “Calculating longitudinal wheel slip and tire parameters using GPS velocity,” in *Proceedings of the American Control Conference*, 2001, pp. 1800–1805.

[79] M. a. Wilkin, W. J. Manning, D. a. Crolla, and M. C. Levesley, “Use of an extended Kalman filter as a robust tyre force estimator,” *Veh. Syst. Dyn. Int. J. Veh. Mech. Mobil.*, vol. 44, no. sup1, pp. 50–59, Jan. 2006.

[80] D. Simon, “Optimal State Estimation: Kalman, H Infinity, and Nonlinear Approaches,” *WILY*, 2006. [Online]. Available: http://ca.wiley.com/WileyCDA/WileyTitle/productCd-0471708585.html. [Accessed: 10-Sep-2014].

[81] S. Antonov, A. Fehn, and A. Kugi, “Unscented Kalman filter for vehicle state estimation,” *Veh. Syst. Dyn. Int. J. Veh. Mech. Mobility*, vol. 49, no. 9, pp. 1497–1520, Sep. 2011.

[82] S. Julier, J. Uhlmann, and H. F. Durrant-whyte, “A New Method for the Nonlinear Transformation of Means and Covariances in Filters and Estimators,” *IEEE Trans. Automat. Contr.*, vol. 45, no. 3, pp. 477–482, 2000.

[83] M. Doumiati, A. C. Victorino, A. Charara, and D. Lechner, “Onboard Real-Time Estimation of Vehicle Lateral Tire – Road Forces and Sideslip Angle,” *IEEE/ASME Trans. Mechatronics*, vol. 16, no. 4, pp. 601–614, 2011.

[84] E. A. Wan and R. Van Der Merwe, “The Unscented Kalman Filter for Nonlinear Estimation,” in *Proceeding of IEEE Symposium (AS-SPCC)*, 2000.

[85] C. Canudas-de-wit, P. Tsiotras, and E. Velenis, “Dynamic Friction Models for Road / Tire Longitudinal Interaction,” *Veh. Syst. Dyn. Int. J. Veh. Mech. Mobil.*, vol. 39, no. 3, pp. 189–226, 2002.

[86] C. C. DE Wit and P. Tsiotras, “Dynamic Tire Friction Models for Vehicle Traction Control,” in *Proceedings of the 38th Conference on Decision & Control*, 1999, no. December, pp. 3746–3751.

[87] J. J. C. G. Ryu, “Estimation of Vehicle Roll and Road Bank Angle.” [Online]. Available: http://www-cdr.stanford.edu/dynamic/estimationGPS/acc2004ryu.pdf.

[88] R. Rajamani, *Vehicle dynamics and control*. Springer, 2012.

[89] W. J. Bagaria, “Vehicle Center of Gravity Height Measurement Errors,” in *SAE Technical Paper*, 2014, no. 724.

[90] N. Mango, “Measurement & Calculation of Vehicle Center of Gravity Using Portable Wheel Scales,” in *SAE Technical Paper*, 2014.

Appendix I

Unscented Kalman filter estimation algorithm

An unscented Kalman filter (UKF) is applied to estimate lateral tire forces. The UKF is an approximation method that uses a minimal set of carefully chosen weighted sample points, referred to as sigma points[81].

The state-space equations are:

$$X_k = f(x_{k-1}, w_{k-1}) + v_k \tag{AI-1}$$

$$y_k = h(x_{k-1}, w_{k-1}) + n_k \tag{AI-2}$$

The UKF algorithm can be expressed as follows for the nonlinear system above:

Initialization

$$\bar{X}_0 = E[X_0], \tag{AI-3}$$

$$P_0 = E[(X_0 - \bar{X}_0)(X_0 - \bar{X}_0)^T], \tag{AI-4}$$

where $\bar{X}_0$ and P_0 are the initial state and covariance, respectively.

Sigma points calculation and prediction

This algorithm uses $2n + 1$ sigma points that are generated as

$$\chi_{0,k|k-1} = \bar{X}_{k-1} \tag{AI-5}$$

$$\chi_{i,k|k-1} = \bar{X}_{k-1} \pm \sqrt{(n+\lambda)P_{k-1}}\,, \quad i = 1,2,\dots,2n \tag{AI-6}$$

where n is the number of states, $\bar{X}_{k-1}$ and P_{k-1} are the estimated state and covariance, respectively, and

$$\lambda = n\,(\alpha^2 - 1) + \alpha^2\,\epsilon \tag{AI-7}$$

where α and ϵ are responsible for the distribution of sigma points around the mean value of the states. α should be a small number $(10^{-4} \leq \alpha \leq 1)$ [84], and ϵ is set to a small number.

These sigma points are propagated by:

$$\chi^{\star}_{i,k|k-1} = f\left(\chi_{i,k-1}, U_k\right), \quad i = 0,1,2,\dots,2n \tag{AI-8}$$

and the states and covariance are predicted by:

$$\bar{X}_{k|k-1} = \sum_{i=0}^{2n} \omega_i^m \chi^{\star}_{i,k|k-1} \tag{AI-9}$$

$$P_{k|k-1} = \sum_{i=0}^{2n} \omega_i^c (\chi^{\star}_{i,k|k-1} - \bar{X}_{k|k-1}) \times \left(\chi^{\star}_{i,k|k-1} - \bar{X}_{k|k-1}\right)^T + Q \tag{AI-10}$$

where

$$\omega_0^m = \frac{\lambda}{\lambda + n} \tag{AI-11}$$

$$\omega_0^c = \frac{\lambda}{\lambda + n} + (n - \alpha^2 + \beta), \tag{AI-12}$$

$$\omega_i^m = \omega_i^c = \frac{1}{2(\lambda + n)}, \quad i = 1,2,\dots,\ 2n, \tag{AI-13}$$

ω_i^m is the weight for the mean and ω_i^c is the weight for the covariance of sigma points. β is a constant used to incorporate a part of the prior knowledge about the distribution of X. For Gaussian distributions, $\beta = 2$ is optimal [84]. Q is a pre-specified process noise covariance matrix.

Based on the information above, the sigma points and outputs can be updated by:

$$\chi_{k|k-1} = \left[\bar{X}_{k|k-1}, \bar{X}_{k|k-1} \pm \sqrt{(n + \lambda)P_{k-1}}\right], \tag{AI-14}$$

$$\gamma_{i,k|k-1} = h(\chi_{i,k|k-1}) \tag{AI-15}$$

$$\bar{Y}_{k|k-1} = \sum_{i=0}^{2n} \omega_i^m \, \gamma_{i,k|k-1}. \tag{AI-16}$$

Measurement update

$$P_{\bar{Y}_k\bar{Y}_k} = \sum_{i=0}^{2n} \omega_i^c \left(\gamma_{i,k|k-1} - \bar{Y}_{k|K-1}\right) \times \left(\gamma_{i,k|k-1} - \bar{Y}_{k|K-1}\right)^T + R \tag{AI-17}$$

$$P_{\bar{X}_k\bar{Y}_k} = \sum_{i=0}^{2n} \omega_i^c \left(\chi_{i,k|k-1} - \bar{X}_{k|K-1}\right) \times \left(\gamma_{i,k|k-1} - \bar{Y}_{k|K-1}\right)^T \tag{AI-18}$$

$$K_k = P_{\bar{X}_k\bar{Y}_k} P_{\bar{Y}_k\bar{Y}_k}^{-1} \tag{AI-19}$$

where R is the measurement noise covariance matrix, assumed to have normal distribution with zero mean values.

$P_{\bar{Y}_k\bar{Y}_k}$ is the innovation covariance, and $P_{\bar{X}_k\bar{Y}_k}$ is the cross correlation matrix. The filter gain, K_k, is computed based on these covariance matrices. Finally, the covariance and states can be updated by:

$$P_k = P_{k|k-1} - K_k P_{\bar{Y}_k\bar{Y}_k} K_k^T, \tag{AI-20}$$

$$\bar{X}_k = \bar{X}_{k|K-1} + K_k\left(Y_k - \bar{Y}_{k|k-1}\right). \tag{AI-21}$$

Appendix II

Kalman filter estimation algorithm

The states of a linear systems can be estimated by using a Kalman filter [80]. Here, the discrete Kalman filter equations will be presented.

The state-space equations are

$$x_k = A\, x_{k-1} + B\, u_{k-1} + v_k \tag{AII-1}$$

$$y_k = C\, x_{k-1} + n_k \tag{AII-2}$$

The algorithm is initialized as follows:

$$\bar{X}_0 = E[X_0], \tag{AII-3}$$

$$P_0 = E[(X_0 - \bar{X}_0)(X_0 - \bar{X}_0)^T], \tag{AII-4}$$

where $\bar{X}_0$ and P_0 are the initial state and covariance, respectively.

<u>Prediction step:</u>

In the next step, the covariance error matrix and states will be updated for each time step $k = 1,2, ...$

$$P_{k|k-1} = AP_{k-1}A^T + Q, \tag{AII-5}$$

$$\hat{x}_{k|k-1} = A\, \hat{x}_{k-1} + B\, u_{k-1}\, , \tag{AII-6}$$

where Q is the processing covariance matrix error, $P_{k|k-1}$ is the updated covariance error matrix, and $\hat{x}_{k|k-1}$ is the predicted states.

<u>Correction step:</u>

Kalman gain will be calculated for each time step. Moreover, the covariance error matrix will be calculated. Finally, the states will be estimated.

$$K_k = P_{k|k-1}\, C^T \left(C\, P_{k|k-1}\, C^T + R\right)^{-1}, \tag{AII-7}$$

$$P_k = (I_{n\times n} - K_k\, C)P_{k|k-1} \tag{AII-8}$$

$$\hat{x}_k = \hat{x}_{k|k-1} + K_k(y_k - C\,\hat{x}_{k|k-1}) \tag{AII-9}$$

where R is the measurement covariance matrix error, K_k is the Kalman gain, P_k is the corrected covariance matrix, and $\hat{x}_k$ is the estimated states.